SYNTHESIS AND APPLICATION OF TARGETED MOLECULAR IMAGING

AGENTS FOR ENHANCED DISEASE IMAGING AND THERAPY

By

MINGFENG BAI

Dissertation

Submitted to the Faculty of the

Graduate School of Vanderbilt University

in partial fulfillment of the requirements

for the degree of

DOCTOR OF PHILOSOPHY

in

Chemistry

December, 2007

Nashville, Tennessee

Approved by:

Darryl J. Bornhop

David E. Cliffel

Brian O. Bachmann

J. Oliver McIntyre

Eva M. Harth

To my supportive parents, who have guided me

To my beloved wife, Yao, who has stood by me

and

To my lovely boy, Leo, who has been the joy of my life

ACKNOWLEDGEMENTS

TABLE OF CONTENTS

LIST OF TABLES

LIST OF FIGURES

LIST OF SCHEMES

LIST OF ABBREVIATIONS

2-AG   2-arachidonoyl glycerol

ATP   adenosine triphosphate

BBB   blood brain barrier

PBS   phosphate buffered saline

CBZ   benzyl carbonate

CLIO   cross-linked iron oxide

CMF-PBS   calcium- and magnesium-free phosphate buffered saline

CT   computer tomography

Cy5.5-2DG   cy5.5-D-glucosamine

DMAP   4-(dimethylamino)pyridine

DMEM   dulbecco's modified eagle medium

DMSO   dimethylsulfoxide

DO3A   1,4,7-tris(carboxymethyl)-10-(2'-hydroxypropyl)-1,4,7,10-
                tetraazacycl ododecane

DOTA   tetraazacyclododecanetetraacetic acid

DTPA   diethylenetriaminepentaacetic acid

EDTA   ethylenediaminetetraacetic acid

eEPC   embryonic epithelial progenitor cells

EGF   epidermal growth factor

EGFr   epidermal growth factor receptor

ESC   embryonic stem cells

FBS   fetal bovine serum

^{18}FDG	[^{18}F]fluoro-2-deoxy-D-glucose
^{18}FES	[^{18}F]fluoro-17β-oestradial
FITC	fluorescein isothiocyanate
^{18}FLT	[^{18}F]fluorothymidine
FMT	fluorescence molecular tomography
FOV	field of view
^{18}FPCV	[^{18}F]fluoropenciclovir
GLUT	glucose transporters
GPCR	G protein-coupled receptors
GRID	gadolinium rhodamine dextran
H&E	hematoxylin and eosin
HBTU	2-(1H-Benzotriazole-1-yl)-1,1,3,3-tetramethyl uronium hexafluorophosphate
HPLC	high performance liquid chromatography
HSA	human serum albumin
IACUC	institutional animal care and use committee
ICG	indocyanine green
IDCC	indodicarbocyanine
ITCC	indotricarbocyanine
Ln	lanthanide
MI	molecular imaging
MION	monocrystalline iron-oxide nanoparticle
MISO	fluoromisonidazole

MMP	matrix metalloproteinases
MNC	mononuclear cells
MR	magnetic resonance
MRI	magnetic resonance imaging
MS	mass spectrometry
NAD[H]	nicotinamide adenine dinucleotide
NHS	N-hydroxysuccinimide
NIR	near infrared
NMR	nuclear magnetic resonance
PBR	peripheral benzodiazepine receptor
PET	positron emission tomography
pi	post-injection
Pyro-2DG	pyropheophorbide 2-deoxyglucosamide
QDs	quantum dots
RTK	receptor tyrosine kinase
ROI	region of interest
SAR	structure activity relationship
SPECT	single photon emission computed tomography
SPIO	superparamagnetic iron-oxide nanoparticle
T1	spin-lattice relaxation
T2	spin-spin relaxation
Tf	transferring
TBAF	Tetrabutylammonium fluoride

Δ^9-THC	(-)-trans-Δ^9-tetrahydrocanabinol
THF	tetrahydrofuran
TFA	trifluoroaceitic acid
TSPO	Translocator Protein
TSTU	*N,N,N′,N′*-tetramethyl-*O*-(*N*-succinimidyl)uronium tetrafluoroborate
uPA	urokinase plasminogen activator
US	ultrasound
USPIO	ultrasmall superparamagnetic iron-oxide nanoparticle
UV	ultraviolet
VEGF	vascular endothelial growth factor

CHAPTER I

INTRODUCTION

1.1 Molecular Imaging

Molecular imaging (MI) is the observation and quantification of a molecular

event in vivo[1]. It provides relevant biological information to characterize and measure

physiological processes at the molecular level in vivo. Disease is usually diagnosed based

on physiological changes, which are a late manifestation of molecular changes underlying

the disease. Therefore, imaging of these molecular changes would allow earlier detection

of diseases. In addition, quantification of diseased area indicates alterations of disease,

which provides opportunities in efficacy monitoring. Moreover, successful surgical

resection relies on accurate location of diseased tissue. Imaging of the diseased cells can

be potentially used to improve clinical outcome.

Due to the importance of molecular imaging, this multi-disciplinary area is now

adding a new dimension to our understanding of biological pathways, pharmacological

mechanisms and disease processes. Using exogenous targeted probes, researchers can

now perform non-invasive studies on cells and living systems as well as visualize gene

expression, biochemical reactions, signal transduction, regulatory pathways and direct

drug action in whole organisms in vivo[2].

There are four major concerns about development of molecular imaging strategies:

(1) Is there a molecular target relevant to the disease of interest? (2) After a target is

selected, is there a molecular probe with high binding affinity for the target? (3) Can this

1

probe overcome biologic delivery barriers, such as vascular, interstitial and cell membrane? (4) What is the imaging system that can provide sensitive, fast and high resolution images? To address these concerns, imaging modalities, targets and probes will be discussed in this chapter.

<center>1.2 Imaging Modalities, Targets and Agents</center>

Commonly used molecular imaging modalities include positron emission tomography (PET), single photon emission computed tomography (SPECT), magnetic resonance imaging (MRI), optical imaging, ultrasound (US) and computed tomography (CT). Each imaging modality has strengths and weakness in terms of sensitivity, spatial and temporal resolution, contrast and cost (Table 1.1)[3-5]. Exquisite sensitivity is the primary advantage of nuclear imaging modalities, especially for PET, which is even more sensitive than SPECT. The major limitation is low spatial resolution and high cost. Magnetic resonance imaging (MRI) has high spatial resolution; however, it requires high concentrations of imaging agents for detection (e.g. it has low sensitivity). Optical imaging is highly sensitive and provides high contrast images, but has limited tissue penetration. Ultrasound is very sensitive for contrast agent detection, but achieving

Table 1.1. Comparison of imaging modalities

Modality	Sensitivity	Cost	Resolution		
			Spatial	Temporal	Contrast
MRI	*	***	10-100 μm	msec	***
PET	***	***	4-5 mm	min	**
SPECT	**	**	8-12 mm	min	*
Optical	***	*	1-2 mm	msec	***
US	***	**	50 μm	msec	**
CT	*	*	50-100 μm	sec	**

***, high; **, medium; *, low.

sufficient stability of these agents remains challenging. Moreover, high spatial resolution of ultrasound decreases dramatically with depth. CT is limited by low sensitivity and adverse effects of ionizing radiation.

Selecting a biologically active target is usually the first step in molecular imaging research and leads the design of a molecular imaging agent. Potential targets include proteins, DNA, RNA, carbohydrates and lipids[6]. Several properties of these biomolecules as imaging targets need to be considered, such as location of the target molecules, related biological activities or diseases, available ligands that specifically target these biomolecules, and the number of biomolecules in each cell. To visualize these targets in living subjects and study molecular events, specifically targeted imaging agents need to be developed[7,8].

A molecular imaging agent typically consists of a signaling moiety, such as a radioisotope, metal ion or a fluorochrome, and a targeting functionality, including receptor ligand, sugar, enzyme substrate, antibody and protein. In general, imaging agents can be categorized into three groups: nonspecific, non-activatable targeted and activatable targeted agents[6,9]. Nonspecific agents do not have targeting functionalities, thus are not able to interact with a specific target. These agents differentiate tissues based on permeability or perfusion and are usually used to characterize physiological changes which occur relatively late in disease processes. Both non-activatable and activatable targeted agents allow visualization of specific biological processes at the cellular or molecular level, allowing characterization of disease in the early stages. Since the signaling moieties in non-activatable targeted agents are always active, these agents are detectable regardless of their interaction with the targeting site. As a result, background

noise is usually seen but tends to decrease to low level after the agent remains bound to the target and unbound agents are cleared. Activatable targeted agents, also called "smart agents", are not detectable until they are activated by the target (usually an enzyme)[10]. Therefore, improved signal to noise ratio is achieved[9]. Imaging agents can be categorized into five groups, based on imaging modalities, including MRI agents, radionuclide imaging agents, optical imaging agents, ultrasound imaging agents and multi-modality imaging agents. The details of these agents will be discussed in this dissertation.

1.3 Magnetic Resonance Imaging

1.3.1 Magnetic Resonance Imaging Principles

The fundamental basis of magnetic resonance imaging is governed by the same principles of nuclear magnetic resonance (NMR)[11-13]. Water and lipids, which have many hydrogen atoms, are the primary components in the human body. As hydrogen nuclei can produce NMR signal, the human body can be imaged under a powerful, uniform magnet.

In principle, unpaired nuclear spin generates a magnetic field. When a strong external magnetic field is applied, unpaired nuclear spins align either parallel (low energy) or anti-parallel (high energy) to the external magnetic field, with slightly more spins at parallel position than at anti-parallel position. After the magnetic field is perturbed by a radiofrequency pulse, these spins will relax to their original orientation, with the emission of a radio frequency signal. This emission signal corresponds to the energy difference between the two energy states and can be detected by a radio frequency coil in the MRI instrument. When spins move back to the low energy parallel position, two types of relaxation take place. Spin-lattice relaxation (T1) is related to energy exchange between

the spin system and the surrounding thermal reservoir. Spin-spin relaxation (T2) is related to energy exchange within the system itself. Roughly speaking, T1 relaxation time determines how fast an MRI signal can be repeatedly collected and the T2 relaxation time determines how quickly each measurement can be made. Both relaxations occur simultaneously with the only restriction being that T2 is less than or equal to T1[11]. T1 and T2 are dependent on sample, tissue, and magnetic field strength[12]. MRI contrast agents can modify T1 or T2 relaxation times for improved sensitivity.

Main advantages of MRI include high spatial resolution and the ability to simultaneously record information at both anatomical and molecular levels[5]. Common magnetic field strengths range from 0.3 to 3 T, although field strengths of 9.4 T or higher are used in research scanners. Standard clinical magnetic resonance imagers (1.5-Tesla magnetic field strength) provide images with about 1 mm spatial resolution. When special coils and probes are employed to imagers, resolution as low as 10 μM can be achieved[14]. The high spatial resolution makes intravascular and intracavitary MR imaging possible[14]. In addition, MRI has good temporal resolution (ms), and a typical image requisition can be obtained in seconds to minutes. For high resolution three dimensional MRI scan, the examination time is usually several hours[15].

However, MRI is limited by its low sensitivity, which is several orders of magnitude less than PET, SPECT and optical imaging[3,6]. This necessitates larger quantities (millimolar to micromolar) of contrast agents at the target site, and therefore, large amounts need to be injected. This low sensitivity of MRI is mainly due to the small percentage of hydrogen magnetic dipoles that preferentially align themselves within an applied external magnetic field[7]. MRI also has some other disadvantages, such as the

high cost and complexity of the scanners, compared to optical imaging, ultrasound and CT.

1.3.2 Magnetic Resonance Imaging Agents and Targets

Generally there are two types of MRI contrast agents: lanthanide chelates (T1 agents) and iron particles (T2 agents). Lanthanide complexes slow T1 relaxation time and increase the number of spins that can absorb energy from the radio frequency pulse[12,16,17]. As a result, T1 contrast agents increase signal to noise ratio and have positive signal enhancement on MRI images[18]. For T2 contrast agents, the most common probes are iron-oxide nanoparticles. These agents reduce T2 time and decrease the local signal intensity. Therefore, T2 agents decreases signal to noise ratio and produce a negative signal enhancement on T2-weighted MRI images[4,12]. In other words, T2 contrast increases with "darkness".

Typical T1 contrast agents are small molecules with a lanthanide chelate as contrast producing moiety. Usually the chelated metal ion is Gd^{3+}, even though Mn^{2+} and Fe^{3+} ions are suitable for T1 weighted MRI imaging as well[19,20]. Gadolinium (III) is highly paramagnetic with seven unpaired electrons and a long electronic relaxation time, making it a good relaxation agent. One example of Gd^{3+} based agent is gadolinium-
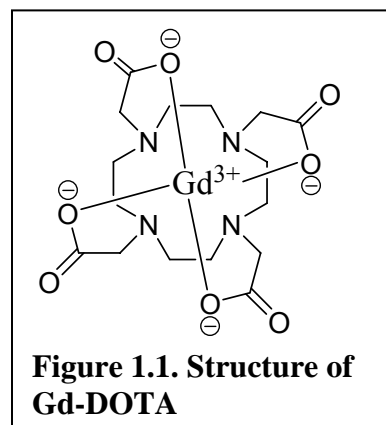
Figure 1.1. Structure of Gd-DOTA

tetraazacyclododecanetetraacetic acid (Gd-DOTA) (Figure 1.1), which is one of the earliest T1 contrast agents and has been successfully used for contrast enhanced imaging of various diseases and cancers[21-29]. Some other examples of Gd-based T1 contrast agents include gadolinium- diethylenetriaminepentaacetic acid (Gd-DTPA)[30], gadolinium-

ethylenediaminetetraacetic acid (Gd-EDTA)[31], and gadolinium 1,4,7-tris(carboxymethyl)-10-(2'-hydroxypropyl)-1,4,7,10-tetraazacycl ododecane (Gd-HP-DO3A)[32].

As it was mentioned earlier, the low sensitivity of MRI necessitates larger quantities (millimolar to micromolar) of T1 contrast agents at the target site. This disadvantage can be partially resolved by using targeted, polymeric (multiple Gd^{3+} on one molecule) and/or smart T1 weighted MRI contrast agents. Targeted contrast agents are usually synthesized by direct conjugation of a contrast agent (such as Gd-DOTA) to a targeting functionality, such as an antibody and a receptor ligand. Some examples include Gd labeled antibodies for tumor angiogenesis imaging[33], polylysine-Gd-embryonic antigen complex that target colorectal carcinoma[34], Gd labeled mesoporphyrins for necrotic tumor assessment[35] and folate receptor targeted Gd-folate-dendrimer complex for ovarian tumor imaging[36]. Polymeric Gd agents can be prepared by chelating multiple Gd ions with cyclodextrin or coupling multiple Gd based lanthanide chelates to dendrimers/polymers[37-42]. The polylysine-Gd-embryonic antigen and Gd-folate-dendrimer complexes are both based on polymer/dendrimer backbone. A smart MRI agent consists of a lanthanide chelate and a "bridge" over the metal ion. The bridge blocks the interaction between the metal ion and bulk water molecules, making it ineffective at water interaction. Upon reaction with a certain disease-specific target enzyme, the bridge can be opened,

Figure 1.2. The transition of EgadMe from a weak to a strong relaxivity state[43].
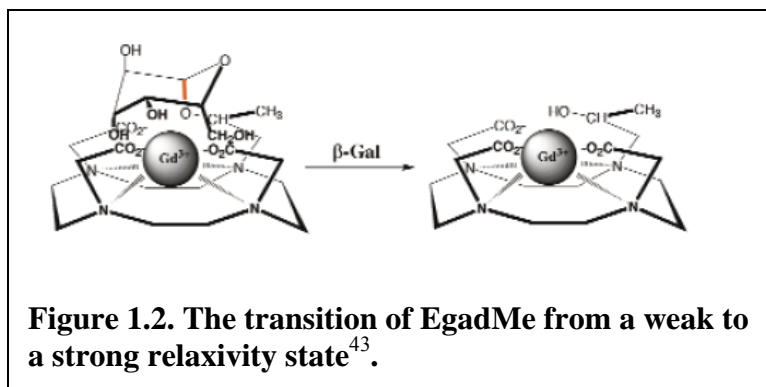
allowing direct interaction of water protons with the metal ion. In other words, the bridge acts as a "switch", which can be used to turn the contrast agent's MR enhancement function on and off. A well known smart MRI contrast agent is EgadMe (Figure 1.2), in which a lalactopyranose ring acts as the "bridge" and can be cleaved by β-galactosidase encoded by he labZ genes[43]. EgadMe was successfully used to image gene expression in vivo[43].

T2 contrast agents usually consist of a crystalline iron-oxide core, surrounded by polymer coatings, which can be polysaccharides, polyethyleneglycol or citrate. These agents are known as superparamagnetic iron-oxide nanoparticles (SPIO). Each iron-oxide nanoparticle contains thousands of iron atoms resulting in very high T2 relaxivities. As a result, as low as micromolar to nanomolar concentrations of T2 agents can be detected, whereas millimolar to micromolar of T1 agents are needed for detection [20]. Nonspecific cellular uptake of T2 contrast agents occurs through phagocytosis and pinocytosis. Targeted imaging using T2 agents is usually achieved by conjugating peptides and proteins to iron-oxide nanoparticles.

SPIO particle sizes range greatly from 2 nm to 3.5 μm[44]. SPIO can be categorized into four groups based on the size: oral SPIO (300 nm to 3.5 μm), standard SPIO (SSPIO, 60-150 nm), ultrasmall SPIO (USPIO, 10-40 nm) and monocrystalline iron-oxide nanoparticles (MION, a subset of USPIO, 10-30 nm)[20,44]. Cross-linked iron oxide (CLIO) is a form of MION, stabilized by a crosslinked aminated dextran. For molecular imaging applications, SPIO molecules are usually less than 50 nm in diameter. Therefore, to avoid confusion, the term SPIO is used to refer to all USPIO, MION and CLIO in this dissertation.

The value of SPIO was first demonstrated in prostate cancer diagnosis by distinguishing healthy lymph nodes (which uptake SPIO into the cells by phagocytosis) and cancerous lymph nodes (no SPIO uptake)[45,46]. Recently, target molecules have been attached to SPIO for molecular imaging. One example is SPIO attached to human protein transferrin to detect breast cancer cells overexpressing the transferrin receptor[47]. There has also been interest in stem cell tracking. In another experiment, SPIO attached with tat peptide was used to label progenitor cells and track their fate in vivo[48]. A number of other SPIO imaging agents have recently been developed to image angiogenesis and apoptosis, processes that are characteristic of diseases including cancer[49,50].

1.4 Radionuclide Imaging

1.4.1 Radionuclide Imaging Principles

Positron emission tomography (PET) is based on detection of decaying radioisotopes, which are neutron deficient and emit positively charged electrons (positrons)[51,52]. The positron can travel a few millimeters in tissue before annihilating with an electron (Figure 1.3). The annihilation produces energy in the form of two high energy (511 keV) γ rays at 180° apart. These γ rays are detected by a scanner with multiple detectors made of scintillation crystals[12]. The scanner determines the site of annihilation and reconstructs a
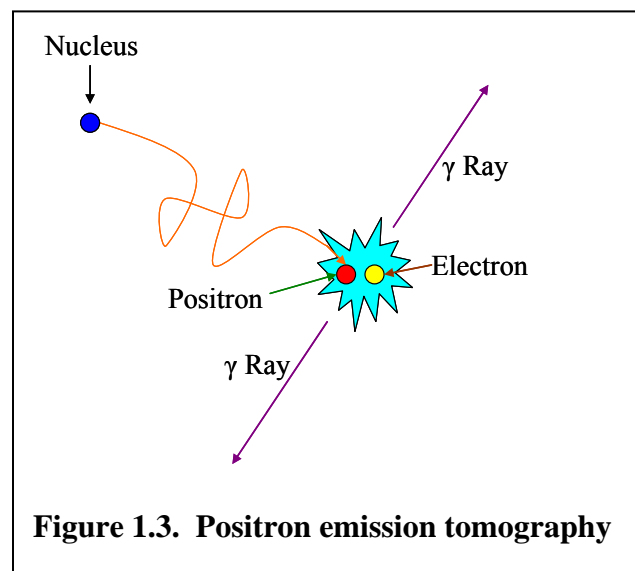
Figure 1.3. Positron emission tomography

9

map of distribution of the radionuclide. Since the positron travels in unpredictable path, PET has very low resolution (4-5 mm)[52]. Frequently used positron-emitting isotopes include ^{18}F, ^{15}O, ^{13}N and ^{11}C. Others less common ones include ^{64}Cu, ^{68}Ga, ^{76}Br, ^{82}Rb, ^{14}O, ^{62}Cu, ^{124}I and ^{94m}Tc[12,53].

Single photon emission computed tomography (SPECT) is similar to PET, but the signal is from gamma-emitting radioisotopes, such as ^{133}Xe, ^{99m}Tc, ^{123}I , ^{131}I and ^{111}In[7,12,54]. The gamma photons are detected by a gamma camera rotating around the subject. The γ emitters used for SPECT are generally more readily available and have longer half-lives ($t_{1/2}$ = hours to days) compared to positron emitters ($t_{1/2}$ = minutes to days) (Table 1.2). However, the spatial resolution of SPECT is rather low (8-12 mm) due to collimation errors and the relatively large size of the detectors[12].

Both PET and SPECT are highly sensitive and the sensitivity is independent of the location depth of the tracer of interest. The sensitivity of PET (10^{-11}-10^{-12} M) is 1 to 2 orders of magnitude greater than that of SPECT (10^{-10} M)[54]. This is due to the fact that PET detectors record simultaneous emission of two photons, whereas SPECT absorbs photon by the mechanical collimator[12]. PET has additional advantages including higher spatial resolution than SPECT and being fully quantitative[55].

The limitation of PET and SPECT include: (1) low spatial resolution, which makes it difficult to assign the signal to specific anatomical-morphological structure; (2)

Table 1.2. Radionuclides half-lives

Imaging Modality	SPECT				PET					
Radionuclide	^{99m}Tc	^{131}I	^{123}I	^{111}In	^{18}F	^{11}C	^{15}O	^{13}N	^{68}Ga	^{64}Cu
Half life	6h	8d	13.2h	2.8d	1.8h	20min	2min	10min	68min	12.7h

short half-life of some radioisotopes for PET, such as ^{11}C ($t_{1/2}$ = 20 minutes) and ^{18}F ($t_{1/2}$ = 110 minutes); (3) exposure to ionizing radiation and production of radioactive waste.

1.4.2 Radionuclide Imaging Agents and Targets

PET and SPECT imaging agents are usually labeled by incorporation of radio isotopes into the probe either covalently (such as ^{18}F and ^{11}C) or noncovalently (such as ^{111}In) using chelators[56]. Due to the high sensitivity of PET and SPECT, most radionuclide imaging agents are given in low doses (subnanomolar)[57]. Radionuclide imaging agents can be divided into two groups: SPECT agents that emit single gamma rays such as ^{99m}Tc, ^{111}In, ^{123}I, and ^{131}I; and PET agents which use positron emitting radionuclides, such as ^{18}F, ^{11}C, ^{15}O, ^{13}N, ^{68}Ga and ^{64}Cu.

Commonly used radionuclides for SPECT have half-lives from 6 hours to 8 days (Table 1.2). These relatively long half-lives allow SPECT agents to be shipped, avoiding the need for cyclotrons and chemistry laboratories nearby. Many SPECT agents have been developed for imaging cancers, cardiac infarction, renal function, receptor binding, transporter function and inflammatory diseases[4]. For example, ^{111}In-D-Phe-DTPA-octreotide and ^{99m}Tc-depreotide were used to image over-expressed sonatostatin receptor in breast carcinoma, lymphoma and neutoendocrine tumors[58-60]. Iodine-131 – pertechnetate and ^{99m}Tc-pertechnetate were applied in diagnosing and targeting therapy of mammary gland abnormalities[61]. Hexakis(2-methoxyisobutyl isonitrile)Tc-99m(I) (^{99m}Tc-Sestamibi) is a widely used radiopharmaceutical to identify adenosine triphosphate-binding cassette (ABC) transporter protein expressed tumors and tissues[62-64]. Tat protein attached with a metal chelator was used to deliver ^{99m}Tc in vivo for cell tracking[65].

Positron-emitting radionuclides, such as ^{18}F and ^{11}C, have also been incorporated into numerous imaging agents. The most well known PET agent is [^{18}F]fluoro-2-deoxy-D-glucose ([18]FDG). [18]FDG is a glucose analog which can be phosphorylated and trapped in cells, whereas glucose itself can be further metabolized to water and carbon dioxide. Due to the increased glucose metabolism rate in cancer cells compared to normal cells, [18]FDG provides great opportunities in cancer imaging[66]. Choline uptake and its phosphorylation are known to be increased in tumor cells as well. Several PET agents, including [^{11}C]Choline, [^{18}F]fluoroethylcholine and [^{18}F]fluoromethylcholine were successfully used to image tumors[56]. Some PET agents can be up-taken by tumor cells based on accelerated protein synthesis, such as [^{11}C]methionin, [^{11}C]tyrosine and [^{18}F]fluorethyl-tyrosine[67]. Tumor proliferation activity can also be investigated based on DNA metabolism using [^{18}F]fluorothymidine ([18]FLT)[68,69], dopamine synthesis using [^{18}F]fluoro-metatyrosine ([18]FDOPA), tumor hypoxia using [^{18}F]fluoromisonidazole ([18]FMISO), hormone receptor expression using 16α[^{18}F]fluoro-17β-oestradial ([18]FES)[70], translocator protein expression using N-(5-fluoro-2-phenoxyphenyl)-N-(2-[^{18}F]fluoromethyl-5-methoxybenzyl)acetamide ([18]FMDAA1106)[71], and reporter gene expression using 8-[^{18}F]fluoropenciclovir ([18]FPCV)[72].

1.5 Optical Imaging

1.5.1 Optical Imaging Principles

Optical imaging is based on fluorescence or bioluminescence. Fluorescence is the absorption of a photon and its subsequent emission at a longer wavelength[73]. Near-infrared (NIR) fluorescence imaging is usually used for in vivo applications because

hemoglobin, water and lipids have lowest absorption coefficient in NIR region (650-900 nm), allowing deep tissue penetration (Figure 1.4)[74,75]. In addition, the autofluorescence from
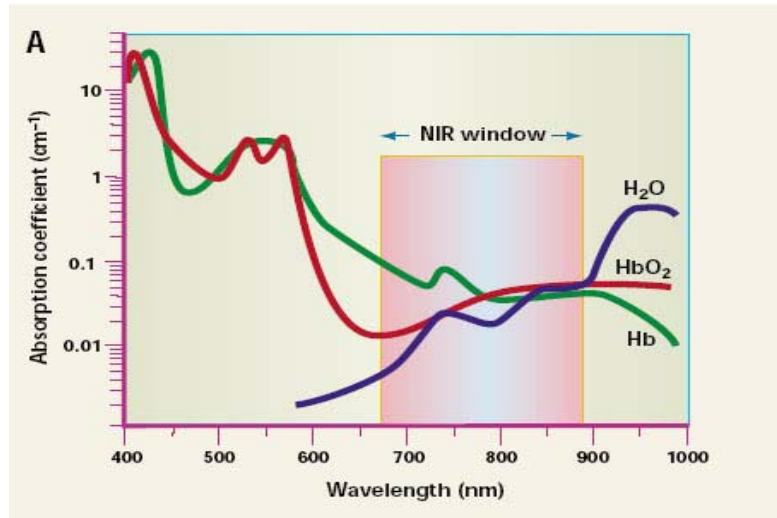
Figure 1.4. Tissue transparency window[75]

the non-targeted area is minimized. NIR fluorescence imaging allows deep tissue imaging up to 10 cm[76]. Bioluminescence on the other hand does not require absorption of light, but arises from the conversion of chemical energy to light. In bioluminescence, luciferase catalyses the oxidation of luciferin, resulting in the release of photons[5]. Because mammalian tissues do not autoluminesce and bioluminescence only occurs when luciferin reacts with luciferase, bioluminescence has zero background signal and high signal to noise ratio[12].

Optical imaging is advantageous in many aspects. It has 1-2 mm spatial resolution (1 μm for intravital microscopy) and possesses nanomolar sensitivity[73]. Compared to other imaging modalities such as MRI, PET, SPECT and US, the instruments are relatively inexpensive. In addition, a variety of imaging probes and signal amplification strategies are available[77]. Optical imaging also allows multichannel imaging using multiple probes with different spectral properties and co-registration of surface anatomical information with molecular information[7].

Optical imaging is limited due to its surface-weighted nature, as well as tissue absorption and autofluorescence. These limitations can be partially resolved by NIR fluorescence imaging or fluorescence molecular tomography (FMT). In FMT a subject is rotated within an array of emitter and detectors[76]. The detected fluorescence, which is spatially recorded, is subsequently reconstructed tomographically, resulting in a quantitative three dimensional map. Penetration depths of 7-14 cm are theoretically achievable using appropriate fluorochromes in FMT[77]. The main limitation of bioluminescence imaging is that absolute quantification of target signal is not possible.

1.5.2 Optical Imaging Agents and Targets

Optical imaging is a rapid, inexpensive and sensitive approach for in vitro and in vivo study of biochemical and biological processes, and is the main focus in this dissertation. Optical imaging agents are usually prepared by conjugating a specific ligand to a fluorochrome. Several types of optical imaging agents have been developed, including fluorescence agents (such as NIR agents), bioluminescence agents, and quantum dots.

1.5.2.1 Fluorescence Agents

Both endogenous and exogenous fluorescent agents have been discovered for optical imaging. All tissue contains fluorophores that absorb light and subsequently emit fluorescence at a longer wavelength[78]. Several well known endogenous tissue fluorophores include nicotinamide adenine dinucleotide (NAD[H]), elastin, collagen, and flavins[78,79]. Changes in concentration or distribution of these endogenous fluorophores are believed to correlate with changes in histology[80,81]. While promising as a diagnostic tool, these signatures are limited in early lesion detection due to low signal to noise (S/N)

stemming from a relatively low signal (small changes in concentration of the endogenous fluorophores detected in early disease) and a large background (scattering, reflected light etc.).

Because of the limitations of endogenous fluorophores in early disease detection, the use of exogenous fluorescence agents has currently experienced an expanded level of attention. Exogenous fluorescence agents can be generally classified as perfusion and targeted agents. Perfusion agents are nonspecific, usually smaller molecules, which have vascular distribution with leakage into the extracellular space. They increase contrast of pathology by differential rates of tissue/tumor perfusion or vascular leakage. However, perfusion agents are usually limited in molecular imaging due to low S/N ratio and the lack of any specific molecular information[82]. Targeted fluorescent agents usually have targeting functionalities, such as receptor ligands, antibodies and peptides, allowing increased localization of imaging agents in diseased tissues and reduced agents' uptake in normal tissues.

Most exogenous fluorescent agents utilize fluorescent dyes as signaling moieties. Some commonly used fluorescent dyes include fluorescein, rhodamine and cyanine dyes. Fluorescein is a green dye with excitation at 494 nm and emission at 521 nm. A well known fluorescein derivative is fluorescein isothiocyanate (FITC), which has isothiocyanate group (-N=C=S) for conjugation. Fluorescein dyes are limited in optical imaging due to the green autofluorescence from skin and viscera, high hemoglobin absorption, and strong tissue scattering. Rhodamine is a family of red dyes. An example is lissamine rhodamine B sulfonyl chloride, which absorbs at 568 nm and emits at 583 nm in methanol. With the sulfonyl chloride group, this rhodamine dye allows easy

conjugation to specific ligands. Compared to fluorecein dyes, rhodamine dyes are red-shifted, allowing reduced tissue autofluorescence, absorption and scattering. However, lissamine dyes are not optimal for in vivo imaging neither, due to relatively low tissue penetration compared to NIR dyes.

Most NIR dyes belong to the cyanine dye family (Figure 1.5). Cyanine dyes represent one of the most prominent classes of optical imaging agents with adjustable optical properties

Figure 1.5. General structure of cyanine dye
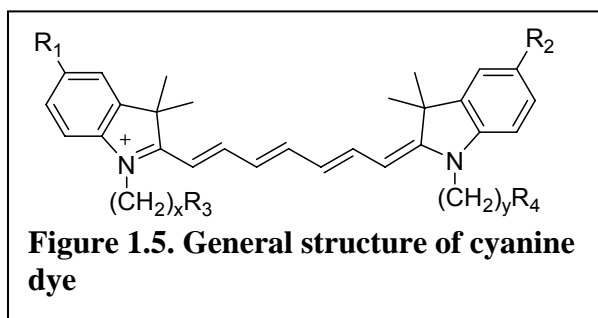
and high extinction coefficients. The absorption and emission ranges throughout the visible to the NIR range[78,83]. At the same time, cyanine dyes can be conjugated to targeting ligands, imparting molecular specificity. There are many commercially available cyanine dyes, such as indocyanine green (ICG), Cy5, Cy5.5, Cy7, IRDye[TM] 700DX, IRDye[TM] 800RS and IRDye[TM] 800CW.

ICG (Figure 1.6) is one example of a clinically approved perfusion cyanine dye. It has very low toxicity in humans with only one known adverse reaction (rare anaphylaxis)[84]. ICG has been used clinically for many years to test hepatic function[85], cardiac physiology[86] and fluorescence angiography in ophthalmology[87]. Moreover, cancer imaging was proven to be somewhat feasible using ICG[88-90].

Recently, several improved heptamethine indocyanine dyes have become available. Figure 1.6 shows one example, IRDye[TM] 800CW NHS ester (LI-COR Biosciences, Lincoln, NE). This molecule has four sulfonate (SO_3^-) groups rather than two in ICG, which increases water solubility and aqueous quantum yield (QY). Moreover,

ICG   IRDye^TM 800CW NHS ester

Figure 1.6. Structure of ICG and IRDye^TM 800CW NHS ester
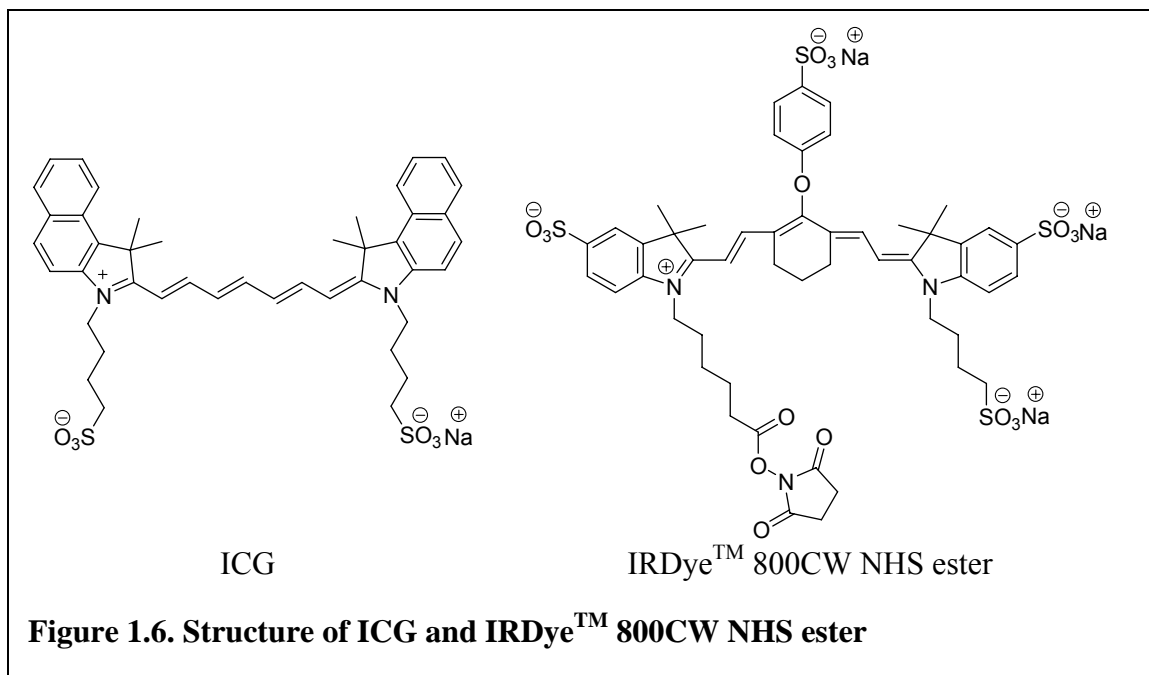
the N-hydroxysuccinimide (NHS) ester allows covalent conjugation to targeting ligands.

NIR targeting agents have been widely used to target cancer. These agents are usually synthesized by coupling NIR dyes to antibodies, peptides or small targeting ligands. For example, an angiogenesis associated antibody was labeled with Cy7 for diagnostic imaging of cancer[91]. Another study exploited the folate receptor for cancer specific targeting using NIR2-folate conjugate[92]. Somatostatin receptor was targeted for cancer imaging as well, using cypate-peptide complex[93], and indodicarbocyanine (IDCC) or indotricarbocyanine (ITCC) labeled peptide[94,95]. Similarly, ITCC was tagged with transferrin (Tf) or human serum albumin (HSA) for the detection of tumors. Recently, epidermal growth factor (EGF) was labeled with Cy5.5[96] or IRDye^TM 800CW[97,98] to target the EGF receptor (EGFr), over-expressed in breast, lung, ovary, brain and prostate tumors. In a similar way, vascular endothelial growth factor (VEGF, involved in angiogenesis)[99], and annexin V (related to apoptosis)[100-102] were labeled with cyanine

17

dyes to image tumors. Cancer cells can also be imaged due to their increased glucose metabolism rate, using NIR dye labeled sugars, such as pyropheophorbide 2-deoxyglucosamide (Pyro-2DG)[103], Cy5.5-D-glucosamine (Cy5.5-2DG)[104] and multivalent carboncyanine-glucosamine[105]. Using low quantities of these NIR agents, high specificity and good tissue penetration can be achieved. However, relatively low signal-to-background ratio is sometimes seen due to the signal from un-bound NIR agents.

Auto-quenched NIR agents that become detectable upon enzyme activation can increase signal-to-background ratios up to several hundred folds[8,106]. An example is shown in Figure 1.7[56,107]. Urokinase plasminogen activator (uPA) and uPA receptor
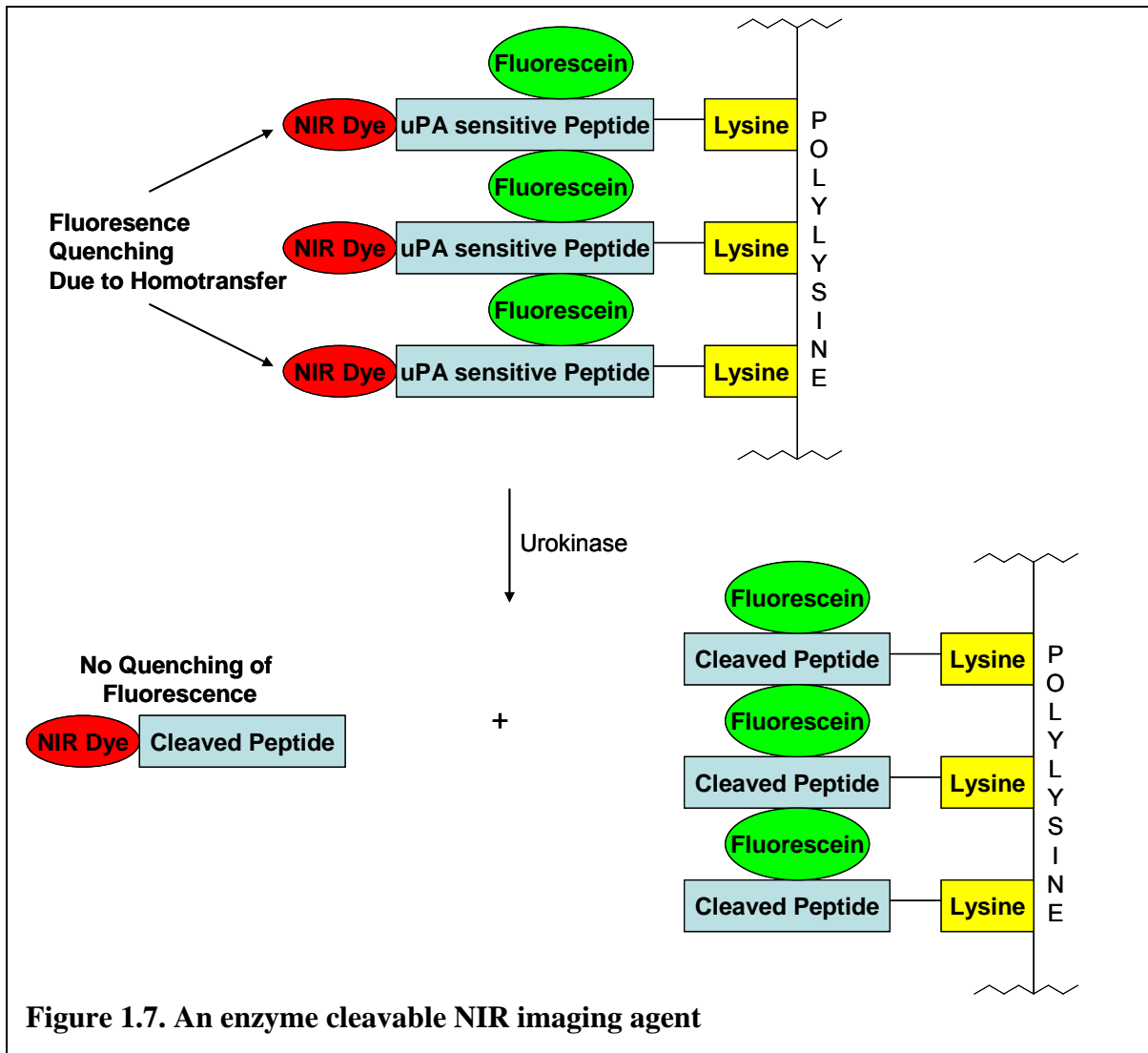
Figure 1.7. An enzyme cleavable NIR imaging agent

facilitate cancer cell invasion into surrounding tissues. Overexpression of uPA is also

found in various cancers. Weissleder and coworkers designed a probe which consists of

multiple peptide (uPA substrate) motifs capped with Cy5.5 or Cy7 and a poly-lysine

backbone[107]. Due to the crowding of NIR dyes, the fluorescence of the dye is quenched.

When the agent reacts with urokinase, the enzyme cleaves the peptide and releases the

NIR dye from the polymer. As a consequence, fluorescence of the dye is recovered and

signal intensity is amplified. Using similar techniques, many smart NIR agents have been

developed and used to target cathepsin B, K, D and H; caspase 1 and 3; matrix

metalloproteinases (MMP) 2, 9, and 13; urokinase and other proteases for cancer

imaging[8,10,56].

1.5.2.2 Bioluminescence Agents

Bioluminescence contrast agents are based
on luciferin (Figure 1.8). Upon meeting luciferase,
bioluminescence agents are oxidized in the
presence of oxygen and adenosine triphosphate

Figure 1.8. Structure of luciferin
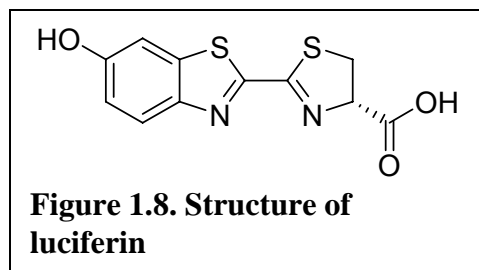
(ATP), and emit light. Compared to fluorescence agents, bioluminescence agents provide

high signal-to-background ratio, as there is no inherent background with bioluminescence.

Numerous bioluminescence agents exist in nature, such as firefly luciferin in male firefly

and other luciferins in sponges, corals, jellyfish, clams and several types of fish[77]. Firefly

luciferin has an emission at 562 nm with good quantum yield (90%)[108], thus becoming

the most commonly used substrate for in vivo bioluminescence imaging[109-111]. A variety

of synthetic luciferins have been developed as well for studying enzyme activities[112-115].

Chemical modification of the 6-hydroxyl group of luciferin seems to be an effective

19

means to approach bioluminescent assays for enzymes of interest.

1.5.2.3 Quantum Dots

Semiconductor quantum dots (QDs) have attractive optical and electronic properties. Compared to organic fluorophores, QDs have several unique advantages: (1) QDs are highly resistant to irreversible photo-oxidation photobleaching, whereas organic fluorophores are sensitive to local environment and can undergo photobleaching; (2) QDs' emission wavelengths can be easily tuned from blue to near infrared by changing size and composition. (3) QDs have improved brightness due to high molar extinction coefficients; (4) because of the broad excitation spectra and narrow emission profile, QDs can be excited with a single light source and emit light with different colors, making multicolor labeling possible[116-119]. However, due to the hydrophobic surfaces, most QDs are challenged by biocompatibility in imaging studies[120]. Some water soluble QDs have been developed, but most of them suffer from decreased quantum efficiency, aggregation, high cost and instability[121].

QDs are typically synthesized at high temperatures in organic solvents and consist of an inorganic core and inorganic shell of metal (Figure 1.9). For in vitro and in vivo imaging applications, QDs are usually solubilized by aqueous-compatible organic

Figure 1.9. Quantum dots
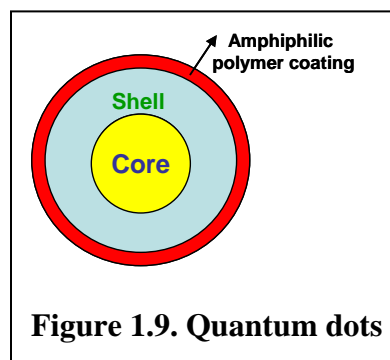
layer. Both group II-VI (e.g. CdSe, CdTe, CdS, and ZnSe) and group III-V (e.g. InP and InAs) nanocrystals have been used as the core[116,122]. A thin layer of semiconductor material, such as ZnS and CdS, is often grown on top of the core to protect the core surface from oxidation and increase the quantum yield[123]. The resulting particle is only

soluble in organic solvents. For biological imaging, QDs must be additionally coated with amphiphilic polymers with both a hydrophobic moiety (such as hydrocarbons) and a hydrophilic segment (such as carboxylate, amine and thiol groups)[117]. These hydrophilic groups allow easy bioconjugation to targeting molecules, such as receptor ligands, peptides and DNA.

Bioconjugated QDs have been imaged in numerous biologically and clinically relevant studies, such as cell trafficking[124], in vivo cancer imaging[125], immunoassay[126,127], DNA hybridization[128], and receptor-mediated endocytosis[126]. Lidke, Jovin and their coworkers coupled EGF to quantum dots to study receptor tyrosine kinase (RTK) mediated signal transduction in various cancer cells lines[129]. Gao et al. developed QDs with triblock polymers to incorporate tumor-targeting ligands for in vivo prostate cancer imaging[125]. Dahan and colleagues visualized single-molecule movement in single living cells using a primary antibody, biotinilated anti-mouse Fab fragments, and streptavidin-coated QDs[130]. Kim and coworkers used polydentate phosphine coated NIR QDs to guide real time resection of sentinel lymph nodes[131]. Some recent studies show that QDs labeled cells can be tracked over extended period of time (up to several months)[129,132,133]. Overall, QDs hold great promise for biological and clinical applications, especially in the imaging of cancers.

1.6 Ultrasound

1.6.1 Ultrasound Principles

Ultrasound imaging uses high frequency sound waves as the signal source. The sound waves are emitted from a transducer placed against the skin and reflected back

21

from the internal organs under examination[7,134]. Sound waves are altered by traveling through tissues, thus providing different acoustic signatures for different tissues. The image contrast depends on sound attenuation, sound speed, backscatter and imaging algorithm used[7]. Clinical ultrasound uses frequencies from 2-15 MHz and yields images with a spatial resolution of 300-500 μm[7]. Ultrasound biomicroscopy works at 40-60 MHz frequency and can be used to image vessels with 15-40 μm diameters[3].

Ultrasound is the most commonly used clinical imaging modality due to the high sensitivity, good surface resolution, low cost, availability and safety. Ultrasound is widely applied in cardiac, fetal, vascular and abdominal imaging. The real-time nature of ultrasound also facilitates its application in image-guided injection procedures. Furthermore, small anatomical structures at the embryonic and early postnatal stages can be visualized using ultrasound biomicroscopy[7]. In addition, recent development of ultrasound contrast agents has enabled ultrasound to be applied in liver lesions characterization, blood pool enhancement and perfusion imaging[135].

Ultrasound is mainly limited by poor resolution in deep tissues and image shadowing. Spatial resolution of ultrasound decreases rapidly with depth, thus unable to provide details about deep tissues. Moreover, targeted ultrasound imaging is limited by the availability and stability of contrast agents[5].

1.6.2 Ultrasound Agents and Targets

Ultrasound contrast agents are usually micrometer-sized gas-filled microbubbles. The most commonly used gases include perfluorocarbons, such as octafluoropropane (C_3F_8), decafluorobutane (C_4F_{10}), and sulfur hexafluoride (SF_6)[135]. To improve in vivo stability, microbubbles are usually encapsulated with shells composed of lipids, proteins

or polymers[4,135]. The microbubbles vibrate strongly in response to ultrasound waves and produce strong backscattered acoustic signal that can be detected. Since microbubbles are several thousand times as reflective as normal tissue, the amount of ultrasound contrast agent needed is rather small (a single microbubble with micrometer diameter can be detected)[4]. Though sensitive and inexpensive, ultrasound imaging using microbubbles is challenged with low spatial resolution and instability of contrast agents[135].

Unlike the small imaging agents used in MR, nuclear and optical imaging, microbubbles do not normally leave the vascular space, thus are intravascular tracers. Microbubbles are widely used clinically for blood pool enhancement and perfusion imaging[135].

Recently, targeted ultrasound imaging agents have been developed based on microbubbles. There are two strategies to synthesize targeted microbubbles. The first one is to modify the microbubble shell to facilitate the attachment of microbubbles to disease-related cells. Lindner and collegues incorporated negatively charged phospholipids phospatidylserine into microbubble shell. The resulting microbubbles were able to attach to and get phagocytosed by activated leukocytes, thus providing opportunities in imaging of inflammation [136-138]. The other strategy involves attaching target-specific ligands, such as monoclonal antibodies, asialoglycoproteins, polysaccharides, peptides and aptamers, to the microbubble shell[135,139]. For example, alpha (v)-integrin targeted microbubble-antiobody complex has been developed to study angiogenesis, which is associated with plaque inflammation and tumor growth[140]. In another study, microbubbles with GPIIIbIIIa receptor targeted peptide were successfully used to image intravascular thrombi in vitro and in vivo[141].

1.7 Computed Tomography

Computed tomography (CT) is based on the fact that tissues absorb X-rays differently[142]. Recent development of CT is micro CT, which allows high-resolution imaging of small animals[143-145]. Image resolution is on 50-100 µm and data acquisition takes 5 to 30 minutes.

Despite the high spatial resolution and fast acquisition, CT suffers from poor soft tissue contrast and low inherent sensitivity[6,7]. CT is mainly used as a complementary modality to other modalities, particularly nuclear imaging modalities. CT addresses low spatial resolution issue of PET/SPECT by the introduction of nuclear/CT fusion systems, such as PET-CT and SPECT-CT. These systems integrate molecular information from PET or SPECT with anatomical details from CT and are playing an increasing role in molecular imaging[6,55,146].

1.8 Multimodality Imaging

As discussed, each imaging modality has its limitations. These limitations can be resolved by incorporation of multiple imaging modalities. For example, optical imaging is highly sensitive, but limited by surface-weighted nature. On the other hand, MRI is not limited to tissue penetration, but has very low sensitivity. Incorporation of optical imaging and MRI will take advantage of both high sensitivity (optical imaging) and deep tissue penetration (MRI). Moreover, preoperative MRI contrast and intraoperative optical signal from the same targets can be applied to improve surgical outcome. Multimodality imaging can potentially provide anatomic information, as well as functional, metabolic or molecular information simultaneously.

Due to the superior nature of multimodality imaging, significant effort has been placed into development of multimodal imaging agents during the last decade. Meade and coworkers synthesized bifunctional optical/MR imaging agents that possess multiple Gd^{3+} chelators and fluorescent tetramethylrhodamine attached to poly-lysine or dextran[147]. These bimodal agents were used to study cell divisions and cell lineage distributions of developing embryos. However, these agents are limited in animal studies as tetramethylrhodamine is not a NIR dye. Weissleder and collegues developed a smart NIR/MRI agent by attaching Cy5.5-derivatized peptides to the surface of cross-linked iron oxide (CLIO) nanoparticle[148]. Fluorescence signal is amplified when the peptides are cleaved by certain enzymes. This smart nanopartical, Cy5.5-CLIO allowed delineation of brain tumors both by preoperative magnetic resonance imaging and by intraoperative optical imaging[149].

Other than bimodal optical/MRI imaging agents, other multimodal probes have been investigated as well. For example, Achilefu and coworkers developed NIR/SPECT agents consisting of heptamethine carbocyanine and ^{111}In-DOTA[150]. An agent consisting of liposomes co-encapsulating iohexol (an iodine based CT agent) and gadoteridol (an Gd^{3+} based MR agent) was developed for CT/MR imaging[151]. Other combinations of optical, nuclide, MR, ultrasound and CT imaging agents are being developed to produce multimodal images[7].

Our group has developed a cocktail approach of multimodal imaging agents[152,153]. This cyclen-based tri-
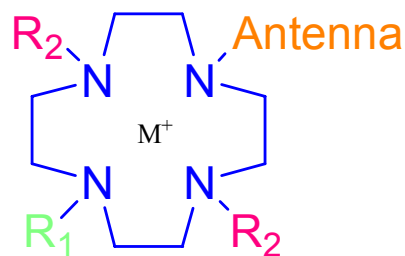
Figure 1.10. Cocktail approach of multimodal imaging agent. R_1: conjugation arm; R_2: chelating arm.

functional agent (Figure 1.10) consists of two chelating arms (R_2) for metal ion chlation, one antenna that can sensitize light and transfer energy to chelated metal, and one conjugation arm which is used to couple target-specific ligands. This kind of agent's emission is far from the absorption ($\Delta\lambda \geq 280$ nm). Moreover, fluorescent lifetimes are rather long (0.5–3.5 ms). As a result, background signal is reduced to low level[154]. Another advantage of this tri-funtional imaging agent is that synthetic modifications on this agent can yield tunable spectroscopic and physical properties. For example, pendant arm modifications can change complex water solubility and antenna modifications can change absorption property. By chelating different metals, this agent is detectable by optical imaging (such as Eu^{3+} and Tb^{3+}), PET imaging (such as $^{64}Cu^{2+}$ and $^{68}Ga^{3+}$), MRI (such as Gd^{3+}), and SPECT (such as $^{111}In^{3+}$). A multimodal imaging approach is achieved by mixing the agent with different metal ions. One agent developed possesses two phosphorous acid pendant arms for strong chelating ability, an energy absorbing/ transmitting quinoline chromophore as antenna, and a carboxylic acid conjugation arm. By coupling this agent to a peripheral benzodiazepine receptor (PBR) ligand, the resulting imaging agents chelated with Eu^{3+} and Gd^{3+} were successfully imaged by optical imaging and MRI to study C6 glioma cells[153].

1.9 Dissertation Overview

The ultimate success of molecular imaging depends heavily upon discovery of selective imaging probes. This dissertation is focused on development, characterization and in vitro/in vivo imaging of novel imaging agents that target glucose metabolism, translocator protein or cannabinoid CB_2 receptor.

Chapter II illustrates NIR-glucosamine as an [^{18}F]fluoro-2-deoxy-D-glucose (^{18}FDG) analog. ^{18}FDG is widely used clinically as a PET agent, however, ^{18}FDG-PET imaging technique is limited due to low spatial resolution, exposure to ionizing radiation, short half life of ^{18}F (110 minutes), requirement of a local cyclotron and difficulty of compound synthesis. In chapter II, the synthesis and characterization of an ^{18}FDG analog, NIR-glucosamine, is first shown. Next, stability of NIR-glucosamine in various solutions is presented. At the end of this chapter, quantitative in vitro and in vivo assessment of NIR-glucosamine in an SW480 mouse model of human colorectal adenocarcinoma is discussed.

Chapter III presents a novel conjugable translocator protein (TSPO) ligand, C_6Ro5-4864. TSPO is an attractive target for cancer imaging as it is overexpressed in a variety of tumors. This chapter describes the synthesis and characterization of C_6Ro5-4864 and a fluorescence dye labeled C_6Ro5-4864, LissRo5. The specific binding of LissRo5 to translocator protein was verified by binding study, live cell competition, and in vitro imaging.

Chapter IV describes another novel conjugable TSPO ligand, n-TSPOmbb732. n-TSPOmbb732 is a analog of DAA1106, which binds to TSPO with picomolar binding affinity. This chapter starts with the development of a series of seven n-TSPOmbb732 (n=3-9) molecules and corresponding structure activity relationship (SAR) studies. Following this, synthesis, characterization, binding studies and in vitro imaging of three fluorescence dye labeled 6-TSPOmbb732 (n-TSPOmbb732 with 6 carbon linker), including NIR6T, Liss6T and cypate6T, are presented. At last, the prospect of three

lanthanide chelate labeled 6-TSPOmbb732 for multimodality imaging or PET imaging is discussed.

Chapter V shows a cancer drug-6-TSPOmbb732 complex for enhanced cancer therapy. The synthesis and characterization of etoposide-6-TSPOmbb732 (Et6T) is presented, followed by cytotoxicity study on breast cancer and glioma cells.

Chapter VI illustrates synthesis and characterization of a functional cannabinoid CB_2 receptor ligand, mbc94. CB_2 receptor is an attractive target for immune system imaging and therapy. This chapter first describes the development of mbc94, which is the first fully conjugable CB_2 receptor ligand. The preparation and in vitro imaging of a NIR dye labeled mbc94, NIRmbc94, is then discussed. At the end of this chapter, competition and saturation binding studies are shown to evaluate NIRmbc94 as a potent CB_2 receptor targeted imaging agent.

1.10 References

(1)   Weissleder R, M. U. Molecular imaging. *Radiology* **2001**, *219*, 316-333.

(2)   Gross, S.; Piwnica-Worms, D. Spying on cancer: Molecular imaging in vivo with genetically encoded reporters. *Cancer Cell* **2005**, *7*, 5-15.

(3)   Pomper, M. G. Molecular imaging: An overview. *Academic Radiology* **2001**, *8*, 1141-1153.

(4)   Miller, J. C.; Thrall, J. H. Clinical molecular imaging. *Journal of the American College of Radiology* **2004**, *1*, 4-23.

(5)   Wunder, A.; Straub, R. H.; Gay, S.; Funk, J.; Muller-Ladner, U. Molecular imaging: novel tools in visualizing rheumatoid arthritis. *Rheumatology* **2005**, *44*, 1341-1349.

(6)   Hengerer, A.; Wunder, A.; Wagenaar, D. J.; Vija, A. H.; Shah, M. et al. From genomics to clinical molecular imaging. *Proceedings of the Ieee* **2005**, *93*, 819-828.

(7)   Massoud, T. F.; Gambhir, S. S. Molecular imaging in living subjects: seeing fundamental biological processes in a new light. *Genes & Development* **2003**, *17*, 545-580.

(8)   Weissleder, R.; Mahmood, U. Molecular imaging. *Radiology* **2001**, *219*, 316-333.

(9)   Weissleder, R. Scaling down imaging: molecular mapping of cancer in mice. *Nature Reviews Cancer* **2002**, *2*, 11-19.

(10)   Weissleder, R.; Tung, C. H.; Mahmood, U.; Bogdanov, A. In vivo imaging of tumors with protease-activated near-infrared fluorescent probes. *Nature Biotechnology* **1999**, *17*, 375-378.

(11)   Longmore, D. B. The Principles of Magnetic-Resonance. *British Medical Bulletin* **1989**, *45*, 848-880.

(12)   Cassidy, P. J.; Radda, G. K. Molecular imaging perspectives. *Journal of the Royal Society Interface* **2005**, *2*, 133-144.

(13)   Jasanoff, A. Functional MRI using molecular imaging agents. *Trends in Neurosciences* **2005**, *28*, 120-126.

(14)   Serfaty, J. M.; Yang, X. M.; Aksit, P.; Quick, H. H.; Solaiyappan, M. et al. Toward MRI-guided coronary catheterization: Visualization of guiding, catheters, guidewires, and anatomy in real time. *Journal of Magnetic Resonance Imaging* **2000**, *12*, 590-594.

(15)   Schneider, J. E.; Bamforth, S. D.; Grieve, S. M.; Clarke, K.; Bhattacharya, S. et al. High-resolution, high-throughput magnetic resonance imaging of mouse embryonic anatomy using a fast gradient-echo sequence. *Magnetic Resonance Materials in Physics Biology and Medicine* **2003**, *16*, 43-51.

(16)   Jacobs, R. E.; Papan, C.; Ruffins, S.; Tyszka, J. M.; Fraser, S. E. MRI: volumetric imaging for vital imaging and atlas construction. *Nature Cell Biology* **2003**, Ss10-Ss16.

(17)   Aime, S.; Cabella, C.; Colombatto, S.; Crich, S. G.; Gianolio, E. et al. Insights into the use of paramagnetic Gd(III) complexes in MR-molecular imaging investigations. *Journal of Magnetic Resonance Imaging* **2002**, *16*, 394-406.

(18)   Artemov, D. Molecular magnetic resonance imaging with targeted contrast agents. *Journal of Cellular Biochemistry* **2003**, *90*, 518-524.

(19)   Lin, Y. J.; Koretsky, A. P. Manganese ion enhances T-1-weighted MRI during brain activation: An approach to direct imaging of brain function. *Magnetic Resonance in Medicine* **1997**, *38*, 378-388.

(20)   Gimi, B.; Pathak, A. P.; Ackerstaff, E.; Glunde, K.; Artemov, D. et al. Molecular imaging of cancer: Applications of magnetic resonance methods. *Proceedings of the Ieee* **2005**, *93*, 784-799.

(21)   Magerstadt, M.; Gansow, O. A.; Brechbiel, M. W.; Colcher, D.; Baltzer, L. et al. Gd(Dota) - an Alternative to Gd(Dtpa) as a T1,2 Relaxation Agent for Nmr Imaging or Spectroscopy. *Magnetic Resonance in Medicine* **1986**, *3*, 808-812.

(22)   Bousquet, J. C.; Saini, S.; Stark, D. D.; Hahn, P. F.; Nigam, M. et al. Gd-Dota - Characterization of a New Paramagnetic Complex. *Radiology* **1988**, *166*, 693-698.

(23)   Meyer, D.; Schaefer, M.; Bonnemain, B. Gd-Dota, a Potential Mri Contrast Agent Current Status of Physicochemical Knowledge. *Investigative Radiology* **1988**, *23*, S232-S235.

(24)   Manelfe, C.; Berry, I.; Arrue, P. Gd-Dota Enhanced Mr Imaging of Spinal-Cord Tumors. *American Journal of Neuroradiology* **1988**, *9*, 1006-1006.

(25)   Hodler, J.; Orellano, J.; Thurnher, S.; Marincek, B.; Vonschulthess, G. K. Gd-Dota in Musculoskeletal Diseases. *Fortschritte Auf Dem Gebiete Der Rontgenstrahlen Und Der Neuen Bildgebenden Verfahren* **1990**, *153*, 535-539.

(26)   Bonnet, P. A.; Michel, A.; Fernandez, J. P.; Cyteval, C.; Rifai, A. et al. The Use of Gd-Dota in Magnetic-Resonance-Imaging of Experimentally Induced Mammary-Tumors. *Magnetic Resonance Imaging* **1990**, *8*, 71-77.

(27)   Soyer, P.; Tidjani, K.; Laissy, J. P.; Sibert, A.; Menu, Y. Dynamic Gd-Dota-Enhanced Mr-Imaging of Hepatic Metastases from Pancreatic Neuroendocrine Tumors. *European Journal of Radiology* **1994**, *18*, 180-184.

(28)   Niemi, P.; Paajanen, H.; Kormano, M.; Alanen, A.; Maattanen, H. et al. Mr Imaging of Experimental Intramuscular Hemorrhage at 0.02-T - Contrast Enhancement with Gd-Dota. *Acta Radiologica* **1990**, *31*, 455-459.

(29)   Hervesomma, C. M. P.; Sebag, G. H.; Prieur, A. M.; Bonnerot, V.; Lallemand, D. P. Juvenile Rheumatoid-Arthritis of the Knee - Mr Evaluation with Gd-Dota. *Radiology* **1992**, *182*, 93-98.

(30)   Mcnamara, M. T.; Ehman, R. L.; Revel, D.; Sievers, R.; Brasch, R. C. et al. The Use of Gd-Dtpa as a Perfusion Marker for Magnetic-Resonance Imaging. *Circulation* **1984**, *70*, 170-170.

(31)   Burai, L.; Hietapelto, V.; Kiraly, R.; Toth, E.; Brucher, E. Stability constants and H-1 relaxation effects of ternary complexes formed between Gd-DTPA, Gd-DTPA-BMA, Gd-DOTA, and Gd-EDTA and citrate, phosphate, and carbonate ions. *Magnetic Resonance in Medicine* **1997**, *38*, 146-150.

(32)   Runge, V. M.; Gelblum, D. Y.; Pacetti, M. L.; Carolan, F.; Heard, G. Gd-Hp-Do3a in Clinical Mr Imaging of the Brain. *Radiology* **1990**, *177*, 393-400.

(33)   Sipkins, D. A.; Cheresh, D. A.; Kazemi, M. R.; Nevin, L. M.; Bednarski, M. D. et al. Detection of tumor angiogenesis in vivo by alpha(v)beta(3)-targeted magnetic resonance imaging. *Nature Medicine* **1998**, *4*, 623-626.

(34)   Curtet, C.; Maton, F.; Havet, T.; Slinkin, M.; Mishra, A. et al. Polylysine-Gd-DTPA(n) and polylysine-Gd-DOTA(n) coupled to anti-CEA F(ab ')(2) fragments as potential immunocontrast agents - Relaxometry, biodistribution, and magnetic resonance imaging in nude mice grafted with human colorectal carcinoma. *Investigative Radiology* **1998**, *33*, 752-761.

(35)   Lee, S. S.; Goo, H. W.; Bin Park, S.; Lim, C. H.; Gong, G. Y. et al. MR Imaging of reperfused myocardial infarction: Comparison of necrosis-specific and intravascular contrast agents in a cat model. *Radiology* **2003**, *226*, 739-747.

(36)   Konda, S. D.; Wang, S.; Brechbiel, M.; Wiener, E. C. Biodistribution of a Gd-153-folate dendrimer, generation=4, in mice with folate-receptor positive and negative ovarian tumor xenografts. *Investigative Radiology* **2002**, *37*, 199-204.

(37)   Corot, C.; Schaefer, M.; Beaute, S.; Bourrinet, P.; Zehaf, S. et al. Physical, chemical and biological evaluations of CMD-A2-Gd-DOTA - A new paramagnetic dextran polymer. *Acta Radiologica* **1997**, *38*, 91-99.

(38)   Aime, S.; Botta, M.; Frullano, L.; Crich, S. G.; Giovenzana, G. B. et al. Contrast agents for magnetic resonance imaging: A novel route to enhanced relaxivities

based on the interaction of a Gd-III chelate with poly-beta-cyclodextrins. *Chemistry-a European Journal* **1999**, *5*, 1253-1260.

(39) Lu, Z. R.; Wang, X. H.; Parker, D. L.; Goodrich, K. C.; Buswell, H. R. Poly(L-glutamic acid) Gd(III)-DOTA conjugate with a degradable spacer for magnetic resonance imaging. *Bioconjugate Chemistry* **2003**, *14*, 715-719.

(40) Langereis, S.; de Lussanet, Q. G.; van Genderen, M. H. P.; Meijer, E. W.; Beets-Tan, R. G. H. et al. Evaluation of Gd(III)DTPA-terminated poly(propylene imine) dendrimers as contrast agents for MR imaging. *Nmr in Biomedicine* **2006**, *19*, 133-141.

(41) Bryant, L. H.; Jordan, E. K.; Bulte, J. W. M.; Herynek, V.; Frank, J. A. Pharmacokinetics of a high-generation dendrimer-Gd-DOTA. *Academic Radiology* **2002**, *9*, S29-S33.

(42) Rudovsky, J.; Botta, M.; Hermann, P.; Hardcastle, K. I.; Lukes, I. et al. PAMAM dendrimeric conjugates with a Gd-DOTA phosphinate derivative and their adducts with polyaminoacids: The interplay of global motion, internal rotation, and fast water exchange. *Bioconjugate Chemistry* **2006**, *17*, 975-987.

(43) Louie, A. Y.; Huber, M. M.; Ahrens, E. T.; Rothbacher, U.; Moats, R. et al. In vivo visualization of gene expression using magnetic resonance imaging. *Nature Biotechnology* **2000**, *18*, 321-325.

(44) Thorek, D. L. J.; Chen, A.; Czupryna, J.; Tsourkas, A. Superparamagnetic iron oxide nanoparticle probes for molecular imaging. *Annals of Biomedical Engineering* **2006**, *34*, 23-38.

(45) Harisinghani, M. G.; Barentsz, J.; Hahn, P. F.; Deserno, W. M.; Tabatabaei, S. et al. Noninvasive detection of clinically occult lymph-node metastases in prostate cancer. *New England Journal of Medicine* **2003**, *348*, 2491-U2495.

(46) Mack, M. G.; Balzer, J. O.; Straub, R.; Eichler, K.; Vogl, T. J. Superparamagnetic iron oxide - Enhanced MR imaging of head and neck lymph nodes. *Radiology* **2002**, *222*, 239-244.

(47) Weissleder, R.; Moore, A.; Mahmood, U.; Bhorade, R.; Benveniste, H. et al. In vivo magnetic resonance imaging of transgene expression. *Nature Medicine* **2000**, *6*, 351-354.

(48) Lewin, M.; Carlesso, N.; Tung, C. H.; Tang, X. W.; Cory, D. et al. Tat peptide-derivatized magnetic nanoparticles allow in vivo tracking and recovery of progenitor cells. *Nature Biotechnology* **2000**, *18*, 410-414.

(49) Kang, H. W.; Josephson, L.; Petrovsky, A.; Weissleder, R.; Bogdanov, A. Magnetic resonance imaging of inducible E-selectin expression in human endothelial cell culture. *Bioconjugate Chemistry* **2002**, *13*, 122-127.

(50)   Schellenberger, E. A.; Hogemann, D.; Josephson, L.; Weissleder, R. Annexin V-CLIO: A nanoparticle for detecting apoptosis by MRI. *Academic Radiology* **2002**, *9*, S310-S311.

(51)   Hoffman, E. J.; Phelps, M. E. Positron Emission Tomography. *Medical Instrumentation* **1979**, *13*, 147-151.

(52)   Robinson, R. O.; Ferrie, C. D.; Capra, M.; Maisey, M. N. Positron emission tomography and the central nervous system. *Archives of Disease in Childhood* **1999**, *81*, 263-270.

(53)   Gambhir, S. S. Molecular imaging of cancer with positron emission tomography. *Nature Reviews Cancer* **2002**, *2*, 683-693.

(54)   Mandl, S.; Schimmelpfennig, C.; Edinger, M.; Negrin, R. S.; Contag, C. H. Understanding immune cell trafficking patterns via in vivo bioluminescence imaging. *Journal of Cellular Biochemistry* **2002**, 239-248.

(55)   Jaffer, F. A.; Weissleder, R. Molecular imaging in the clinical arena. *Jama-Journal of the American Medical Association* **2005**, *293*, 855-862.

(56)   Danthi, S. N.; Pandit, S. D.; Li, K. C. P. A primer on molecular biology for imagers: VII. Molecular imaging probes. *Academic Radiology* **2004**, *11*, 1047-1054.

(57)   Cherry, S. R.; Gambhir, S. S. Use of positron emission tomography in animal research. *ILAR journal* **2001**, *42*, 219-232.

(58)   Krenning, E. P.; Kwekkeboom, D. J.; Bakker, W. H.; Breeman, W. A. P.; Kooij, P. P. M. et al. Somatostatin Receptor Scintigraphy with [in-111-Dtpa-D-Phe(1)]- and [I-123-Tyr(3)]-Octreotide - the Rotterdam Experience with More Than 1000 Patients. *European Journal of Nuclear Medicine* **1993**, *20*, 716-731.

(59)   Vallabhajosula, S.; Moyer, B. R.; ListerJames, J.; McBride, B. J.; Lipszyc, H. et al. Preclinical evaluation of technetium-99m-labeled somatostatin receptor-binding peptides. *Journal of Nuclear Medicine* **1996**, *37*, 1016-1022.

(60)   Breeman, W. A. P.; de Jong, M.; Kwekkeboom, D. J.; Valkema, R.; Bakker, W. H. et al. Somatostatin receptor-mediated imaging and therapy: basic science, current knowledge, limitations and future perspectives. *European Journal of Nuclear Medicine* **2001**, *28*, 1421-1429.

(61)   Tazebay, U. H.; Wapnir, I. L.; Levy, O.; Dohan, O.; Zuckier, L. S. et al. The mammary gland iodide transporter is expressed during lactation and in breast cancer. *Nature Medicine* **2000**, *6*, 871-878.

(62)   Piwnicaworms, D.; Rao, V. V.; Kronauge, J. F.; Croop, J. M. Characterization of Multidrug-Resistance P-Glycoprotein Transport Function with an Organotechnetium Cation. *Biochemistry* **1995**, *34*, 12210-12220.

(63)   Piwnicaworms, D.; Chiu, M. L.; Budding, M.; Kronauge, J. F.; Kramer, R. A. et al. Functional Imaging of Multidrug-Resistant P-Glycoprotein with an Organotechnetium Complex. *Cancer Research* **1993**, *53*, 977-984.

(64)   Cordobes, M. D.; Starzec, A.; DelmonMoingeon, L.; Blanchot, C.; Kouyoumdjian, J. C. et al. Technetium-99m-sestamibi uptake by human benign and malignant breast tumor cells: Correlation with mdr gene expression. *Journal of Nuclear Medicine* **1996**, *37*, 286-289.

(65)   Polyakov, V.; Sharma, V.; Dahlheimer, J. L.; Pica, C. M.; Luker, G. D. et al. Novel Tat-peptide chelates for direct transduction of technetium-99m and rhenium into human cells for imaging and radiotherapy. *Bioconjugate Chemistry* **2000**, *11*, 762-771.

(66)   Luker, G. D.; Piwnica-Worms, D. Molecular imaging - Beyond the genome: Molecular imaging in vivo with PET and SPECT. *Academic Radiology* **2001**, *8*, 4-14.

(67)   Jager, P. L.; Vaalburg, W.; Pruim, J.; de Vries, E. G. E.; Langen, K. J. et al. Radiolabeled amino acids: Basic aspects and clinical applications in oncology. *Journal of Nuclear Medicine* **2001**, *42*, 432-445.

(68)   Shields, A. F.; Grierson, J. R.; Dohmen, B. M.; Machulla, H. J.; Stayanoff, J. C. et al. Imaging proliferation in vivo with [F-18]FLT and positron emission tomography. *Nature Medicine* **1998**, *4*, 1334-1336.

(69)   Shields, A. F.; Dohmen, B. M.; Grierson, J. R.; Kuntzsch, M.; Machulla, H. J. et al. Imaging with [F-18]FLT and FDG in patients with cancer. *Journal of Nuclear Medicine* **1999**, *40*, 61p-61p.

(70)   Koh, W. J.; Bergman, K. S.; Rasey, J. S.; Peterson, L. M.; Evans, M. L. et al. Evaluation of Oxygenation Status During Fractionated Radiotherapy in Human Nonsmall Cell Lung Cancers Using [F-18] Fluoromisonidazole Positron Emission Tomography. *International Journal of Radiation Oncology Biology Physics* **1995**, *33*, 391-398.

(71)   Zhang, M. R.; Maeda, J.; Furutsuka, K.; Yoshida, Y.; Ogawa, M. et al. [F-18]FMDAA1106 and [F-18]FEDAA1106: Two positron-emitter labeled ligands for peripheral benzodiazepine receptor (PBR). *Bioorganic & Medicinal Chemistry Letters* **2003**, *13*, 201-204.

(72)   Iyer, M.; Barrio, J. R.; Namavari, M.; Bauer, E.; Satyamurthy, N. et al. 8-[F-18]fluoropenciclovir: An improved reporter probe for imaging HSV1-tk reporter

gene expression in vivo using PET. *Journal of Nuclear Medicine* **2001**, *42*, 96-105.

(73)   Dzik-Jurasz, A. S. K. Molecular imaging in vivo: an introduction. *The British Journal of Radiology* **2003**, *76*, S98-S109.

(74)   Shah, K.; Weissleder, R. Molecular optical imaging: applications leading to the development of present day therapeutics. *The American Society for Experimental NeuroTherapeutics* **2005**, *2*, 215-225.

(75)   Weissleder, R. A clearer vision for in vivo imaging. *Nature Biotechnology* **2001**, *19*, 316-317.

(76)   Ntziachristos, V.; Ripoll, J.; Weissleder, R. Would near-infrared fluorescence signals propagate through large human organs for clinical studies? (vol 27, pg 333, 2002). *Optics Letters* **2002**, *27*, 1652-1652.

(77)   Weissleder, R.; Ntziachristos, V. Shedding light onto live molecular targets. *Nature Medicine* **2003**, *9*, 123-128.

(78)   Bornhop, D. J.; Contag, C. H.; Licha, K.; Murphy, C. J. Advances in contrast agents, reporters, and detection. *Journal of Biomedical Optics* **2001**, *6*, 106-110.

(79)   Banerjee, B.; Miedema, B.; Chandrasekhar, H. R. Emission spectra of colonic tissue and endogenous fluorophores. *American Journal of the Medical Sciences* **1998**, *316*, 220-226.

(80)   Romer, T. J.; Fitzmaurice, M.; Cothren, R. M.; Richardskortum, R.; Petras, R. et al. Laser-Induced Fluorescence Microscopy of Normal Colon and Dysplasia in Colonic Adenomas - Implications for Spectroscopic Diagnosis. *American Journal of Gastroenterology* **1995**, *90*, 81-87.

(81)   Wagnieres, G. A.; Star, W. M.; Wilson, B. C. In vivo fluorescence spectroscopy and imaging for oncological applications. *Photochemistry and Photobiology* **1998**, *68*, 603-632.

(82)   Mahmood, U.; Weissleder, R. Near-infrared optical imaging of proteases in cancer. *Molecular Cancer Therapeutics* **2003**, *2*, 489-496.

(83)   Bremer, C.; Ntziachristos, V.; Weissleder, R. Optical-based molecular imaging: contrast agents and potential medical applications. *European Radiology* **2003**, *13*, 231-243.

(84)   Frangioni, J. V. In vivo near-infrared fluorescence imaging. *Current Opinion in Chemical Biology* **2003**, *7*, 626-634.

(85)   Leevy, C. M.; Smith, F.; Longuevi.J; Paumgart.G; Howard, M. M. Indocyanine Green Clearance as a Test for Hepatic Function. *Journal of the American Medical Association* **1967**, *200*, 236-&.

(86)   Schad, H.; Brechtelsbauer, H.; Kramer, K. Studies on Suitability of a Cyanine Dye (Viher-Test) for Indicator Dilution Technique and Its Application to Measurement of Pulmonary-Artery and Aortic Flow. *Pflugers Archiv-European Journal of Physiology* **1977**, *370*, 139-144.

(87)   Flower, R. W.; Hochheimer, B. F. Indocyanine Green Dye Fluorescence and Infrared-Absorption Choroidal Angiography Performed Simultaneously with Fluorescein Angiography. *Johns Hopkins Medical Journal* **1976**, *138*, 33-42.

(88)   Reynolds, J. S.; Troy, T. L.; Mayer, R. H.; Thompson, A. B.; Waters, D. J. et al. Imaging of spontaneous canine mammary tumors using fluorescent contrast agents. *Photochemistry and Photobiology* **1999**, *70*, 87-94.

(89)   Licha, K.; Riefke, B.; Ntziachristos, V.; Becker, A.; Chance, B. et al. Hydrophilic cyanine dyes as contrast agents for near-infrared tumor imaging: Synthesis, photophysical properties and spectroscopic in vivo characterization. *Photochemistry and Photobiology* **2000**, *72*, 392-398.

(90)   Gurfinkel, M.; Thompson, A. B.; Ralston, W.; Troy, T. L.; Moore, A. L. et al. Pharmacokinetics of ICG and HPPH-car for the detection of normal and tumor tissue using fluorescence, near-infrared reflectance imaging: A case study. *Photochemistry and Photobiology* **2000**, *72*, 94-102.

(91)   Neri, D.; Carnemolla, B.; Nissim, A.; Leprini, A.; Querze, G. et al. Targeting by affinity-matured recombinant antibody fragments of an angiogenesis associated fibronectin isoform. *Nature Biotechnology* **1997**, *15*, 1271-1275.

(92)   Tung, C. H.; Lin, Y. H.; Moon, W. K.; Weissleder, R. A receptor-targeted near-infrared fluorescence probe for in vivo tumor imaging. *Chembiochem* **2002**, *3*, 784-786.

(93)   Achilefu, S.; Dorshow, R. B.; Bugaj, J. E.; Rajagopalan, R. Novel receptor-targeted fluorescent contrast agents for in vivo tumor imaging. *Investigative Radiology* **2000**, *35*, 479-485.

(94)   Licha, K.; Hessenius, C.; Becker, A.; Henklein, P.; Bauer, M. et al. Synthesis, characterization, and biological properties of cyanine-labeled somatostatin analogues as receptor-targeted fluorescent probes. *Bioconjugate Chemistry* **2001**, *12*, 44-50.

(95)   Becker, A.; Hessenius, C.; Licha, K.; Ebert, B.; Sukowski, U. et al. Receptor-targeted optical imaging of tumors with near-infrared fluorescent ligands. *Nature Biotechnology* **2001**, *19*, 327-331.

(96)   Ke, S.; Wen, X. X.; Gurfinkel, M.; Charnsangavej, C.; Wallace, S. et al. Near-infrared optical imaging of epidermal growth factor receptor in breast cancer xenografts. *Cancer Research* **2003**, *63*, 7870-7875.

(97)   Kovar, J. L.; Volcheck, W. M.; Chen, J. Y.; Simpson, M. A. Purification method directly influences effectiveness of an epidermal growth factor-coupled targeting agent for noninvasive tumor detection in mice. *Analytical Biochemistry* **2007**, *361*, 47-54.

(98)   Kovar, J. L.; Johnson, M. A.; Volcheck, W. M.; Chen, J. Y.; Simpson, M. A. Hyaluronidase expression induces prostate tumor metastasis in an orthotopic mouse model. *American Journal of Pathology* **2006**, *169*, 1415-1426.

(99)   Backer, M. V.; Patel, V.; Jehning, B. T.; Backer, J. M. Self-assembled "dock and lock" system for linking payloads to targeting proteins. *Bioconjugate Chemistry* **2006**, *17*, 912-919.

(100)   Petrovsky, A.; Schellenberger, E.; Josephson, L.; Weissleder, R.; Bogdanov, A. Near-infrared fluorescent imaging of tumor apoptosis. *Cancer Research* **2003**, *63*, 1936-1942.

(101)   Ntziachristos, V.; Schellenberger, E. A.; Ripoll, J.; Yessayan, D.; Graves, E. et al. Visualization of antitumor treatment by means of fluorescence molecular tomography with an annexin V-Cy5.5 conjugate. *Proceedings of the National Academy of Sciences of the United States of America* **2004**, *101*, 12294-12299.

(102)   Choi, H. K.; Yessayan, D.; Choi, H. J.; Schellenberger, E.; Bogdanov, A. et al. Quantitative analysis of chemotherapeutic effects in tumors using in vivo staining and correlative histology. *Cellular Oncology* **2005**, *27*, 183-190.

(103)   Zhang, M.; Zhang, Z. H.; Blessington, D.; Li, H.; Busch, T. M. et al. Pyropheophorbide 2-deoxyglucosamide: A new photosensitizer targeting glucose transporters. *Bioconjugate Chemistry* **2003**, *14*, 709-714.

(104)   Cheng, Z.; Levi, J.; Xiong, Z. M.; Gheysens, O.; Keren, S. et al. Near-infrared fluorescent deoxyglucose analogue for tumor optical imaging in cell culture and living mice. *Bioconjugate Chemistry* **2006**, *17*, 662-669.

(105)   Ye, Y. P.; Bloch, S.; Kao, J.; Achilefu, S. Multivalent carbocyanine molecular probes: Synthesis and applications. *Bioconjugate Chemistry* **2005**, *16*, 51-61.

(106)   Tung, C. H.; Bredow, S.; Mahmood, U.; Weissleder, R. Preparation of a cathepsin D sensitive near-infrared fluorescence probe for imaging. *Bioconjugate Chemistry* **1999**, *10*, 892-896.

(107)   Law, B.; Curino, A.; Bugge, T. H.; Weissleder, R.; Tung, C. H. Design, synthesis, and characterization of urokinase plasminogen-activator-sensitive near-infrared reporter. *Chemistry & Biology* **2004**, *11*, 99-106.

(108) Adam, W.; Reinhardt, D.; SahaMoller, C. R. From the firefly bioluminescence to the dioxetane-based (AMPPD) chemiluminescence immunoassay: A retroanalysis. *Analyst* **1996**, *121*, 1527-1531.

(109) Contag, C. H.; Spilman, S. D.; Contag, P. R.; Oshiro, M.; Eames, B. et al. Visualizing gene expression in living mammals using a bioluminescent reporter. *Photochemistry and Photobiology* **1997**, *66*, 523-531.

(110) Contag, P. R.; Olomu, I. N.; Stevenson, D. K.; Contag, C. H. Bioluminescent indicators in living mammals. *Nature Medicine* **1998**, *4*, 245-247.

(111) Contag, C. H.; Jenkins, D.; Contag, F. R.; Negrin, R. S. Use of reporter genes for optical measurements of neoplastic disease in vivo. *Neoplasia* **2000**, *2*, 41-52.

(112) Valley, M. P.; Zhou, W.; Hawkins, E. M.; Shultz, J.; Cali, J. J. et al. A bioluminescent assay for monoamine oxidase activity. *Analytical Biochemistry* **2006**, *359*, 238-246.

(113) Zhou, W. H.; Valley, M. P.; Shultz, J.; Hawkins, E. M.; Bernad, L. et al. New bioluminogenic substrates for monoamine oxidase assays. *Journal of the American Chemical Society* **2006**, *128*, 3122-3123.

(114) Zhou, W. H.; Shultz, J. W.; Murphy, N.; Hawkins, E. M.; Bernad, L. et al. Electrophilic aromatic substituted luciferins as bioluminescent probes for glutathione S-transferase assays. *Chemical Communications* **2006**, 4620-4622.

(115) O'Brien, M. A.; Daily, W. J.; Hesselberth, P. E.; Moravec, R. A.; Scurria, M. A. et al. Homogeneous, bioluminescent protease assays: Caspase-3 as a model. *Journal of Biomolecular Screening* **2005**, *10*, 137-148.

(116) Chan, W. C. W.; Maxwell, D. J.; Gao, X. H.; Bailey, R. E.; Han, M. Y. et al. Luminescent quantum dots for multiplexed biological detection and imaging. *Current Opinion in Biotechnology* **2002**, *13*, 40-46.

(117) Gao, X. H.; Yang, L. L.; Petros, J. A.; Marshal, F. F.; Simons, J. W. et al. In vivo molecular and cellular imaging with quantum dots. *Current Opinion in Biotechnology* **2005**, *16*, 63-72.

(118) Qu, L. H.; Peng, X. G. Control of photoluminescence properties of CdSe nanocrystals in growth. *Journal of the American Chemical Society* **2002**, *124*, 2049-2055.

(119) Han, M. Y.; Gao, X. H.; Su, J. Z.; Nie, S. Quantum-dot-tagged microbeads for multiplexed optical coding of biomolecules. *Nature Biotechnology* **2001**, *19*, 631-635.

(120) Kaji, N.; Tokeshi, M.; Baba, Y. Quantum dots for single bio-molecule imaging. *Analytical Sciences* **2007**, *23*, 21-24.

(121) Yu, W. W.; Chang, E.; Drezek, R.; Colvin, V. L. Water-soluble quantum dots for biomedical applications. *Biochemical and Biophysical Research Communications* **2006**, *348*, 781-786.

(122) Sapsford, K. E.; Pons, T.; Medintz, I. L.; Mattoussi, H. Biosensing with luminescent semiconductor quantum dots. *Sensors* **2006**, *6*, 925-953.

(123) Kumar, S.; Richards-Kortum, R. Optical molecular imaging agents for cancer diagnostics and therapeutics. *Nanomedicine* **2006**, *1*, 23-30.

(124) Michalet, X.; Pinaud, F. F.; Bentolila, L. A.; Tsay, J. M.; Doose, S. et al. Quantum dots for live cells, in vivo imaging, and diagnostics. *Science* **2005**, *307*, 538-544.

(125) Gao, X. H.; Cui, Y. Y.; Levenson, R. M.; Chung, L. W. K.; Nie, S. M. In vivo cancer targeting and imaging with semiconductor quantum dots. *Nature Biotechnology* **2004**, *22*, 969-976.

(126) Chan, W. C. W.; Nie, S. M. Quantum dot bioconjugates for ultrasensitive nonisotopic detection. *Science* **1998**, *281*, 2016-2018.

(127) Wu, X. Y.; Liu, H. J.; Liu, J. Q.; Haley, K. N.; Treadway, J. A. et al. Immunofluorescent labeling of cancer marker Her2 and other cellular targets with semiconductor quantum dots (vol 21, pg 41, 2003). *Nature Biotechnology* **2003**, *21*, 452-452.

(128) Mitchell, G. P.; Mirkin, C. A.; Letsinger, R. L. Programmed assembly of DNA functionalized quantum dots. *Journal of the American Chemical Society* **1999**, *121*, 8122-8123.

(129) Lidke, D. S.; Nagy, P.; Heintzmann, R.; Arndt-Jovin, D. J.; Post, J. N. et al. Quantum dot ligands provide new insights into erbB/HER receptor-mediated signal transduction. *Nature Biotechnology* **2004**, *22*, 198-203.

(130) Dahan, M.; Levi, S.; Luccardini, C.; Rostaing, P.; Riveau, B. et al. Diffusion dynamics of glycine receptors revealed by single-quantum dot tracking. *Science* **2003**, *302*, 442-445.

(131) Kim, S.; Lim, Y. T.; Soltesz, E. G.; De Grand, A. M.; Lee, J. et al. Near-infrared fluorescent type II quantum dots for sentinel lymph node mapping. *Nature Biotechnology* **2004**, *22*, 93-97.

(132) Ballou, B.; Lagerholm, B. C.; Ernst, L. A.; Bruchez, M. P.; Waggoner, A. S. Noninvasive imaging of quantum dots in mice. *Bioconjugate Chemistry* **2004**, *15*, 79-86.

(133) Jaiswal, J. K.; Mattoussi, H.; Mauro, J. M.; Simon, S. M. Long-term multiple color imaging of live cells using quantum dot bioconjugates. *Nature Biotechnology* **2003**, *21*, 47-51.

(134) Jensen, J. A. Medical ultrasound imaging. *Progress in Biophysics & Molecular Biology* **2007**, *93*, 153-165.

(135) Kaufmann, B. A.; Lindner, J. R. Molecular imaging with targeted contrast ultrasound. *Current Opinion in Biotechnology* **2007**, *18*, 11-16.

(136) Christiansen, J. P.; Leong-Poi, H.; Fisher, N. G.; Klibanov, A. L.; Kaul, S. et al. Non-invasive imaging of myocardial inflammation following reperfusion injury using leukocyte-targeted contrast echocardiography. *Circulation* **2001**, *104*, 589-589.

(137) Lindner, J. R.; Song, J.; Xu, F.; Klibanov, A. L.; Singbartl, K. et al. Noninvasive ultrasound imaging of inflammation using microbubbles targeted to activated leukocytes. *Circulation* **2000**, *102*, 2745-2750.

(138) Lindner, J. R.; Dayton, P. A.; Coggins, M. P.; Ley, K.; Song, J. et al. Noninvasive imaging of inflammation by ultrasound detection of phagocytosed microbubbles. *Circulation* **2000**, *102*, 531-538.

(139) Lanza, G. M.; Wickline, S. A. Targeted ultrasonic contrast agents for molecular imaging and therapy. *Current Problems in Cardiology* **2003**, *28*, 625-653.

(140) Leong-Poi, H.; Christiansen, J.; Klibanov, A. L.; Kaul, S.; Lindner, J. R. Noninvasive assessment of angiogenesis by ultrasound and microbubbles targeted to alpha(v)-integrins. *Circulation* **2003**, *107*, 455-460.

(141) Schumann, P. A.; Christiansen, J. P.; Quigley, R. M.; McCreery, T. P.; Sweitzer, R. H. et al. Targeted-microbubble binding selectively to GPIIb IIIa receptors of platelet thrombi. *Investigative Radiology* **2002**, *37*, 587-593.

(142) McCullough, E. C.; Payne, J. T. X-ray-transmission computed tomography. *Medical physics* **1977**, *4*, 85-98.

(143) Paulus, M. J.; Gleason, S. S.; Kennel, S. J.; Hunsicker, P. R.; Johnson, D. K. High resolution X-ray computed tomography: An emerging tool for small animal cancer research. *Neoplasia* **2000**, *2*, 62-70.

(144) Paulus, M. J.; Gleason, S. S.; Easterly, M. E.; Foltz, C. J. A review of high resolution X-ray computed tomography and other imaging modalities for small animal research. *Lab Animal* **2001**, *30*, 36-45.

(145) Berger, F.; Lee, Y. P.; Loening, A. M.; Chatziioannou, A.; Freedland, S. J. et al. Whole-body skeletal imaging in mice utilizing microPET: optimization of

reproducibility and applications in animal models of bone disease. *European Journal of Nuclear Medicine and Molecular Imaging* **2002**, *29*, 1225-1236.

(146) Beyer, T.; Townsend, D. W.; Blodgett, T. M. Dual-modality PET/CT tomography for clinical oncology. *Quarterly Journal of Nuclear Medicine* **2002**, *46*, 24-34.

(147) Huber, M. M.; Staubli, A. B.; Kustedjo, K.; Gray, M. H. B.; Shih, J. et al. Fluorescently detectable magnetic resonance imaging agents. *Bioconjugate Chemistry* **1998**, *9*, 242-249.

(148) Josephson, L.; Kircher, M. F.; Mahmood, U.; Tang, Y.; Weissleder, R. Near-infrared fluorescent nanoparticles as combined MR/optical imaging probes. *Bioconjugate Chemistry* **2002**, *13*, 554-560.

(149) Kircher, M. F.; Mahmood, U.; King, R. S.; Weissleder, R.; Josephson, L. A multimodal nanoparticle for preoperative magnetic resonance imaging and intraoperative optical brain tumor delineation. *Cancer Research* **2003**, *63*, 8122-8125.

(150) Zhang, Z. R.; Liang, K. X.; Bloch, S.; Berezin, M.; Achilefu, S. Monomolecular multimodal fluorescence-radioisotope imaging agents. *Bioconjugate Chemistry* **2005**, *16*, 1232-1239.

(151) Zheng, J. Z.; Perkins, G.; Kirilova, A.; Allen, C.; Jaffray, D. A. Multimodal contrast agent for combined computed tomography and magnetic resonance imaging applications. *Investigative Radiology* **2006**, *41*, 339-348.

(152) Manning, H. C.; Goebel, T.; Marx, J. N.; Bornhop, D. J. Facile, efficient conjugation of a trifunctional lanthanide chelate to a peripheral benzodiazepine receptor ligand. *Organic Letters* **2002**, *4*, 1075-1078.

(153) Manning, H. C.; Goebel, T.; Thompson, R. C.; Price, R. R.; Lee, H. et al. Targeted molecular imaging agents for cellular-scale bimodal imaging. *Bioconjugate Chemistry* **2004**, *15*, 1488-1495.

(154) Griffin, J. M. M.; Skwierawska, A. M.; Manning, H. C.; Marx, J. N.; Bornhop, D. J. Simple, high yielding synthesis of trifunctional fluorescent lanthanide chelates. *Tetrahedron Letters* **2001**, *42*, 3823-3825.

CHAPTER II

IN VITRO AND IN VIVO EVALUATION OF A POTENTIAL OPTICAL
ANALOGUE TO [^{18}F]FLUORO-2-DEOXY-D-GLUCOSE (^{18}FDG)

2.1 Introduction

One of the most successful molecular imaging agents is [^{18}F]-fluoro-2-deoxy-D-

glucose (^{18}FDG), which has been employed as a positron emission tomography (PET)

agent to image living subjects non-invasively for three decades. ^{18}FDG-PET imaging is

widely used in studying normal and pathologic functions, especially tumors of brain,

heart, breast, head, neck, ovary, and other tissues[1-5].

^{18}FDG is a glucose analogue (Figure 2.1). Under steady state conditions, ^{18}FDG is

taken up by cells via glucose transporters (GLUT) in competition with glucose[6]. Once

inside cells, ^{18}FDG and glucose are phosphorylated to ^{18}FDG-6-phosphate and glucose-6-

phosphate respectively by hexokinase[7]. Both ^{18}FDG-6-phosphate and glucose-6-

phosphate can be dephosphorylated to ^{18}FDG and glucose by glucose-6-phosphatase,

however the dephosphorylation occurs rather slowly due to the low concentration of the enzyme in most cells[6]. Unlike glucose-6-phosphate, which can be

Figure 2.1. Structures of ^{18}FDG and glucose
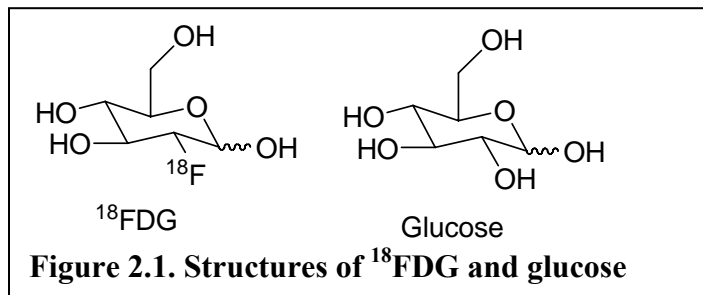
metabolized further eventually to water and carbon dioxide, ^{18}FDG-6-phosphate can not

act as a substrate for further glycolysis[8]. Therefore, ^{18}FDG-6-phosphate accumulates in

cells. Due to these facts, ^{18}FDG can be used to depict spatial distribution of increased

glucose metabolism, which is related to many diseases[7]. For example, most tumors overexpress GLUTs and have high levels of glycolysis. As a result, [18]FDG has become an efficient contrast agent for cancer imaging.

While [18]FDG-PET imaging is highly sensitive and clinically useful, the requirement of a cyclotron to generate radioisotopes, the short half life time of [18]F (110 minutes), exposure to ionizing radiation, and low special resolution remain as limitations. To overcome some of these limitations, several [18]FDG analogs for optical imaging have been developed, including 2-[N-(7-nitrobenz-2-oxa-1,3-diazol-4-yl)amino]-2-deoxy-D-glucose (2-NBDG)[9-13], pyropheophorbide 2-deoxyglucosamide (Pyro-2DG)[6], multivalent carboncyanine-glucosamine[14], and Cy5.5-D-glucosamine (Cy5.5-2DG)[15].

Matsuoka and colleagues developed the first optical [18]FDG analogue, 2-NBDG, in 1996. It was demonstrated that cellular uptake of 2-NBDG was inhibited by D-glucose but not L-glucose[9]. In addition, intracellular phosphorylation of 2-NBDG to 2-NBDG-6-phosphate was verified by mass spectrometry[10]. These results suggest that 2-NBDG is taken up and accumulated via the GLUT/hexokinase pathway. However, the spectroscopic properties (λ_{ex} = 475 nm and λ_{em} = 550 nm) render the 2-NBDG probe a poor choice for in vivo imaging due to high hemoglobin absorption and strong tissue scattering.

Recently, several studies have attempted to develop [18]FDG analogues suitable for in vivo imaging by coupling glucosamine to NIR dyes. Pyro-2DG (λ_{ex} = 665 nm and λ_{em} = 720 nm), which functions as both a NIR imaging and photodynamic therapy agent, demonstrated enhanced tumor uptake relative to the surrounding muscle tissue and selective mitochondrial damage to tumor region[6]. Preliminary confocal microscopy

studies suggest that the uptake of Pyro-2DG is GLUT-specific, since D-glucose appears to competitively inhibit cellular localization of Pyro-2DG but not Pyro-acid[6]. Using an alternative approach, Achilefu and coworkers synthesized multivalent carboncyanine-glucosamine complex (λ_{ex} = ~780 nm and λ_{em} = ~810 nm) based on an inner NIR carbocyanine core[14]. Although the number of glucosamine (1, 2, 3, 4, 6, or 8) conjugated to the carbocyanine core does not appear to correlate with tumor uptake, each of the dendritic glucosamine arrays provided some tumor signal. However, the mechanisms of uptake and accumulation of the multivalent carbocyanine-glucosamine complex remain unknown. Interestingly, Gambhir and colleagues reported that another [18]FDG analogue, Cy5.5-2DG (λ_{ex} = 675 nm and λ_{em} =695 nm), does not appear to follow the GLUT/hexokinase pathway and provides significantly less contrast enhancement than the free Cy5.5 dye[15]. The authors hypothesize that the dye characteristics are responsible for the differing behaviors of 2-NBDG and Cy5.5-2DG and suggest careful selection of NIR fluorophores for particular biological applications.

In an effort to develop an improved optical analogue to [18]FDG, we have developed an alternative NIR [18]FDG analogue by conjugating D-glucosamine to IRDye[TM] 800CW NHS ester (mentioned in 1.5.2.1). Compared to pyropheophorbide (no sulfonate or carboxylate group after conjugation) and carbocyanine(0-1 carboxylate group after conjugation), IRDye[TM] 800CW NHS ester (four sulfonate groups) has increased water solubility. In addition, IRDye[TM] 800CW NHS ester (λ_{ex} = 778 nm and λ_{em} =794 nm), capitalizes on the increased photon penetration in the NIR tissue transparency window and is red-shifted relative to either Cy5.5 or pyropheophorbide. This red-shift in excitation and emission eliminates the fluorescence contribution from

the autofluorescence of typical alfalfa-based rodent chow, which is often seen in the Cy5.5 wavelength region, and is more suitable for in vivo imaging[16].

Here, we report the synthesis, and in vitro/in vivo characterization of IRDye[TM] 800CW–glucosamine (NIR-glucosamine). An SW480*neo* mouse model of human colon cancer was used for imaging studies and the results corroborate and expand upon the recent discoveries reported for Cy5.5-2DG[15].

2.2 Materials and Methods

2.2.1 Materials

The IRDye[TM] 800CW NHS Ester dye and IRDye[TM] 800-acid (designated here as "free NIR dye") were obtained from LI-COR Biosciences (Lincoln, NE). Sodium methoxide, glucosamine hydrochloride, D-(+)-glucose monohydrate, and cytochalasin B were purchased from Fluka/Sigma Aldrich (St. Louis, MO). Dimethylsulfoxide (DMSO) was purchased from Fisher Scientific (Pittsburgh, PA). SW480 (human colorectal adenocarcinoma) cells were acquired from the American Type Culture Collection (ATCC; Manassas, VA). Calcium- and magnesium-free phosphate buffered saline (CMF-PBS), Dulbecco's Modified Eagle Medium (DMEM), fetal bovine serum (FBS), and gentamicin sulfate were obtained from Invitrogen Corporation (Carlsbad, CA). Female athymic nude mice (6 weeks of age) were obtained from Harlan Sprague Dawley (Indianapolis, IN).

2.2.2 NIR-glucosamine Synthesis

A mixture of sodium methoxide (9.3 mg, 0.17 mmol) and D-glucosamine hydrochloride (37 mg, 0.17 mmol) in DMSO (2 mL) was stirred under room temperature

for 2 h. A portion (150 μL) of the solution (12.9 μmol) was added to a stirring solution of IRDye[TM] 800CW (5 mg, 4.3 μmol) in DMSO (9.85 mL) solution. The mixture was stirred in dark under argon positive pressure flow overnight.

High performance liquid chromatography (HPLC) analysis was performed to monitor the reaction on a Varian Polaris C-18 column (250 × 4.6 mm) at a flow rate of 0.8 mL/min. Flow A was 0.1% triethylamine (TEA) in water and flow B was 0.1% TEA in acetonitrile. The elution method for analytical HPLC started with a linear gradient from 100% to 80% A over 30 min, then from 80% to 50% A for 5 min, arrived at 20% A in another 3 min, held at 20% A for 10 min, and finally returned to 100% A over 1 min. The elution profile was monitored by ultraviolet (UV) absorbance at 254 and 780 nm. Product was purified by preparative HPLC using a Varian Polaris C-18 column (250 × 21.2 mm) at 17 mL/min. The collected solution was concentrated by vacuum rotary evaporation, frozen to -78ºC and dried under freeze-dry system. The amount of NIR-glucosamine was determined by absorption in DMSO solution at 780 nm (3.5 mg, 66%). ^{1}H NMR 400 MHz (MeOD) δ 8.02-7.93 (m, 2H), 7.88-7.80 (m, 6H), 7.36 (d, J=8.4 Hz, 1H), 7.28 (d, J=8.4 Hz, 1H), 7.19 (d, J=8.8 Hz, 2H), 6.29 (d, J=14.4 Hz, 1H), 6.19 (d, J=14.0 Hz, 1H), 5.08 (d, J=3.2 Hz, 1H), 4.20-4.14 (m, 2H), 4.10 (t, J=6.8 Hz, 2H), 3.89-3.58 (m, 5H), 3.06-3.01 (m, 2H), 2.92-2.86 (m, 2H), 2.82-2.75 (m, 2H), 2.28-2.22 (m, 2H), 2.08-2.05 (m, 2H), 2.00-1.91 (m, 5H), 1.80-1.79 (m, 2H), 1.71-1.68 (m, 3H), 1.40 (s, 12H). MS (ESI)$^+$ [M+H]$^+$ calcd 1162.3, found 1162.2.

2.2.3 Spectroscopic Characterization

The absorbance spectra of free NIR dye and NIR-glucosamine were measured using a Shimadzu UV-VIS 1700 spectrophotometer (Columbia, MD) and the emission

spectra were measured using a PTI Technologies spectrofluorometer (Oxnard, CA).

2.2.4 NIR-glucosamine Stability Study

To determine the stability of NIR-glucosamine, the sample was dissolved in DMSO, pH 5.0 buffer, pH 6.0 buffer, Phosphate Buffered Saline (PBS) buffer (pH 7.3), pH 8.2 buffer, pH 9.0 buffer, and DI water (pH 6.0) independently. The methods for preparation of buffer solutions are listed in Table 2.1. All samples were excited at their maximum absorption wavelength when fluorescence spectra were taken. The fluorometer settings were: 1 nm/second scan rate, 1.5 nm slit width and 75 watts Photomultiplier tube (PMT) voltage.

Table 2.1. Buffer solutions preparation method

Buffer solutions	Preparation methods
pH 5.0	0.1 M potassium hydrogen phthalate (KHP) solution was mixed with 0.1 M sodium hydroxide solution
pH 6.0	Added 0.1 M hydrochloric acid solution to 0.1 M potassium phosphate solution
PBS buffer	Dissolved one PBS tablet in 100 mL water
pH 8.2	0.1 M sodium bicarbonate solution
PH 9.0	0.1 M sodium bicarbonate solution was mixed with 0.1 M sodium carbonate

2.2.5 Cell Culture

Stable SW480 clones expressing the neomycin selection cassette (SW480*neo*) were isolated and characterized as previously reported[17]. SW480*neo* (human colorectal adenocarcinoma) cells were propagated in Dulbecco's Modified Eagle Medium (DMEM; high glucose) supplemented with 2 mM L-glutamine, 10% FBS, and 50 mg gentamicin sulfate in vented culture flasks (Corning; Corning, NY) at 37 °C and 5% CO_2. The

medium was replaced every three days or as necessary. After attaining confluence, the cells were sub-cultured approximately 1:2 to 1:10.

2.2.6 Animal Models

Animal studies were performed under guidelines approved by the Institutional Animal Care and Use Committee (IACUC) at Vanderbilt University.

SW480*neo* cells were propagated until near confluency as described above. Cells were harvested by incubation with trypsin, pelleted by centrifugation, resuspended in sterile CMF-PBS, counted and assessed for viability (%) using trypan blue staining. The cells were again pelleted by centrifugation, resuspended in sterile CMF-PBS at a concentration of 1.5×10^6 or 2×10^6 cells/100 μL and kept on ice. Prior to cell implantation, the cell-containing tube was gently inverted several times to assure proper cell distribution. Athymic nude (nu/nu) mice were finally injected with approximately 1.5×10^6 or 2×10^6 SW480*neo* cells (100 μL volume) subcutaneously on one or both hind limbs.

2.2.7 In Vivo Optical Imaging Studies

During the imaging sessions, the mice were kept on a heated animal support plate under general anesthesia by inhalation of 2-3% isoflurane. Anesthesia was initiated in an induction chamber.

Tumor-bearing mice that had been fasted overnight to decrease blood glucose levels were retroorbitally injected with 20 nmoles of either free NIR dye or NIR-glucosamine (100 μL in sterile saline). The biodistribution and accumulation of free NIR dye and NIR-glucosamine were monitored in real-time using the IVIS Imaging System 200 (Xenogen Corporation/ Caliper LifeSciences; Alameda, CA) equipped with an

indocyanine green (ICG) excitation and emission filter set (710 – 760 nm and 810 – 875 nm, respectively). Images were obtained pre-injection and at numerous time points post-injection (typically several minutes post-injection, 1 hour, 3 hours, 4 hours, 6 hours, 8 hours, 12 hours, 24 hours, and 48 hours). The following instrument settings were used: 1 or 3 second exposure time, small or medium binning (4 × 4 pixels or 8 × 8 pixels, respectively), f/stop of 8, and FOV B or C (6.4 cm × 6.4 cm and 12.8 cm × 12.8 cm, respectively). At the conclusion of the study, the mice were sacrificed and the harvested organs (heart, lungs, kidneys, liver) and tumors were also imaged using the same IVIS instrument parameters and/or on the Odyssey Infrared Imaging System. The tumors and organs were subsequently fixed in 10% formalin followed by ethanol dehydration. The fixed tumor tissues were then paraffin embedded and serially sliced. Alternating slices were stained with hematoxylin and eosin (H&E) for histological characterization or DAPI-mounted for NIR fluorescence microscopy.

The data were processed in Living Image® Software Version 2.50 (Xenogen Corporation). Regions of interest (ROIs) were drawn over the xenograft tumors and a normal region. Since most of the mice had two hindlimb tumors, several "normal" ROIs were drawn and evaluated including: (A) regions over one forelimb; (B) along the midline (spine) between the two flank tumors; (C) slightly to the right or left of the spine between the two flank tumors; (D) between the forelimbs; and (E) below the tumors on the lower portion of a hindlimb. All of the data presented here refer to the lower hindlimb ROI analysis for reasons discussed below. Also, since these mice were imaged longitudinally, the contribution of residual NIR-glucosamine or free NIR dye was accounted for by subtracting the original (true) pre-injection fluorescence intensity

obtained on the first day of imaging from the initial "pre-injection" fluorescence intensity acquired a week or more later. This image also allows the baseline pre-injection values to be reestablished. For example:

$$FI_{6h\ pi,\ dayB}{}' = FI_{6h\ pi,\ dayB} - (FI_{preinjection,\ dayB} - FI_{preinjection,\ day\ A})$$

where $FI \equiv$ fluorescence intensity in terms of average radiance $= [p/s/cm^2/sr]$ and $(FI_{preinjection,\ dayB} - FI_{preinjection,\ day\ A})$ represents the contribution from the residual fluorescence signal.

To generate time activity curves and monitor biodistribution, accumulation and clearance rates, the average radiance (photons/sec/cm^2/sr) $\pm$ standard deviation for each group were plotted as a function of time post-injection to generate time-activity curves (n $= 2 - 8$ tumors from $1 - 4$ mice per group). To further determine tumor specificity, the tumor to normal contrast ratio was calculated as the average ratio of the fluorescence intensity of the tumor region relative to the normal tissue.

2.2.8 In Vivo MicroPET Imaging

SW480*neo* tumor-bearing mice that had been fasted overnight to decrease blood glucose levels were injected with approximately 118-300 µCi of ^{18}FDG two days pre- or post-injection of NIR-glucosamine and imaged dynamically for 1-1.5 hours using the Concorde Microsystems microPET Focus 220 (Concorde Microsystems; Knoxville, TN). Maximum a posteriori (MAP) reconstructions were performed after the scans were collected. Data processing was performed using ASIPro VM^{TM} (Concorde Microsystems; Knoxville, TN).

2.2.9 Blood Stability

HPLC was used to evaluate the stability of NIR-glucosamine in blood. Since

blood samples taken from mice ~3.5 hours post-injection of NIR-glucosamine did not

contain enough compound to analyze via HPLC or mass spectrometry, these studies were

performed *ex vivo*. To keep a similar NIR-glucosamine concentration as in animal

imaging studies (20 nmoles injected per mouse, estimated to have a blood volume of 1.6

mL), five nmoles of NIR-glucosamine was added to 400 μL of blood obtained from

Balb/c mice in the ex vivo experiment. The blood was originally collected and stored in

heparinized-tubes. The NIR-glucosamine-containing blood was then incubated at 37 °C

for either zero, four or eight hours to allow sufficient time for agent degradation by blood

components. The NIR-glucosamine-containing blood was then centrifuged at 1,800 g for

20 minutes to separate the red blood cells from the plasma. The supernatant (plasma) was

collected, vortexed, and centrifuged again for 20 minutes at 1,800 g to settle any

sediment. The supernatant was carefully transferred to another tube and an equal volume

of acetonitrile was added for precipitation. The tube was vortexed for 60 seconds and

centrifuged for five minutes at 1,800 g. Supernatant was transferred to a separate tube and

centrifuged again at 1,800 g for five minutes to remove any residual precipitate.

Stock NIR-glucosamine and free NIR dye as well as the purified plasma samples

were analyzed via HPLC at 782 nm. Flow A was 20 mM tetrabutylammonium bromide

in water and B was 20 mM tetrabutylammonium bromide in 90% acetonitrile and 10%

water. The elution method started with a linear gradient from 100% to 50% A over 10

minutes, held at 50% for 5 minutes, arrived at 10% A in another 10 minutes, held at 10%

A for 5 minutes and finally returned to 100% A over 1 minute. The data were processed

by integrating the area under the peaks at 782 nm using Empower software (Waters

Corporation; Milford, MA). The relative percent free NIR dye (eluting at 23 minutes)

and NIR-glucosamine (eluting at 18 minutes) were calculated as:

$$\% \text{ Free NIR Dye} = \frac{\text{Area at 23 minutes}}{\text{Area at 18 min} + \text{Area at 23 min}} \times 100$$

$$\% \text{ NIR - glucosamine} = \frac{\text{Area at 18 minutes}}{\text{Area at 18 min} + \text{Area at 23 min}} \times 100$$

2.2.10 Cell Imaging

SW480*neo* cells (~75,000 per dish) were plated in collagen-coated glass bottom

dishes (MatTek Corporation; Ashland, MA) 48 hours prior to experimentation. The cells

were first washed once with warmed glucose- and FBS-free medium and then incubated

with 10–20 μM NIR-glucosamine or free NIR dye for 30 minutes at 37 °C. Subsequently,

the cells were washed three times with medium and imaged. A Nikon Eclipse TE2000-U

fluorescence microscope equipped with a mercury lamp, indocyanine green (ICG) filter

set and a Hamamatsu ORCA II BT 512 camera controlled by Metamorph software v6.1

(Molecular Devices Corporation; Downingtown, PA) was used for imaging.

2.3 Results and Discussion

To synthesize NIR-glucosamine, we first activated glucosamine hydrochloride

with sodium methoxide, followed by conjugating IRDye[TM] 800CW NHS ester with the

Scheme 2.1. Reaction scheme for IRDye[TM] 800CW-glucosamine
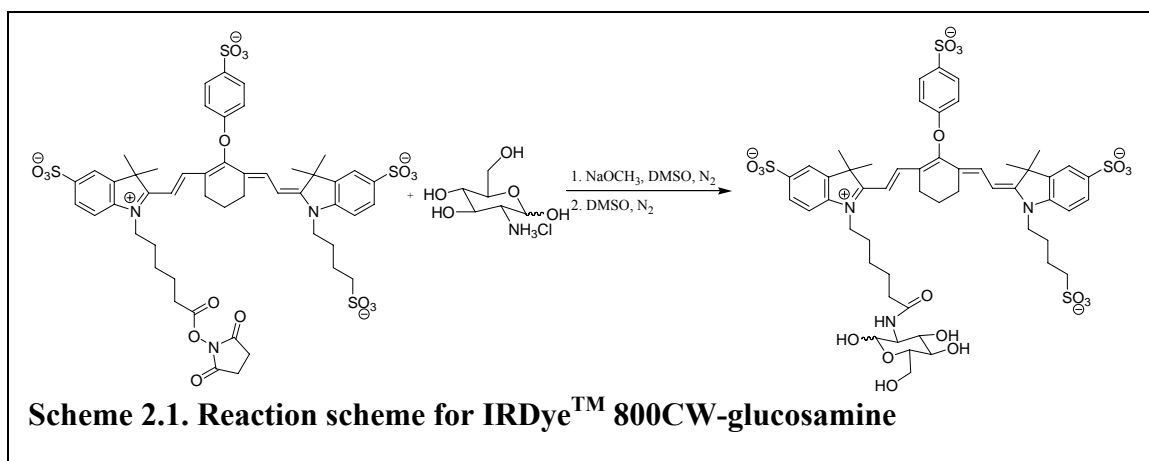
2-amino group of the glucosamine (Scheme 2.1). The resulting NIR-glucosamine was

purified by semipreparative HPLC and then characterized by NMR and mass

spectrometry. The maximum absorption and fluorescence emission wavelengths of NIR-

glucosamine (λ_{ab} = 774 nm and λ_{em} = 800 nm) in water are identical to those of free

NIR dye (IRDye800 acid) (Figure 2.2).

To study the stability of NIR-glucosamine, absorbance and fluorescence spectra were collected 13 times over 31 days and the results are displayed in Figures 2.3 and 2.4. Maximum

Figure 2.2. Absorption and fluorescence curves of NIR-glucosamine in water
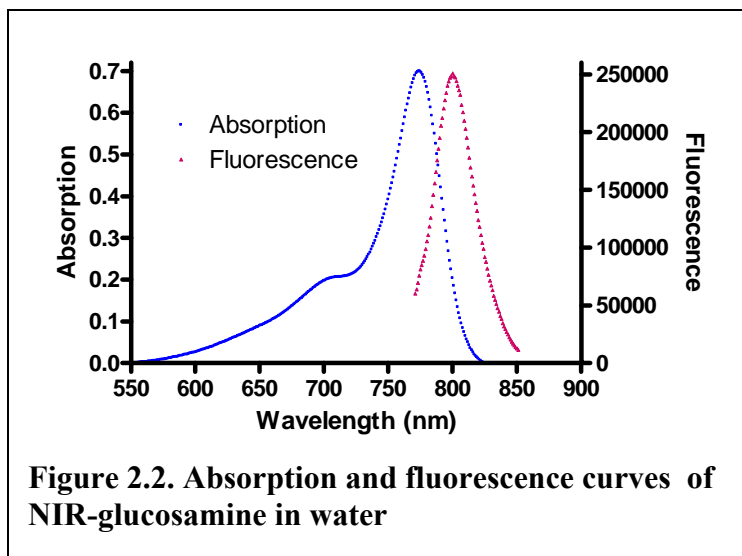
absorption and fluorescence of free dye in DMSO and all NIR-glucosamine samples are

listed in Table 2.2. The absorption and fluorescence λ_{max} of NIR-glucosamine shifted ~23

nm and ~22 nm respectively in aqueous solutions compared to solutions made in DMSO

due to solvent effect.

The stability analysis of NIR-glucosamine shows that the compound is stable in

Table 2.2. Maximum absorption and fluorescence of free dye and NIR-glucosamine samples

Sample	free dye DMSO	NIR-glu DMSO	NIR-glu pH 5	NIR-glu pH 6	NIR-glu PBS	NIR-glu pH 8	NIR-glu pH 9	NIR-glu DI water
λ_{ab} (nm)	797	797	774	774	774	774	774	774
λ_{em} (nm)	820	820	798	798	798	798	798	800
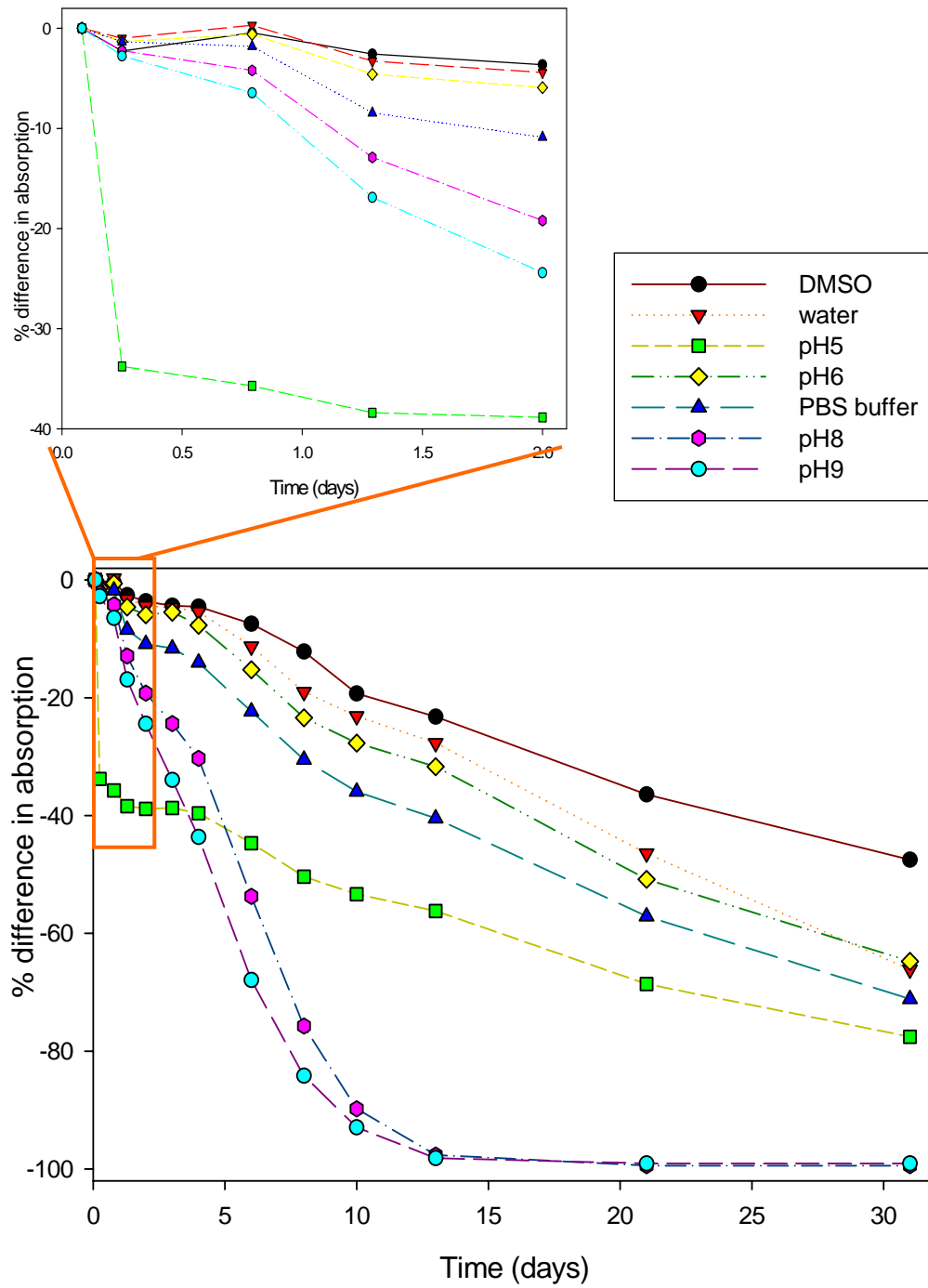
Figure 2.3. Absorbance percentage differences of NIR-glucosamine samples over 31 days
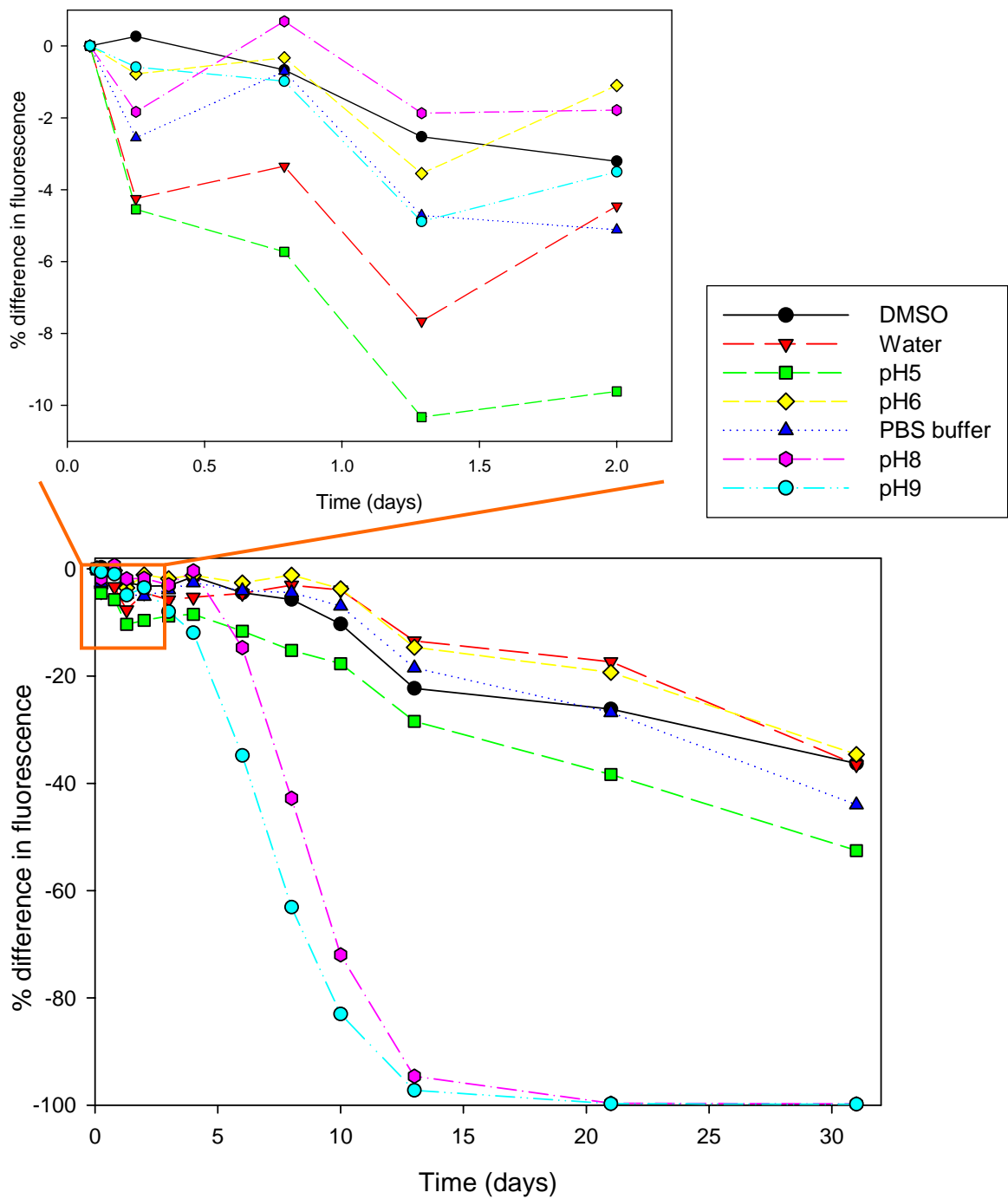
Figure 2.4. Fluorescence percentage differences of NIR-glucosamine samples over 31 days

DMSO, water, acidic solutions, and PBS buffer solution, but relatively unstable in basic solutions. In basic solutions, the highly conjugated cyanine backbone in NIR-glucosamine could possibly be broken by a nucleophile, as shown in Figure 2.5. As the cyanine backbone is the basic of NIR-glucosamine absorption at 774 nm, the decomposed molecule lost NIR absorption. Figure 2.3 and Figure 2.4 show that the half-lives of NIR-glucosamine in DMSO, water, pH 5 buffer, pH 6 buffer, and PBS buffer solutions are longer than one month. Even in basic solutions the molecule has half-lives of about 7 days (in pH 9 buffer) and 8 days (in pH 8 buffer), which is much longer than the half-life of [18]FDG (110 minutes).

In a preliminary study of the in vivo tumor targeting capabilities of NIR-glucosamine, an SW480*neo* tumor-bearing mouse was injected with 20 nmoles of NIR-glucosamine and imaged over time using the IVIS Imaging System 200. Fluorescence images taken pre-injection as well as approximately three minutes and six hours post-injection of NIR-glucosamine are shown in Figure 2.6; the fluorescence images are also overlaid onto the corresponding photographic images for orientation. Prior to injection,

Figure 2.5. Decomposition of NIR-glucosamine in basic solution
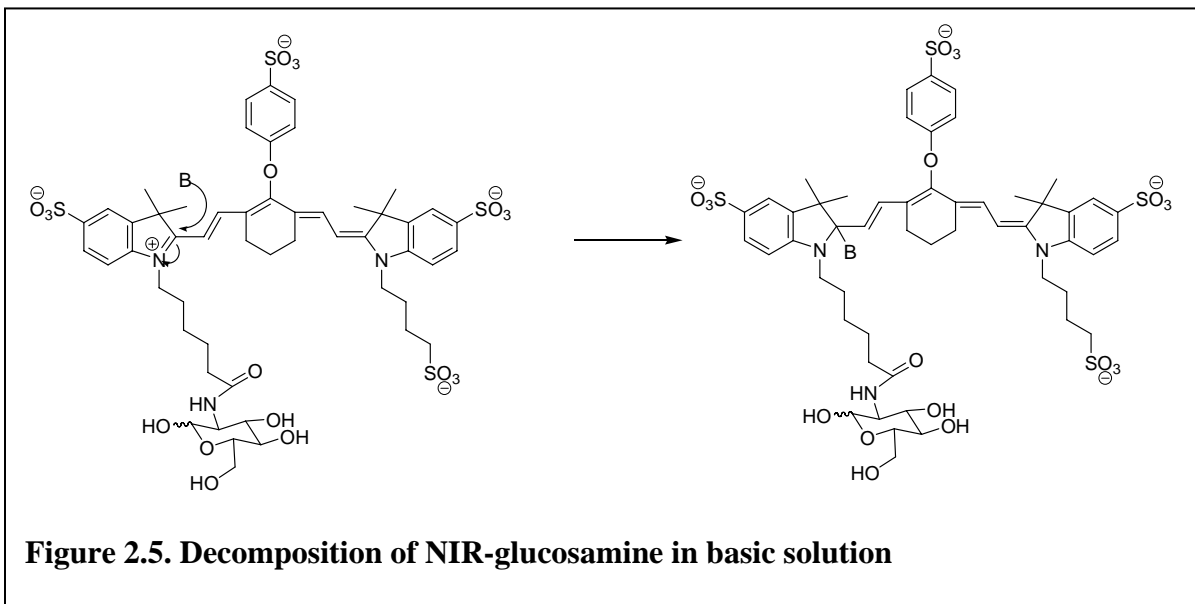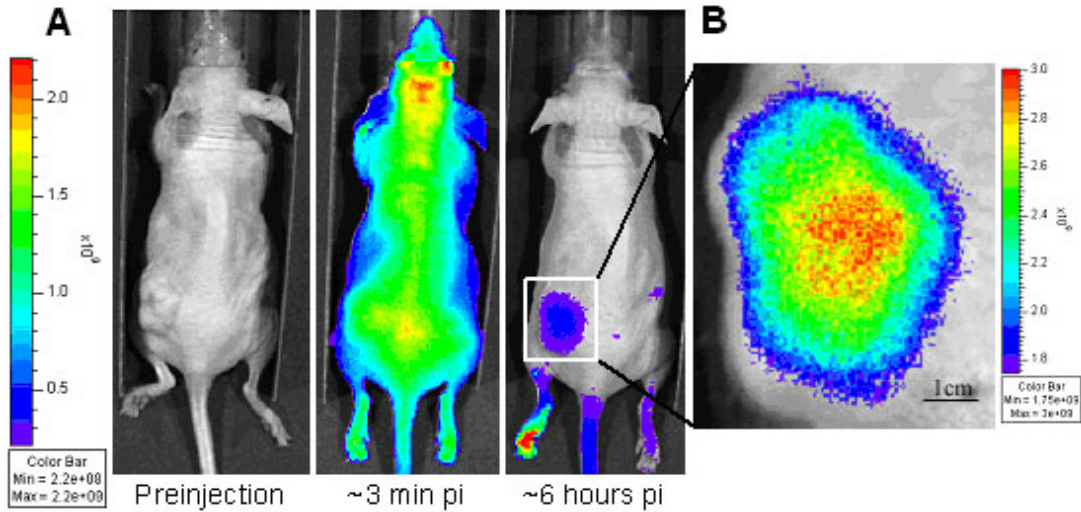
Figure 2.6. Biodistribution and accumulation of NIR-glucosamine in real-time.
(A) Fluorescence images of an SW480 tumor-bearing mouse overlaid onto the
corresponding photographic images, displayed on a color bar scale ranging from
2.2×10^8 to 2.2×10^9 photons/sec/cm^2/sr (acquired using FOV C and medium
binning). Substantial accumulation of NIR-glucosamine is seen in the tumor region
relative to the normal tissues approximately six hours post-injection. (B) Zoomed
image of the tumor region with better resolution on a color bar scale ranging from
1.75×10^9 to 3×10^9 photons/sec/cm^2/sr (acquired using FOV B and small binning).

the mice are essentially devoid of NIR fluorescence, revealing the negligible

autofluorescence of tissue in the exploited wavelength region. Approximately 3 minutes

post-injection, the NIR-glucosamine appears to be fairly uniformly distributed throughout

the mouse with some increased signal near the retroorbital injection site (right eye).

However, almost six hours post-injection, substantial accumulation of NIR-glucosamine

is apparent in the tumor tissue. The bright fluorescence signal on the left rear paw is

believed to result from urine contamination and is not present in other imaging studies.

Figure 2.6B displays a zoomed image of the tumor region, imaged using a smaller IVIS

field of view (FOV B = 6.4×6.4 cm), with better resolution (binning = 4×4), and

presented on a different average radiance scale. Quantification of the fluorescent signal in

the tumor region relative to the normal tissue on the opposite hindlimb demonstrates a

2.3-fold tumor-specific enhancement, suggesting that NIR-glucosamine specifically labels tumor tissue in vivo.

Two days after optical imaging, the mouse shown in Figure 2.6 was injected with 118 µCi of ^{18}FDG and dynamically imaged in the Concorde MicroSystems microPET scanner. A summation of the microPET images taken over an hour and ten minutes post-injection of ^{18}FDG is shown in Figure 2.7A. As expected, enhanced PET signal resulting from increased uptake and accumulation of ^{18}FDG is seen in the highly metabolic tissues including the brain, heart, and tumor. The bladder is also significantly bright due to the renal excretion of ^{18}FDG. For comparison, the optical image demonstrating NIR-glucosamine accumulation six hours post-injection is shown in Figure 2.7B. We originally attributed the lack of fluorescence signal emanating from the heart and brain following injection with NIR-glucosamine to decreased sensitivity in deeper tissues and the potential that NIR-glucosamine may not cross the blood brain barrier. Further studies have demonstrated otherwise as discussed below.

Figure 2.7C displays a coronal slice through the tumor of the ^{18}FDG-PET image for comparison to the tumor-specific accumulation of NIR-glucosamine (Figure 2.7D). It is noteworthy that both images have a similar size and shape, indicating potential correlation between the two imaging probes and methodologies. However, the central region of the tumor is devoid of ^{18}FDG-PET signal while the optical image shows substantial fluorescence intensity mid-tumor. This observation is presumably due to the fact that the IVIS Imaging System produces two-dimensional projection images of fluorescence intensity and is essentially a volumetric ensemble of all the photons emanating from the interrogated regions, whereas the microPET image is a slice through
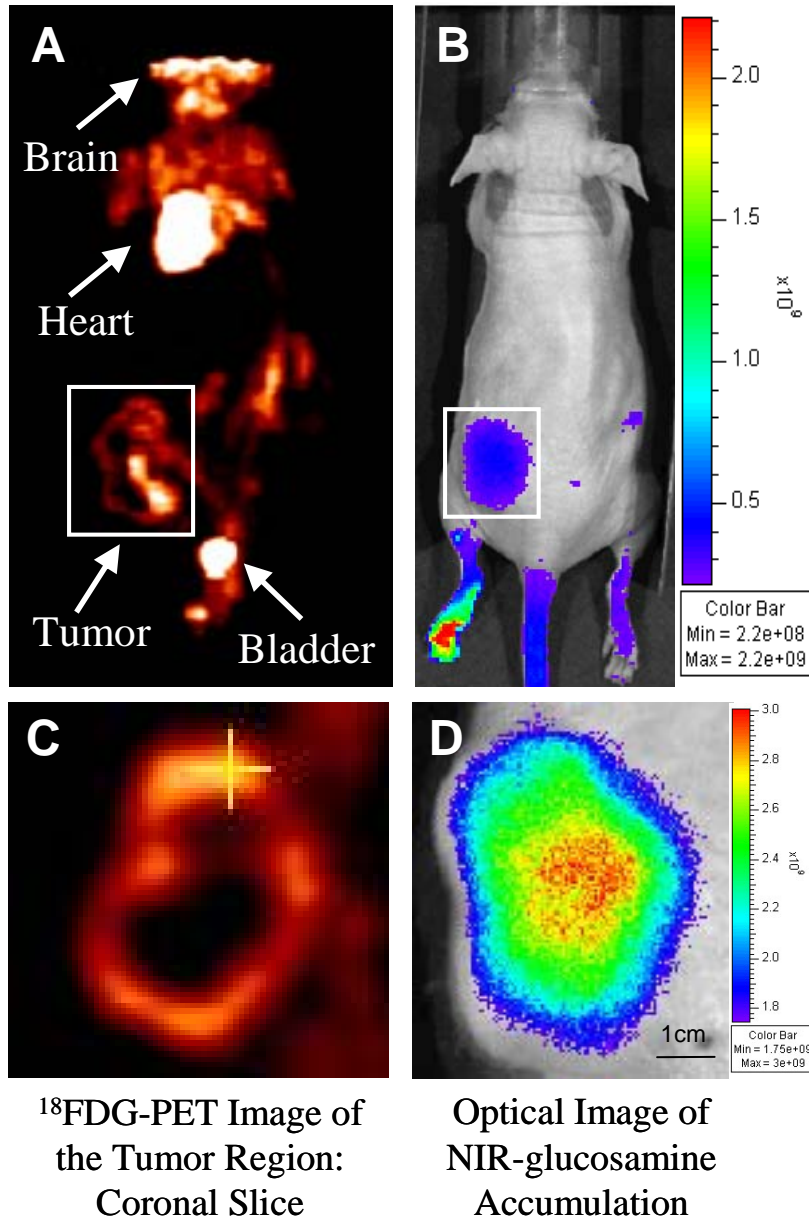
Figure 2.7. Comparison of [18]FDG signal to NIR-glucosamine accumulation in the tumor region of the same SW480 tumor-bearing mouse. (A) The microPET image illustrates [18]FDG accumulation in the highly metabolic tissues (brain, heart, and tumor) as well as the bladder due to renal excretion of [18]FDG. (B) The optical image captured six hours post-injection shows substantial accumulation of NIR-glucosamine in the same tumor two days prior to [18]FDG-microPET imaging. (C) A coronal slice through the tumor of the [18]FDG-PET image for comparison to the tumor-specific accumulation of NIR-glucosamine (D). Zoomed optical image of the tumor region with better resolution on a color bar scale ranging from 1.75×10^9 to 3×10^9 photons/sec/cm^2/sr.

the tumor itself. This discrepancy is analogous to the difference between fluorescence and confocal microscopy. It is likely that the dark region on the ^{18}FDG-microPET image represented necrotic tissue that was not evident in the 2D optical projection image. (In later studies, it became apparent that unlike ^{18}FDG, NIR-glucosamine does label necrotic and transitioning tissues, which may also account for the difference.) Qualitatively, but not quantitatively, the tumor-specific uptake of NIR-glucosamine appears to mimic that of ^{18}FDG uptake and accumulation. We therefore set out to determine the uptake mechanism responsible for tumor-specific labeling by NIR-glucosamine and to compare the in vivo biodistribution, clearance, and accumulation of NIR-glucosamine with free NIR dye.

To evaluate the in vivo biodistribution, clearance, and accumulation of NIR-glucosamine compared to free NIR dye, a pilot imaging study was performed in four SW480*neo* tumor-bearing mice. Approximately four and a half weeks post-implantation, the tumors were externally visible but fairly small (2 – 8 mm in their longest dimension). Following an overnight fast, the tumor-bearing mice were retroorbitally injected with 20 nmoles of free NIR dye and imaged over 24 hours using the Xenogen IVIS Imaging System 200. Two days later, the same mice were injected with NIR-glucosamine and again monitored over 24 hours post-injection. The fluorescence intensity of the tumor and normal regions were subsequently quantified in terms of average radiance (photons/sec/cm^2/steradian) to generate time activity curves and determine tumor specificity. It is important to note that since these mice each had two flank tumors, the opposite hindlimb could not be used as the "normal" tissue control. Thus, several ROIs were evaluated to determine the most appropriate "normal" tissue region, including

60

regions (1) over one forelimb, (2) along the midline (spine) between the two flank tumors, (3) slightly to the right or left of the spine between the two flank tumors, (4) between the forelimbs and (5) below the tumors on the lower portion of a hindlimb. The "normal" region defined over one forelimb consistently provided the highest tumor to normal contrast. However, this region did not appear to accurately represent normal tissue biodistribution as evident even in the immediately post-injection images (ex. Figure 2.6A). The "normal" regions defined along the spine and slightly offset from the spine demonstrated increased fluorescence intensity relative to the rest of the normal tissue, even immediately post-injection. These ROIs were also too close to the bladder and presumably included some signal from the renally cleared agents. Finally, the "normal" ROI between the shoulders consistently demonstrated a different clearance profile than

Figure 2.8. Time activity curves for NIR-glucosamine and free NIR dye in the tumor region and "normal" lower hindlimb tissue of mice bearing relatively small SW480 xenograft tumors. The same average radiance data up to four hours post-injection is displayed in the inset plot. The NIR-glucosamine appears to clear slightly faster than the free NIR dye in both the tumor and normal regions.

61

either the tumor or the other normal ROIs and was consequently eliminated. Thus, all of

the results presented herein result from quantitative analysis of the tumor ROI relative to

the lower portion of the hindlimb.

The in vivo time activity curves of NIR-glucosamine and free NIR dye in mice

bearing relatively small SW480*neo* tumors are shown in Figure 2.8; the same average

radiance data up to four hours post-injection is displayed as an inset. The NIR-

glucosamine and free NIR dye appear to clear from the tumor and normal tissues with

slightly different clearance profiles. More specifically, the time necessary to clear half of

the maximum fluorescence intensity occurring immediately post-injection is
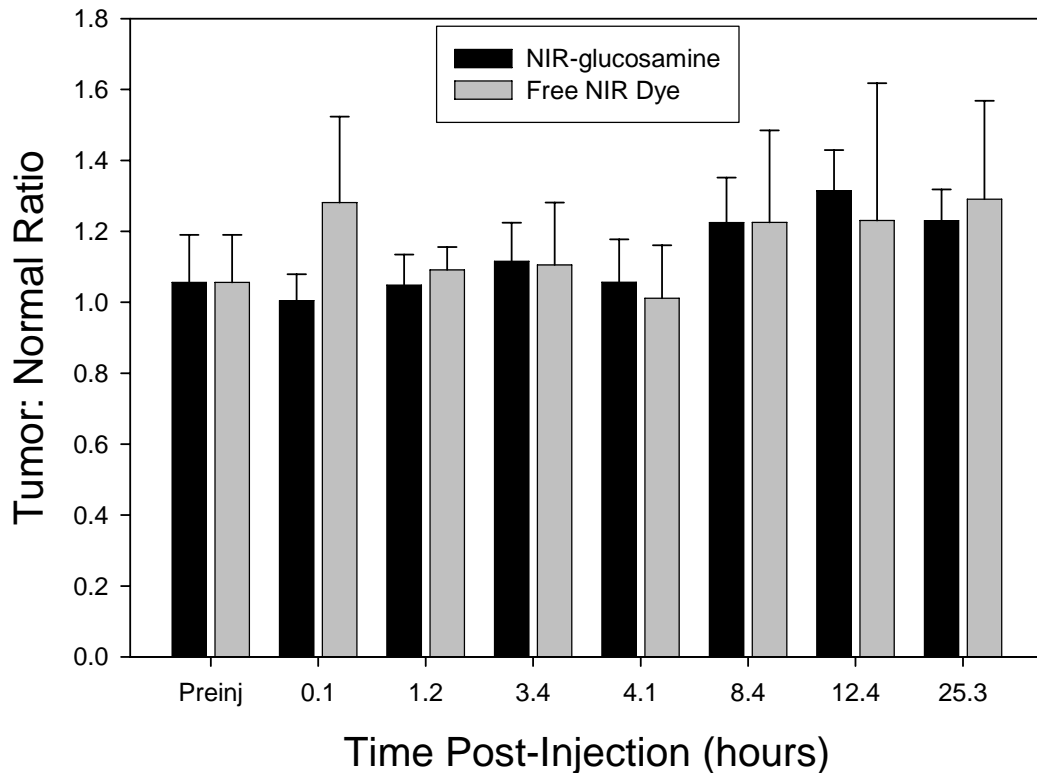
Figure 2.9. The tumor to normal contrast ratios of mice bearing relatively small SW480 xenograft tumors at each time point post-injection. Overall, both agents appear to provide very little to no tumor-specific contrast enhancement, suggesting a potential size or vascularity requirement for substantial tumor uptake.

approximately 2.5 hours for the free NIR dye, but only ~ 1.5 hours for the NIR-glucosamine. The faster rate of clearance presumably results from the increased polarity and therefore water solubility of NIR-glucosamine relative to the free NIR dye, which is more lipophilic. Overall, both agents appear to provide very little to no contrast enhancement in the relatively small tumors (Figure 2.9), suggesting a potential size or vascularity requirement for substantial tumor uptake.

Several weeks later, when the tumors approximately doubled in size, both the free NIR dye and NIR-glucosamine were injected to the same animals again. The injected agents provided enhanced tumor-specific contrast relative to the adjacent normal hindlimb tissue. The time activity curves and tumor to normal contrast ratios for two
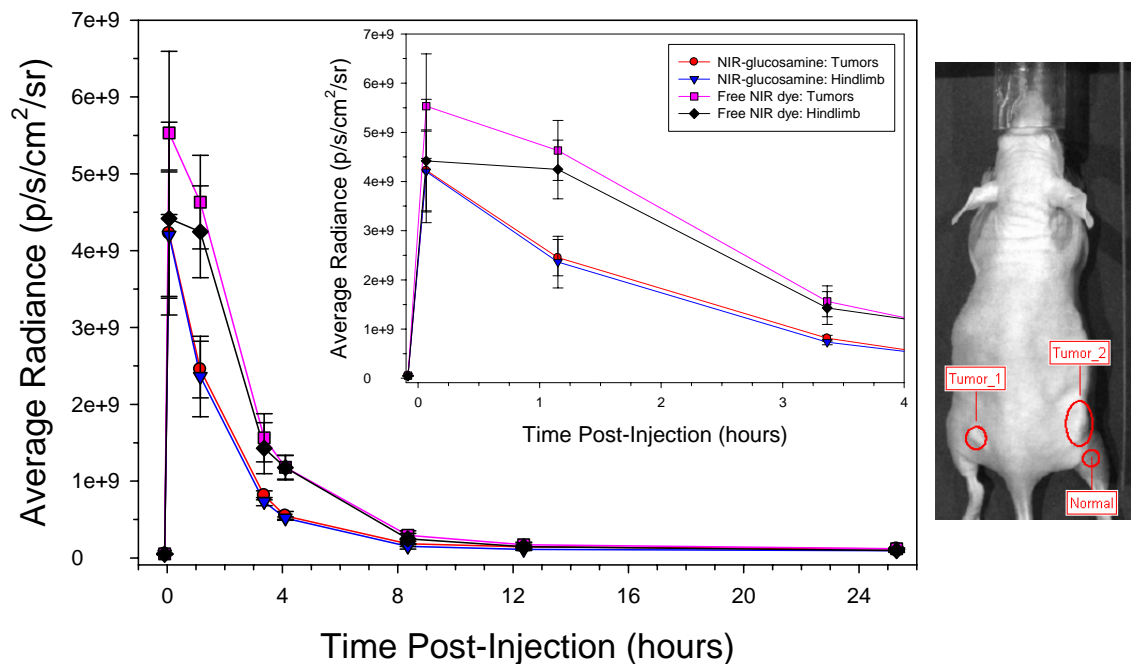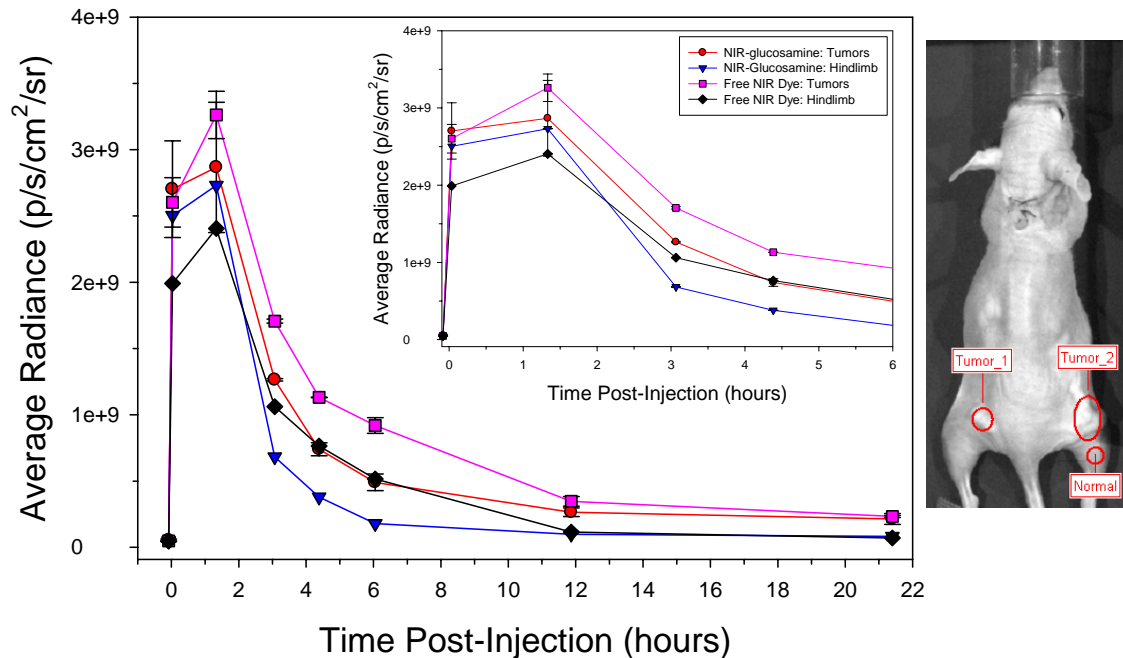

Figure 2.10. Time activity curves for NIR-glucosamine and free NIR dye in the tumor region and "normal" lower hindlimb tissue of mice bearing relatively larger SW480 xenograft tumors. The same average radiance data up to six hours post-injection is displayed in the inset plot. The NIR-glucosamine appears to clear slightly faster than the free NIR dye in the normal hindlimb region.

mice imaged simultaneously following retroorbital injection of 20 nmoles of free NIR

dye or NIR-glucosamine are shown in Figures 2.10 and 2.11, respectively. As previously

demonstrated in Figure 2.8, the NIR-glucosamine appears to clear more rapidly than the

free NIR dye, particularly from the normal hindlimb tissue (Figure 2.10 inset). As a result,

the apparent tumor to normal contrast from NIR-glucosamine increases from 1.0

immediately post-injection to a maximum of 2.7 six hours post-injection (Figure 2.11).

This 2.7-fold contrast enhancement persists for the duration of the study (~24 hours).

Conversely, the tumor to normal ratio from the free NIR dye is only 1.8 at six hours post-
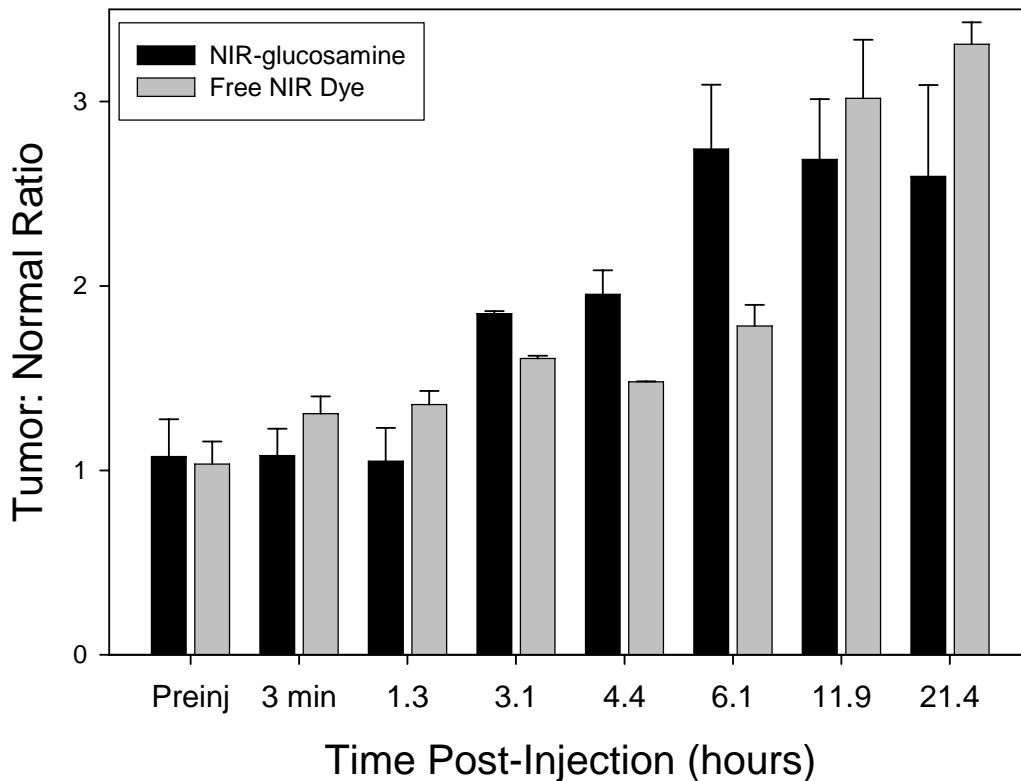
Figure 2.11. The tumor to normal contrast ratios of mice bearing relatively larger SW480 xenograft tumors at each time point post-injection. The NIR-glucosamine reaches a maximum tumor to normal contrast ratio (2.7) at six hours post-injection, while the free NIR dye contrast steadily rises to 3.3 over 24 hours post-injection. This discrepancy is presumably due to the faster rate of NIR-glucosamine clearance in the normal hindlimb tissue, which appears to result in earlier tumor-specific contrast and potentially less toxicity.

injection, but steadily increases to 3.3-fold at 21 hours post-injection. Since the

fluorescence intensity in the free NIR dye-containing tumors is consistently higher than

the fluorescence intensity in the NIR-glucosamine-containing tumors, this contrast

discrepancy is presumably due to the faster normal tissue washout of NIR-glucosamine

rather than preferential NIR-glucosamine accumulation over free NIR dye. This

increased normal tissue clearance due to the contribution of the D-glucosamine may

prove beneficial over free NIR dye due to the earlier contrast enhancement and could

potentially provide a reduction in cytotoxicity. However, more animal studies are

necessary to evaluate the potential advantages of NIR-glucosamine over the use of free

NIR dye for tumor labeling.

Since both NIR-glucosamine and free NIR dye provide similar contrast

enhancement in SW480*neo* tumor-bearing mice, it is possible that the conjugated

compound has poor blood stability. HPLC analysis was used to determine whether or not

NIR-glucosamine is degraded to free NIR dye in the presence of blood components on a

relevant time scale. Following a 0, 4, or 8 hour incubation in whole blood, the elution

Table 2.3. Blood stability analysis.

Compound	Experimental Condition	Peak Elution Time (min) NIR-gluc	Area	Peak Elution Time (min) Free NIR dye	Area	% NIR-glucosamine[a]	% Free NIR Dye[b]
Free NIR Dye	Stock Solution	18.3	1.3	22.5	95	1 %	99 %
NIR-glucosamine	Stock Solution	18.1	88	22.6	7.7	92 %	8 %
NIR-glucosamine	Diluted in blood and immediately purified	18.0	66	22.5	6.9	91 %	9 %
NIR-glucosamine	In whole blood for 4 hours	18.2	53	23.1	7.1	88 %	12 %
NIR-glucosamine	In whole blood for 8 hours	18.1	61	23.0	4.7	93 %	7 %

[a] $\% \, Free \, NIR \, Dye = \dfrac{Area \, at \, 23 \, minutes}{Area \, at \, 18 \, min + Area \, at \, 23 \, min} \times 100$;   [b] $\% \, NIR\text{-}glucosamine = \dfrac{Area \, at \, 18 \, minutes}{Area \, at \, 18 \, min + Area \, at \, 23 \, min} \times 100$
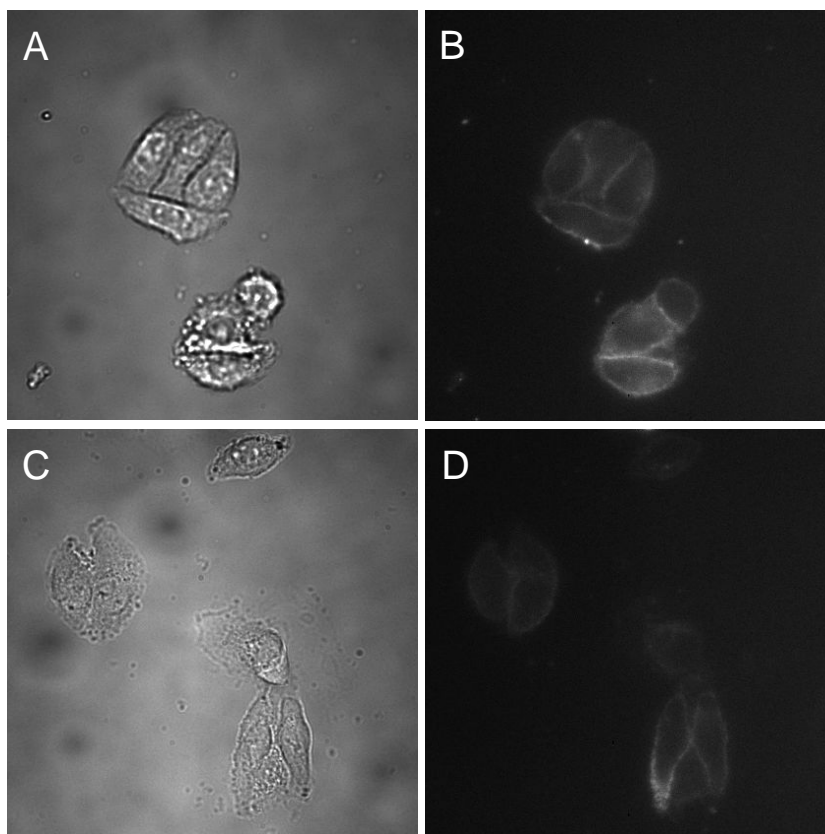
Figure 2.12. Fluorescence microscopy of SW480 cells incubated with NIR-glucosamine (white light image in A and NIR fluorescence in B) or free NIR dye (white light image in C and NIR fluorescence in D) in glucose- and FBS-free medium. The fluorescence signal appears to be primarily associated with the cell membrane. The localization is better demonstrated by the full, pseudo-confocal z-stack.

profile of NIR-glucosamine was compared to that of the NIR-glucosamine and free NIR dye stocks at 782 nm (Table 2.3). NIR-glucosamine and free NIR dye eluted at ~18.1 minutes and ~22.5 minutes, respectively. The shorter elution time for NIR-glucosamine indicates an increased polarity relative to the free NIR dye, as previously discussed. The reduction in area following incubation in whole blood results from poor baseline in HPLC chromatograph due to the very low signal of these samples. The small fraction of the NIR-glucosamine stock (~8 %) that eluted at 22.6 minutes is likely free NIR dye. The NIR-glucosamine sample used for these studies was approximately six months old

and had probably degraded to free NIR dye slightly. However, this small contribution to the entire elution profile remains less than 13 % after exposure to whole blood components for 4 or 8 hours. This suggests that the NIR-glucosamine remains intact and is stable in blood for at least 8 hours.

Finally, fluorescence microscopy studies were performed to assess the cellular localization of NIR-glucosamine and free NIR dye. Figure 2.12 displays one slice of a pseudo-confocal NIR z-stack of SW480*neo* cells incubated with NIR-glucosamine (A, B) or free NIR dye (C,D) for 30 minutes. Both agents appear to be primarily localized to the outer cellular membrane. This localization is better demonstrated by the full z-stack, which shows localized fluorescence at the top of the cell that spreads radially outwards as one traverses through the cell. These fluorescence images further suggest non-specific binding to the lipid membrane.

2.4 Conclusion

In summary, this study describes the synthesis and characterization of an alternative optical ^{18}FDG analogue. Preliminary imaging studies in an SW480*neo* mouse model of human colon cancer suggest that NIR-glucosamine specifically labels tumor tissue in vivo with a 2.3 to 2.7-fold contrast enhancement over normal tissue. This tumor-specific fluorescence signal also appears to mimic that of ^{18}FDG accumulation. Blood stability analysis and preliminary tissue imaging studies suggest that NIR-glucosamine is not degraded to free NIR dye in blood and appears to be able to extravasate from the vasculature at least in liver, kidneys and lungs.

Overall, NIR-glucosamine and free NIR dye appear to provide enhanced tumor

contrast over normal tissues in reasonably sized tumors. Although the mechanism of uptake and accumulation remains unknown, the increased rate of NIR-glucosamine clearance from the normal tissue due to increased polarity may prove beneficial for imaging of vascular permeability and could result in less toxicity. However, additional animal studies are necessary to evaluate the potential advantages of NIR-glucosamine over free NIR dye for tumor labeling.

2.6 References

(1)   Bromiley, A.; Welch, A.; Chilcott, F.; Waikar, S.; McCallum, S. et al. Attenuation correction in PET using consistency conditions and a three-dimensional template. *Ieee Transactions on Nuclear Science* **2001***, 48*, 1371-1377.

(2)   Couper, G. W.; McAteer, D.; Wallis, R.; Welch, A.; Norton, M. et al. Quantification of FDG-PET scans in patients with oesophageal and gastric cancer. A study of 40 patients. *British Journal of Surgery* **2002***, 89*, 64-64.

(3)   Couper, G. W.; Wallis, F.; Welch, A.; Sharp, P. F.; Park, K. G. M. et al. The role of FDG-PET in the early detection of response of colorectal liver metastases to chemotherapy. *Gut* **2002***, 50*, A107-A107.

(4)   Danthi, S. N.; Pandit, S. D.; Li, K. C. P. A primer on molecular biology for imagers: VII. Molecular imaging probes. *Academic Radiology* **2004***, 11*, 1047-1054.

(5)   Weissleder, R. Molecular imaging in cancer. *Science* **2006***, 312*, 1168-1171.

(6)   Zhang, M.; Zhang, Z. H.; Blessington, D.; Li, H.; Busch, T. M. et al. Pyropheophorbide 2-deoxyglucosamide: A new photosensitizer targeting glucose transporters. *Bioconjugate Chemistry* **2003***, 14*, 709-714.

(7)   Miller, J. C.; Thrall, J. H. Clinical molecular imaging. *Journal of the American College of Radiology* **2004***, 1*, 4-23.

(8)   Gambhir, S. S. Molecular imaging of cancer with positron emission tomography. *Nature Reviews Cancer* **2002***, 2*, 683-693.

(9)   Yoshioka, K.; Takahashi, H.; Homma, T.; Saito, M.; Oh, K. B. et al. A novel fluorescent derivative of glucose applicable to the assessment of glucose uptake activity of Escherichia coli. *Biochimica Et Biophysica Acta-General Subjects* **1996***, 1289*, 5-9.

(10)   Yoshioka, K.; Saito, M.; Oh, K. B.; Nemoto, Y.; Matsuoka, H. et al. Intracellular fate of 2-NBDG, a fluorescent probe for glucose uptake activity, in Escherichia coli cells. *Bioscience Biotechnology and Biochemistry* **1996***, 60*, 1899-1901.

(11)   Yoshioka, K.; Oh, K. B.; Saito, M.; Nemoto, Y.; Matsuoka, H. Evaluation of 2-[N-(7-nitrobenz-2-oxa-1,3-diazol-4-yl)amino]-2-deoxy-D-glucose, a new fluorescent derivative of glucose, for viability assessment of yeast Candida albicans. *Applied Microbiology and Biotechnology* **1996***, 46*, 400-404.

(12)   Yamada, K.; Nakata, M.; Horimoto, N.; Saito, M.; Matsuoka, H. et al. Measurement of glucose uptake and intracellular calcium concentration in single, living pancreatic beta-cells. *Journal of Biological Chemistry* **2000***, 275*, 22278-22283.

(13)   Oh, K. B.; Matsuoka, H. Rapid viability assessment of yeast cells using vital staining with 2-NBDG, a fluorescent derivative of glucose. *International Journal of Food Microbiology* **2002***, 76*, 47-53.

(14)   Ye, Y. P.; Bloch, S.; Kao, J.; Achilefu, S. Multivalent carbocyanine molecular probes: Synthesis and applications. *Bioconjugate Chemistry* **2005***, 16*, 51-61.

(15)   Cheng, Z.; Levi, J.; Xiong, Z. M.; Gheysens, O.; Keren, S. et al. Near-infrared fluorescent deoxyglucose analogue for tumor optical imaging in cell culture and living mice. *Bioconjugate Chemistry* **2006***, 17*, 662-669.

(16)   Ke, S.; Wen, X. X.; Gurfinkel, M.; Charnsangavej, C.; Wallace, S. et al. Near-infrared optical imaging of epidermal growth factor receptor in breast cancer xenografts. *Cancer Research* **2003***, 63*, 7870-7875.

(17)   Witty, J. P.; Mcdonnell, S.; Newell, K. J.; Cannon, P.; Navre, M. et al. Modulation of Matrilysin Levels in Colon-Carcinoma Cell-Lines Affects Tumorigenicity in-Vivo. *Cancer Research* **1994***, 54*, 4805-4812.

CHAPTER III

A NOVEL CONJUGABLE TRANSLOCATOR PROTEIN LIGAND LABELED WITH A
FLUORESCENCE DYE FOR IN VITRO IMAGING

3.1 Introduction

Molecular imaging (MI) has emerged as an important multidisciplinary area which involves radiology, chemistry, biology, biochemistry, physics, engineering, and medicine. MI combines molecular agents with imaging tools to follow specific molecular pathways in the body and can be widely applied in locating, diagnosing, and treating disease. Synthetic chemistry is essential to MI by providing potent imaging agents.

The translocator protein (18 kDa), TSPO, previously known as the peripheral-type benzodiazepine receptor has become an interesting target in MI[1]. TSPO is a mitochondrial protein which is associated with a variety of biological activities such as cell proliferation, apoptosis, immunomudulation, steroidogenesis, and transport of porphyrin and heme[1-3]. TSPO is ubiquitously expressed throughout the human body, with high level of expression in non-neoplastic diseases such as ischemia, brain damage induced by toxins, viral encephalitis, hepatic encephalopathy, epilepsy, nerve degeneration, and trauma[4]. TSPO overexpression has also been observed in various cancers including breast, glioma, prostate, colorectal, esophageal, ovarian, and small cell lung cancer[4].

Several selective and potent TSPO ligands have been developed, such as benzodiazepines (Ro5-4864), isoquinoline carboxamides (PK11195), indolacetamide derivatives (FGIN-1-27), pyrisanoindole derivatives (SSR180575), and phenoxylphenyl

71

acetamide derivatives (DAA1106 or DAA1097). The study of TSPO, an important mitochondrial membrane protein is currently limited because only two ligands that exist are conjugable to signaling moieties for tracking and quantitation. An FGIN analogue was labeled with a fluorophore (NBD) which is not ideal for in vitro imaging due to the low molar extinction coefficient (~ 8000 L mol^{-1} cm^{-1})[5,6]. Our lab developed a PK11195 analogue which has a six-carbon linker and a terminal primary amino group[7]. Development of conjugable forms of the numerous PBR ligands would facilitate the study of TSPO and possibly allow for it to be used as a target for in vivo imaging.

A conjugable form of PK11195 has been reported and the molecule has been coupled to a lanthanide chelate[7] and a fluorescence dye[8]. These TSPO-targeted agents showed good TSPO binding activity, allowing in vitro molecular imaging studies. Ro5-4864 and PK11195 are reversible competitive inhibitors of each other, and they show distinct biological properties in inflammation[9], depression[10], nociception[11] and apoptosis enhancement[4]. Given these facts, to further study TSPO function in relation to its expression levels, a conjugable form of Ro5-4864 was deemed as a necessity.

We report herein the synthesis of a conjugable form of Ro5-4864 having a six-carbon spacer (C_6Ro5-4864). Through the primary amino group, this molecule can be conjugated to a variety of signaling moieties, thus allowing the use of different imaging modalities. Lissamine-rhodamine B sulfonyl chloride, a fluorescence dye with a high molar extinction coefficient (88,000 L/mol cm in methanol), was selected for conjugation to C_6Ro5-4864. The resulting TSPO-targeted fluorophore, lissamine-C_6Ro5-4864, labels TSPO-expressing cells selectively and shows promise for MI studies in imaging disease states where TSPO levels are affected, either as the cause or the outcome of the disease.

3.2 Experimental Procedures

3.2.1 Synthesis

7-Chloro-5-(4-chlorophenyl)-1-methyl-1H-benzo[1,2,4]triazepin-2-one **(2).** (5-Chloro-2-(methylamino)phenyl)(4-chlorophenyl)methanone **1** (2 g, 7 mmol) and ethyl carbazate (1.5 g, 17 mmol) were stirred at 210 °C for 3.5 h. After the reaction was cooled to room temperature, the product was purified by column chromatography on silica gel by eluting with 1:3 ethyl acetate/hexanes to yield **2** as a yellow solid (774 mg, 34%). ^{1}H NMR 300 MHz (CDCl$_3$) δ 7.38-7.53 (6H, m), 7.15 (1H, d, J=8.7 Hz), 7.05 (1H, d, J=2.7 Hz), 3.29 (3H, s); MS (MALDI)$^+$ m/z 320.3 ([M + H]$^+$, 100%).

(6-Bromohexyloxy)(tert-butyl)dimethylsilane **(4).** To a solution of 6-bromo-1-hexanol (906 mg, 5 mmol) in dichloromethane (25 mL) at 0 °C was added imidazole (1.02 g, 15 mmol). After 5 min, 4-(dimethylamino)pyridine (DMAP) (60 mg, 0.5 mmol) was added, followed by *tert*-butyldimethylsilyl chloride (1.5 g, 10 mmol). The resulting solution was stirred at 0 °C for 2 h, quenched with 30 mL water, and extracted with dichloromethane (3 × 30 mL). The organic layers were combined, dried over sodium sulfate, and concentrated by vacuum rotary evaporation. The product was purified by silica gel chromatography using 1:20 ethyl acetate/hexanes as the eluent. Compound **4** was isolated as a colorless liquid (1.3 g, 88%). ^{1}H NMR 300 MHz (CDCl$_3$) δ 3.60 (t, J=6.3 Hz, 2H), 3.40 (t, J=6.9 Hz, 2H), 1.86 (q, J=5.1 Hz, 2H), 1.54-1.35 (m, 6H), 0.89 (s, 9H), 0.04 (s, 6H). MS (GC): 295, 293 [M•].

(Z)-3-(6-(*tert*-Butyldimethylsilyloxy)hexyl)-7-chloro-5-(4-chlorophenyl)-1-methyl-1H-benzo[e][1,2,4]triazepin-2(3H)-one **(5).** Sodium hydride (60% in mineral oil) (20 mg, 0.5 mmol) was added to a stirring solution of compound **2** (256 mg, 0.8 mmol) in dry DMF (4 mL). The mixture was stirred under argon for 30 min. Compound **4** was then added

to the mixture, and the resulting mixture was stirred for another 30 min. The reaction solution was poured into 50 mL of a stirring 1 M ammonium chloride solution at 0 °C. The mixture was transferred to a separation funnel and extracted with ethyl ether (3 × 40 mL). The organic layers were combined, dried over sodium sulfate, and concentrated by vacuum rotary evaporation. The crude product was purified by silica gel chromatography using gradient 1:20 to 1:4 ethyl acetate/hexanes as the eluent to give a yellow oil (349 mg, 89%). ^{1}H NMR 400 MHz (CDCl$_3$) δ 7.55-7.53 (m, 2H), 7.46 (dd, J=8.8, 2.4 Hz, 1H), 7.41-7.39 (m, 2H), 7.12 (d, J=8.8 Hz, 1H), 7.06 (d, J=2.4 Hz, 1H), 3.73 (bs, 1H), 3.55 (t, J=2.4 Hz, 2H), 3.23 (s, 3H), 1.65 (bs, 2H), 1.49-1.43 (m, 2H), 1.33-1.24 (m, 5H), 0.88 (s, 9H), 0.02 (s, 6H). MS (ESI)$^+$: 556.2 Da [M + Na]$^+$.

(Z)-7-Chloro-5-(4-chlorophenyl)-3-(6-hydroxyhexyl)-1-methyl-1H-benzo[e][1,2,4]triazepin-2(3H)-one (6). Tetrabutylammonium fluoride (TBAF) (3.5 mL 1 M solution in THF) was added to a stirring solution of compound **5** (377 mg, 0.7 mmol) in THF (2.5 mL) at 0 °C. The reaction solution was stirred at 0 °C for 3 h, quenched with 30 mL of water, and extracted with ethyl ether three times. The organic layers were combined, dried over sodium sulfate, and concentrated by vacuum rotary evaporation. The crude product was purified by column chromatography (silica gel) using 1:2 ethyl acetate/hexanes as eluent. Compound **6** was collected as a pale yellow oil (281 mg, 95%). ^{1}H NMR 300 MHz (CDCl$_3$) δ 7.55-7.53 (m, 2H), 7.46 (dd, J=9.0, 2.4 Hz, 1H), 7.41-7.38 (m, 2H), 7.12 (d, J=8.7 Hz, 1H), 7.06 (d, J=2.4 Hz, 1H), 3.72 (bs, 1H), 3.61-3.56 (m, 3H), 3.23 (s, 3H), 1.69-1.62 (m, 2H), 1.57-1.48 (m, 2H), 1.37-1.24 (m, 5H). ^{13}C NMR 75 MHz (CDCl$_3$) δ 163.6, 161.1, 145.5, 136.5, 134.5, 131.7, 130.3, 129.2, 129.0, 128.8, 128.5, 120.9, 62.8, 51.5, 35.5, 32.6, 27.7, 26.6, 25.4. MS (ESI)$^+$: 442.2 Da [M + Na]$^+$.

(Z)-6-(7-Chloro-5-(4-chlorophenyl)-1-methyl-2-oxo-1H-benzo[e][1,2,4]triazepin-3(2H)-yl)hexyl 4-Methylbenzenesulfonate (7). A solution of compound **6** (182 mg, 0.43 mmol) and triethylamine (188 µL, 1.3 mmol) in dry dichloromethane (6 mL) was stirred at 0 °C for 5 min. *p*-Toluenesulfonyl chloride (298 mg, 1.56 mmol) was added slowly to the above solution. The resulting mixture was warmed to room temperature and stirred overnight. The reaction was then quenched with 20 mL of water and extracted with dichloromethane (3 × 20 mL). The combined organic layers were dried over sodium sulfate and concentrated by vacuum rotary evaporation. The crude product was purified by silica gel chromatography using a 1:19 to 2:3 ethyl acetate/hexanes gradient as eluent. Compound **7** was isolated as a yellow oil (238 mg, 96%). ^{1}H NMR 300 MHz (CDCl$_3$) δ 7.77 (dm, *J*=8.1 Hz, 2H), 7.54-7.51 (m, 2H), 7.46 (dd, *J*=8.7, 2.4 Hz, 1H), 7.52-7.39 (m, 2H), 7.33 (d, *J*=7.8 Hz, 2H), 7.12 (d, *J*=8.7 Hz, 1H), 7.06 (d, *J*=2.4 Hz, 1H), 3.97 (t, *J*=6.3 Hz, 2H), 3.70-3.40 (m, 2H), 3.23 (s, 3H), 2.44 (s, 3H), 1.62-1.55 (m, 4H), 1.31-1.21 (m, 4H). MS (ESI)$^+$: 596.3 Da [M + Na]$^+$.

C$_6$Ro5-4864 (8). A sealed tube with a solution of compound **7** (25 mg, 44 µmol) in methanol (1 mL) was cooled to -78 °C and flushed with ammonia gas. After about 2.5 mL liquid ammonia was condensed, the tube was sealed and warmed to room temperature. The reaction was stirred under room temperature overnight. The mixture was concentrated by nitrogen flow, redissolved by dichloromethane, and treated with a saturated sodium bicarbonate solution. The mixture was extracted with dichloromethane three times. The organic layers were combined, dried over sodium sulfate, and concentrated by vacuum rotary evaporation. The crude product was purified by column chromatography (silica gel) using a gradient with dichloromethane and dichloromethane/methanol/ammonia (6:1:0.1) as the eluent. C$_6$Ro5-4864 was collected as a pale yellow oil (14 mg, 77%). ^{1}H NMR 300 MHz

(CDCl$_3$) δ 7.55-7.51 (m, 2H), 7.45 (dd, J=8.7, 2.4 Hz, 1H), 7.41-7.37 (m, 2H), 7.12 (d, J=8.7 Hz, 1H), 7.06 (d, J=2.4 Hz, 1H), 3.80-3.45 (m, 2H), 3.23 (s, 3H), 2.62 (bs, 2H), 1.65 (bs, 2H), 1.49-1.38-1.24 (m, 8H). ^{13}C NMR 75 MHz (CDCl$_3$) δ 163.6, 161.1, 145.5, 136.4, 134.5, 131.7, 130.2, 129.2, 129.0, 128.8, 128.5, 120.9, 51.5, 42.1, 35.5, 33.7, 27.7, 26.6, 26.5. MS (ESI)$^+$: 419.3 Da [M + H]$^+$.

Lissamine-C$_6$Ro5-4864. A mixture of lissamine rhodamine B sulfonyl chloride (mixed isomers) (10 mg, 17 μmol), C$_6$-Ro5-4864 (8 mg, 19 μmol), and triethylamine (15 μL) in dry dichloromethane (1.6 mL) was stirred at room temperature under argon flow for 2 h. The product was purified through column chromatography (silica gel) using a mixture of 24:1 dichloromethane:methanol as the eluent. Lissamine-C$_6$Ro5-4864 was isolated as a pink solid (Isomer I, 3.2 mg, 19%; Isomer II, 2.2 mg, 13%). ^{1}H NMR 500 MHz (CDCl$_3$) **Isomer I**: δ 8.81 (d, J=2.0 Hz, 1H), 7.96 (dd, J=8.0, 1.5 Hz, 1H), 7.55-7.53 (m, 2H), 7.47 (dd, J=8.5, 2.5 Hz, 1H), 7.41-7.39 (m, 2H), 7.29 (d, J=9.5 Hz, 2H), 7.20 (d, J= 8.0 Hz, 1H), 7.15 (d, J=9.0 Hz, 1H), 7.07 (d, J=2.0 Hz, 1H), 6.81 (dd, J=9.5, 2.5 Hz, 2H), 6.66 (d, J=2.5 Hz, 2H), 4.99 (t, J=6.5 Hz, 1H), 3.50-3.59 (m, 8H), 3.23 (s, 3H), 3.01 (q, J=7.0 Hz, 2H), 1.69-1.58 (m, 6H), 1.55-1.50 (m, 2H), 1.29 (t, J=7.5 Hz, 14H). **Isomer II**: δ 8.66 (s, 1H), 8.38 (dd, J=8.0, 1.0 Hz, 1H), 7.52-7.50 (m, 2H), 7.46 (dd, J=8.5, 2.5 Hz, 1H), 7.38-7.36 (m, 2H), 7.23 (d, J=7.5 Hz, 1H), 7.17 (d, J= 9.5 Hz, 1H), 7.14 (d, J=9.0 Hz, 1H), 7.04 (d, J=2.5 Hz, 1H), 6.85 (dd, J=9.5, 1.5 Hz, 2H), 6.70 (d, J=2.5 Hz, 2H), 5.24 (bs, 1H), 3.63-3.55 (m, 8H), 3.21 (s, 3H), 2.89 (q, J=6.5 Hz, 2H), 1.72-1.61 (m, 9H), 1.33 (t, J=7.5 Hz, 14H). MS (ESI)$^+$: 981.4 Da [M + Na]$^+$. Rf 0.23 (Isomer I), 0.14 (Isomer II) (4% methanol in dichloromethane).

3.2.2 Spectroscopic Characterization

The lissamine-C_6Ro5-4864 absorption and emission spectra were obtained using a Shimadzu 1700 UV-vis spectrophotometer and ISS PCI spectrofluorometer at room temperature on a 5 μM sample.

3.2.3 Binding Studies

C6 glioma cells were cultured in Dulbecco's modified Eagle medium (DMEM)-F12 medium (Gibco/Invitrogen) supplemented with 0.5% FBS and 2.5% horse serum (HS) at 3.7% CO_2. Cells were scraped from 150 mm culture dishes into 5 mL of phosphate-buffered saline (PBS), dispersed by trituration, and centrifuged at 500 x*g* for 15 min. Cell pellets were resuspended in PBS and assayed for protein concentration. [3H]PK11195 binding studies on 30 μg of protein from cell suspensions were performed as previously described[12]. Displacement studies using increasing concentrations of lissamine-C_6Ro5-4864 were performed in the presence of 15 nM [3H]PK11195. Data were analyzed using PRISM software (vs 4.0, GraphPad, Inc., San Diego, CA).

3.2.4 Cell Imaging

C6 rat glioma and MDA-MB-231 human breast carcinoma cells were plated in MaTek[TM] dishes. The growth media was removed and replaced with media containing the contrast agent. C6 and MDA-MB-231 cells were dosed with 100 nM lissamine-C_6Ro5-4864 for 30 min at 37 °C under 5% CO_2. Cells dosed with 100 nM free lissamine dye were imaged as control. At the end of the incubation time, cells were rinsed with PBS three times and imaged under a Nikon Eclipse TE2000-U microscope (Lewisville, TX).

3.2.5 In Vitro Competition

MDA-MB-231 human breast carcinoma cells were plated in MaTek[TM] dishes. The

growth media was removed and replaced with media containing the contrast agent. Unchallenged MDA-MB-231 cells were dosed with 5 μM lissamine-C_6Ro5-4864. Challenged cells were dosed with 5 μM lissamine-C_6Ro5-4864 and PK1195 (500 nM, 5 μM or 50 μM). All cells were incubated for 30 min at 37 °C under 5% CO_2. At the end of the incubation time, cells were rinsed with PBS three times and imaged under a Nikon Eclipse TE2000-U microscope (Lewisville, TX).

3.3 Results and Discussion

3.3.1 Synthesis
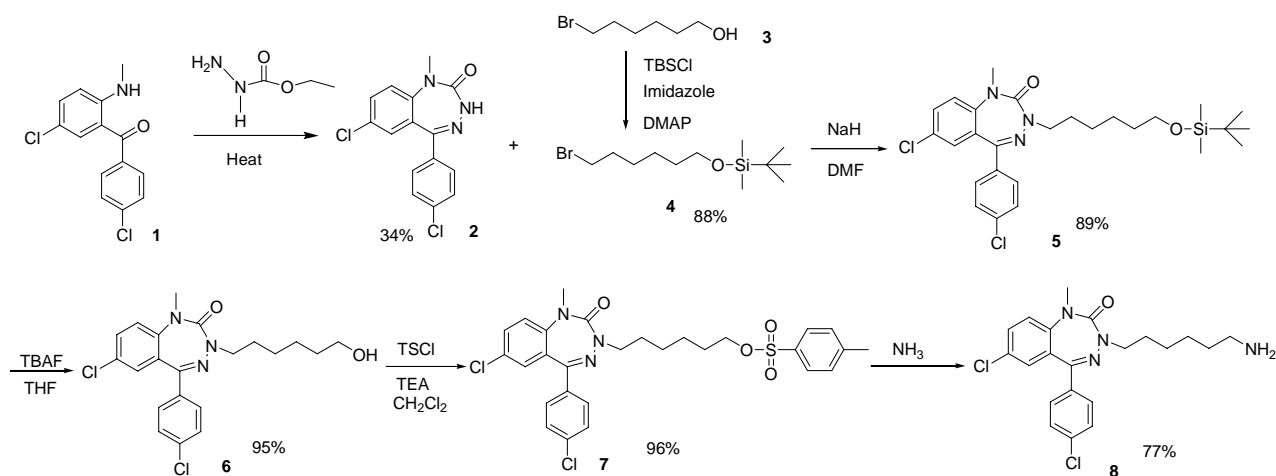
Scheme 3.1. Synthesis of C_6-Ro5-4864

The overall goal of this synthetic effort was to construct a conjugable TSPO ligand with a biologically active portion of Ro5-4864. (5-Chloro-2-(methylamino)phenyl)(4-chlorophenyl)methanone **1** was synthesized from commercially available 4-chlorophenylacetonitrile and 4-chloronitrobenzene as reported[13]. After several unsuccessful attempts using semicarbazide and high-boiling solvents to induce a ring-closure reaction with **1**, we synthesized the triazepinone **2** by heating a mixture of ethyl semicarbazide and **1** at

78

210 °C without any solvent(Scheme 3.1).. The *tert*-butyldimethylsilyl (TBS)-protected six-carbon linker **4** was added to **2** by an N-alkylation reaction. It is noteworthy that two other linkers, 1,3-dihydro-1,3-dioxo-2*H*-isoindole-2-hexanoic acid and 6-nitrohexanoic acid were also employed, but we were unsuccessful in achieving the final product. After the TBS group in **5** was removed via TBAF, the hydroxyl group in **6** was converted to a tosyl group and subsequently reacted with ammonia to yield the final product **8**.

Since the commercially available lissamine-rhodamine B sulfonyl chloride is a mixture of two isomers (Scheme 3.2), the N-sulfonylation reaction between C_6Ro5-4864 and the fluorescence dye produced two isomer products. It was possible to isolate these two products through silica gel column chromatograph (Rf is 0.23 for isomer I and 0.14 for isomer II in 4% methanol in dichloromethane). C_6Ro5-4864 is in para position in isomer I and ortho position in isomer II, verified by pH test[14]. Isomers I and II have a similar maximum absorption (isomer I: 561 nm; isomer II: 563 nM) and emission (isomer I: 583 nm; isomer II: 585 nm) wavelength to that of the free lissamine dye (Abs = 568 nm and Fluo = 583 nm) and Liss-ConPK11195 (Abs = 571 nm and Fluo = 585 nm) (Figure 3.1)[8]. However, the molar extinction coefficients of the produced isomers are significantly different (isomer I:
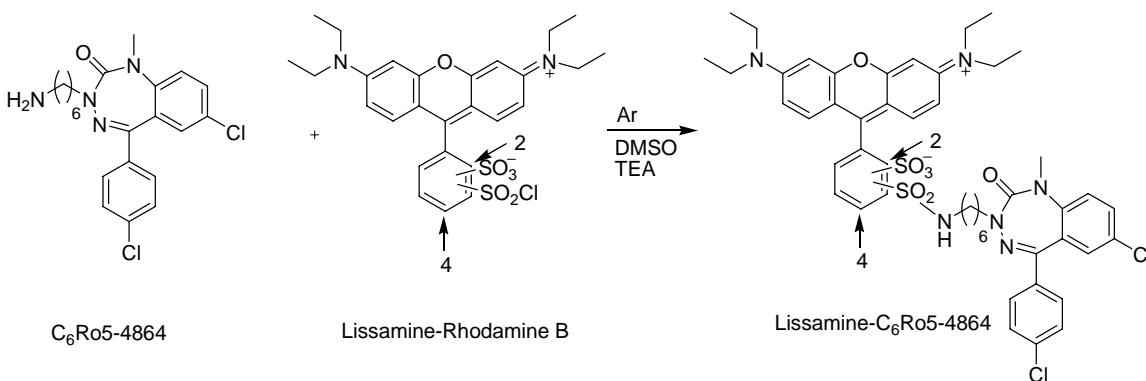
Scheme 3.2. Synthesis of lissamine-C_6Ro5-4864
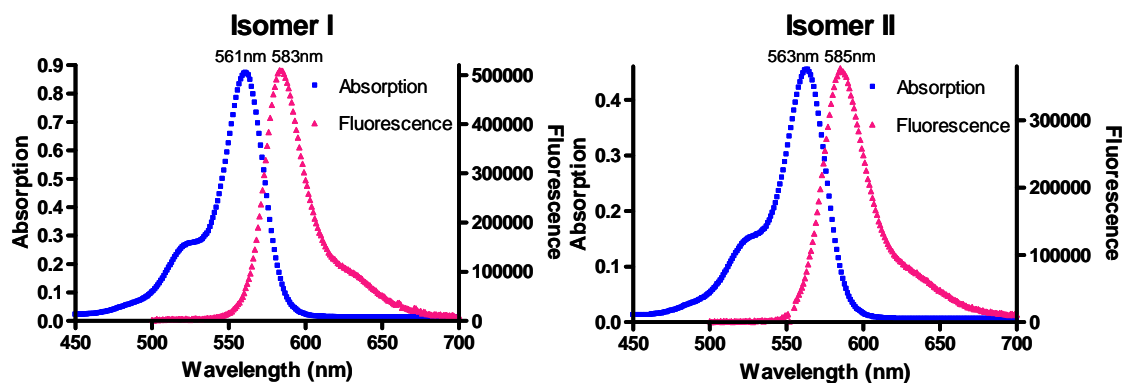
Figure 3.1. Lissamine-C_6Ro5-4864 isomer I (left, para) and isomer II (right, ortho) absorption and fluorescence curves.
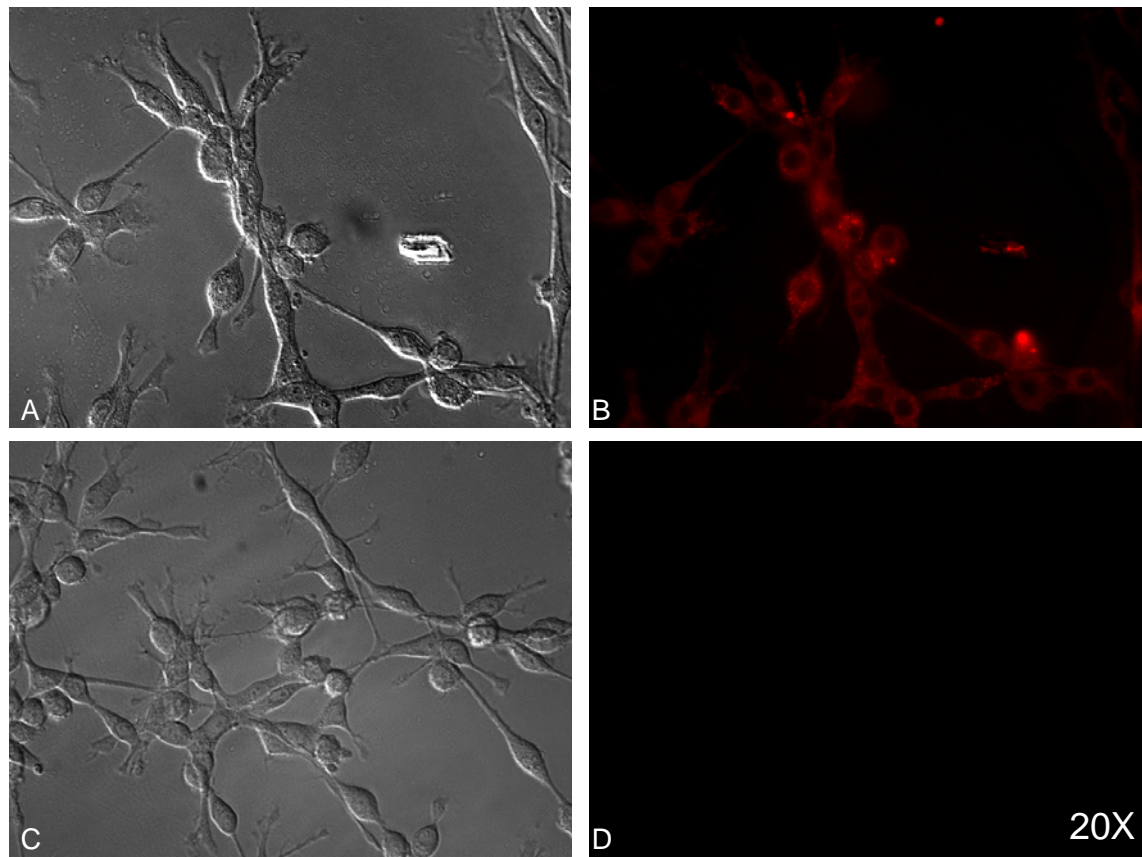
Figure 3.2. Fluorescence imaging of C6 rat glioma cells: (A) phase contrast microscopy of cells dosed with lissamine-C_6Ro5-4864; (B) fluorescence imaging of cells dosed with 100 nM lissamine-C_6Ro5-4864; (C) phase contrast microscopy of cells dosed with lissamine dye; (D) fluorescence imaging of cells dosed with 100 nM lissamine dye (control).
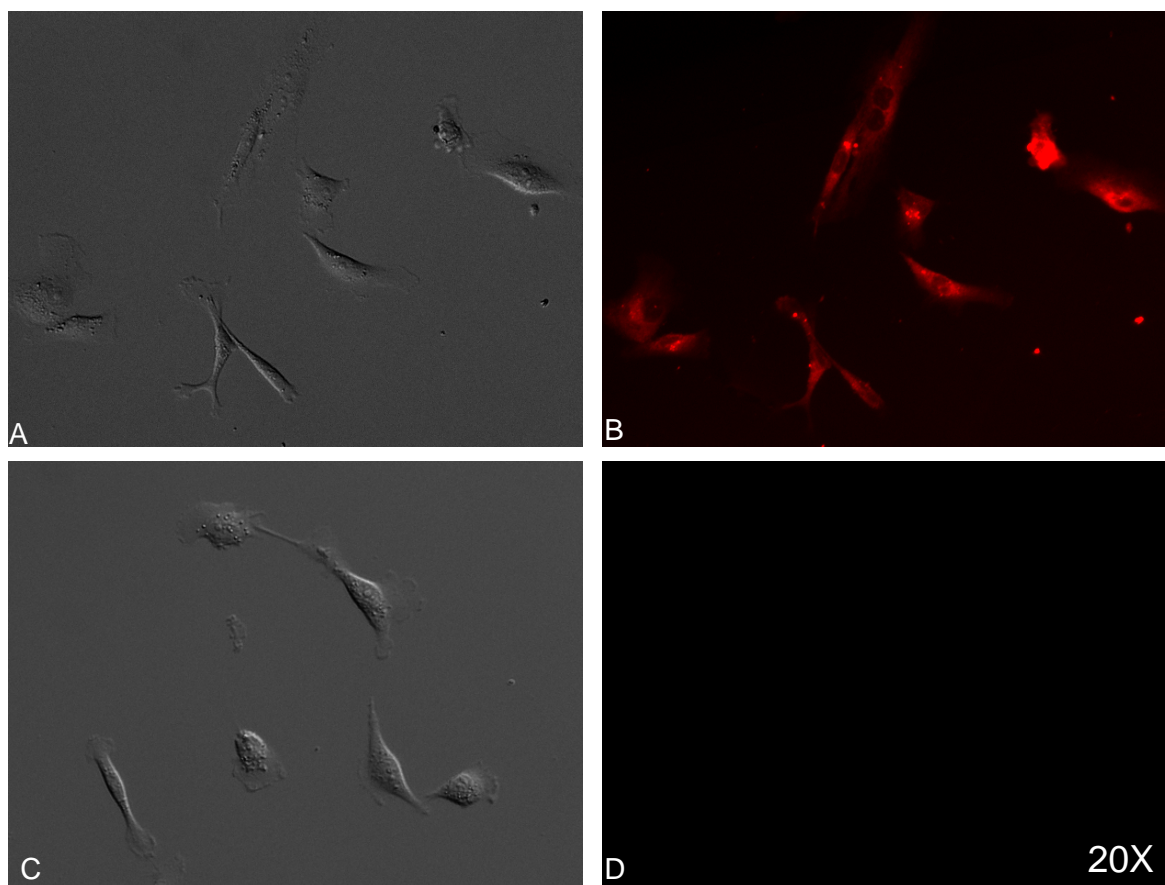
Figure 3.3. Fluorescence imaging of MDA-MB-231 human breast cancer cells: (A) Phase contrast microscopy of cells dosed with lissamine-C_6Ro5-4864; (B) fluorescence imaging of cells dosed with 100 nM lissamine-C_6Ro5-4864; (C) Phase contrast microscopy of cells dosed with lissamine dye; (D) fluorescence imaging of cells dosed with 100 nM lissamine dye (control).

175000 L/mol cm; isomer II: 91000 L/mol cm). Isomer I has much higher ε than lissamine-rhodamine B sulfonyl chloride (ε = 88000 L/mol cm), which indicates that C_6Ro5-4864 produces a positive effect on lissamine's absorptive property. The molar extinction coefficient of Liss-ConPK11195 was reported as 35000 L/mol cm, which is lower than both isomer I and isomer II. Isomer I was selected for imaging due to the relative high absorption and fluorescence (Figure 3.1).
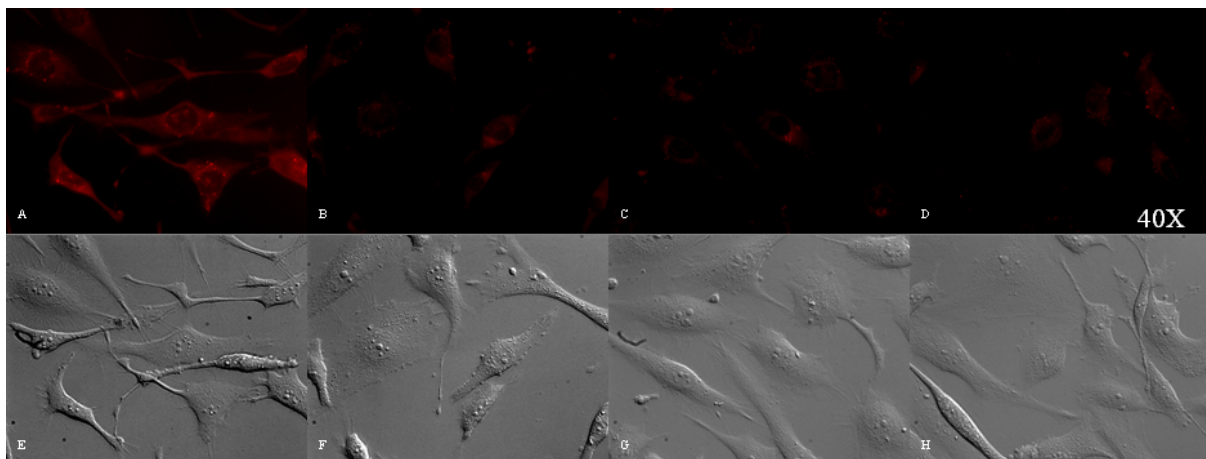
Figure 3.4. In vitro competition study using MDA-MB-231 human breast cancer cells: (A) fluorescence imaging of cells dosed with 5 µM lissamine-C_6Ro5-4864; (B) fluorescence imaging of cells dosed with 5 µM lissamine-C_6Ro5-4864 and 500 nM PK11195; (C) fluorescence imaging of cells dosed with 5 µM lissamine-C_6Ro5-4864 and 5 µM PK11195; (D) fluorescence imaging of cells dosed with 5 µM lissamine-C_6Ro5-4864 and 50 µM PK11195; (E-H) corresponding phase contrast microscopy.

3.3.2 Cell Imaging and Binding Study

The cellular uptake of lissamine-C_6Ro5-4864 was examined in C6 rat glioma and MDA-MB-231 human mammary adenocarcinoma cells by fluorescence microscopy. Both cell types were previously shown to contain relatively high levels of TSPO[15,16]. The resulting images were compared with those obtained using the same concentrations of the free lissamine dye as control. Cell uptake of lissamine-C_6Ro5-4864 was observed in fluorescence images of both cell lines (Figures 3.2 and 3.3, panel B) while the control exhibited no significant fluorescence. Images using Liss-ConPK11195 showed similar quality[8].

Radioligand binding studies further demonstrated specific binding of lissamine-C_6Ro5-4864 to the TSPO protein. In these studies, [^{3}H]PK11195, the well characterized diagnostic TSPO drug ligand, was used as the competitive radioligand. The concentration of lissamine-C_6Ro5-4864 tested varied from 10^{-11} M to 10^{-4} M in the competitive binding assays

82

performed. The K_i value derived from IC50 was calculated to be 2.6 ± 1.4 µM, which is similar to Liss-ConPK11195 (1 µM)[8]. Even though the binding affinity is significantly lower than that of [³H]Ro5-4864 ($K_i = 5$ nM)[17], the selective binding of lissamine-C_6Ro5-4864 to TSPO is clearly shown and visualized. The specificity of lissamine-C_6Ro5-4864 to TSPO is further verified by in vitro competition study. In this experiment, MDA-MB-231 cells were treated with 5 µM lissamine-C_6Ro5-4864 and PK11195 with different concentrations as competitor. Challenged cells showed reduced fluorescence signal compared to unchallenged cells (Figure 3.4). Taken together these data suggest that lissamine-C_6Ro5-4864 is a promising TSPO targeted MI agent.

3.4 Conclusions

We synthesized and characterized a conjugable form of the benzodiazepine Ro5-4864, C_6Ro5-4864, which can be conjugated to a variety of signaling moieties for TSPO-targeted imaging. This TSPO ligand has been coupled to a fluorescent dye, and the resulting imaging agent, lissamine-C_6Ro5-4864, displays attractive optical properties for fluorescence microscopy imaging. The specific binding of this agent to TSPO was demonstrated by radioligand binding studies and live cell imaging on MDA-MB-231 breast cancer and C6 glioma cells.

3.5 Acknowledgments

Bioconjugate Chemistry 2007, *18*, 1118-1122. The title is: "A Novel Conjugable Translocator Protein Ligand Labeled with a Fluorescence Dye for in Vitro Imaging". The authors are: Mingfeng Bai, Shelby Wyatt, Zeqiu Han, Vassilios Papadopoulos, and Darryl J. Bornhop.

3.6 References

(1)   Papadopoulos, V.; Baraldi, M.; Guilarte, T. R.; Knudsen, T. B.; Lacapere, J. J. et al. Translocator protein (18 kDa): new nomenclature for the peripheral-type benzodiazepine receptor based on its structure and molecular function. *Trends in Pharmacological Sciences* **2006**, *27*, 402-409.

(2)   Casellas, P.; Galiegue, S.; Basile, A. S. Peripheral benzodiazepine receptors and mitochondrial function. *Neurochemistry International* **2002**, *40*, 475-486.

(3)   Taketani, S.; Kohno, H.; Furukawa, T.; Tokunaga, R. Involvement of Peripheral-Type Benzodiazepine Receptors in the Intracellular-Transport of Heme and Porphyrins. *Journal of Biochemistry* **1995**, *117*, 875-880.

(4)   Decaudin, D.; Castedo, M.; Nemati, F.; Beurdeley-Thomas, A.; De Pinieux, G. et al. Peripheral benzodiazepine receptor ligands reverse apoptosis resistance of cancer cells in vitro and in vivo. *Cancer Research* **2002**, *62*, 1388-1393.

(5)   Kozikowski, A. P.; Kotoula, M.; Ma, D. W.; Boujrad, N.; Tuckmantel, W. et al. Synthesis and biology of a 7-nitro-2,1,3-benzoxadiazol-4-yl derivative of 2-phenylindole-3-acetamide: A fluorescent probe for the peripheral-type benzodiazepine receptor. *Journal of Medicinal Chemistry* **1997**, *40*, 2435-2439.

(6)   Shilova, N. V.; Bovin, N. V. Fluorescent labels for the analysis of mono- and oligosaccharides. *Russian Journal of Bioorganic Chemistry* **2003**, *29*, 309-324.

(7)   Manning, H. C.; Goebel, T.; Marx, J. N.; Bornhop, D. J. Facile, efficient conjugation of a trifunctional lanthanide chelate to a peripheral benzodiazepine receptor ligand. *Organic Letters* **2002**, *4*, 1075-1078.

(8)   Manning, H. C.; Smith, S. M.; Sexton, M.; Haviland, S.; Bai, M. F. et al. A peripheral benzodiazepine receptor targeted agent for in vitro imaging and screening. *Bioconjugate Chemistry* **2006**, *17*, 735-740.

(9)   Farges, R. C.; Torres, S. R.; Ferrara, P.; Ribeiro-Do-Valle, R. M. Involvement of steroids in anti-inflammatory effects of peripheral benzodiazepine receptor ligands. *Life Sciences* **2004**, *74*, 1387-1395.

(10)   Gavioli, E. C.; Duarte, F. S.; Bressan, E.; Ferrara, P.; Farges, R. C. et al. Antidepressant-like effect of Ro5-4864, a peripheral-type benzodiazepine receptor ligand, in forced swimming test. *European Journal of Pharmacology* **2003**, *471*, 21-26.

(11)   DalBo, S.; Nardi, G. M.; Ferrara, P.; Ribeiro-do-Valle, R.; Farges, R. C. Antinociceptive effects of peripheral benzodiazepine receptors. *Pharmacology* **2004**, *70*, 188-194.

(12)   Garnier, M.; Dimchev, A. B.; Boujrad, N.; Price, J. M.; Musto, N. A. et al. In-Vitro Reconstitution of a Functional Peripheral-Type Benzodiazepine Receptor from Mouse Leydig Tumor-Cells. *Molecular Pharmacology* **1994**, *45*, 201-211.

(13)   Vejdelek, Z.; Polivka, Z.; Protiva, M. Synthesis of 7-Chloro-5-(4-Chlorophenyl)-1-Methyl-1,3-Dihydro-1,4-Benzodiazepin-2-One. *Collection of Czechoslovak Chemical Communications* **1985**, *50*, 1064-1069.

(14)   Corrie, J. E. T.; Davis, C. T.; Eccleston, J. F. Chemistry of sulforhodamine-amine conjugates. *Bioconjugate Chemistry* **2001**, *12*, 186-194.

(15)   Papadopoulos, V.; Guarneri, P.; Krueger, K. E.; Guidotti, A.; Costa, E. Pregnenolone Biosynthesis in C6-2b Glioma Cell Mitochondria - Regulation by a Mitochondrial Diazepam Binding Inhibitor Receptor. *Proceedings of the National Academy of Sciences of the United States of America* **1992**, *89*, 5113-5117.

(16)   Hardwick, M.; Fertikh, D.; Culty, M.; Li, H.; Vidic, B. et al. Peripheral-type benzodiazepine receptor (PBR) in human breast cancer: Correlation of breast cancer cell aggressive phenotype with PBR expression, nuclear localization, and PBR-mediated cell proliferation and nuclear transport of cholesterol. *Cancer Research* **1999**, *59*, 831-842.

(17)   Boujrad, N.; Gaillard, J. L.; Garnier, M.; Papadopoulos, V. Acute Action of Choriogonadotropin on Leydig Tumor-Cells - Induction of a Higher Affinity Benzodiazepine-Binding Site Related to Steroid-Biosynthesis. *Endocrinology* **1994**, *135*, 1576-1583.

A NOVEL FUNCTIONAL TRANSLOCATOR PROTEIN LIGAND FOR DISEASE
IMAGING AND STEM CELL TRACKING

4.1 Introduction

The 18 kDa translocator protein (TSPO), also known as the peripheral-type benzodiazepine receptor (PBR), has become an attractive target for cancer[1-3] and neurodegenerative disease imaging[4-6]. Over-expression of TSPO has been observed in a variety of cancers, including brain, breast, colorectal, prostate and ovarian cancers, astrocytomas and hepatocellular and endometrial carcinomas[7]. TSPO is also associated with a number of biological processes, such as cell proliferation, apoptosis, steroidogenesis, and immunomodulation, however, its exact physiological role still is not clear.

Several TSPO-selective ligands have been developed, including the diazepam derivative (Ro5-4864), the isoquinoline derivative (PK11195), the 2-acryl-3-indoleacetamide derivative (FGIN-1), and the phenoxyphenyl-acetamide derivative (DAA1106)[8,9]. DAA1106 (Figure 4.1) has become an attractive TSPO ligand. It has higher binding affinity for TSPO than PK11195, Ro5-4864, and FGIN1. DAA1106 has been shown to displace TSPO-complexed PK11195 and Ro5-4864 at a very
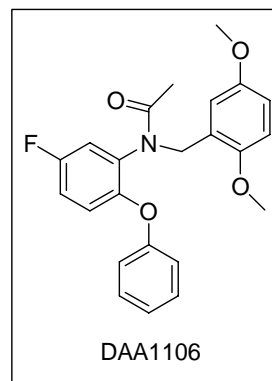
DAA1106

Figure 4.1. Structure of DAA1106

low concentration (10^{-15}–10^{-12} M), however, 0.1-1 µM amounts of PK11195, Ro5-4864 or FGIN1 were necessary to displace DAA1106[10]. Although promising, TSPO studies using DAA1106 have been limited due to the fact that the molecule is not easily functionalized.

A conjugable analog of DAA1106, which can be coupled to a variety of signaling moieties, would be a valuable tool for studying TSPO function. Even though DAA1106 labeled with ^{11}C, ^{3}H and ^{18}F have been used to study TSPO activity, these labels are limited by their short half-lives[11-13]. In addition, positron emission tomography (PET) has very low resolution (4-5 mm)[14]. Furthermore, biological studies using tritium are cumbersome, expensive, time consuming and create radioactive waste. A conjugable version of PK11195 was developed previously and labeled with a fluorescent dye[15,16]. Unfortunately, the binding affinity of the imaging agent was rather low (1 µM).

In this part of research, conjugable analogues of DAA1106, n-TSPOmbb732 (n is the number of carbon on the linker) were synthesized and characterized. The analogue has a terminal amino group that facilitates coupling reactions. The binding affinities and yields of seven n-TSPOmbb732 (n=3-9) molecules were compared. The 6-TSPOmbb732 was determined as the version with the highest affinity in cell homogenate. Signaling moieties, including three fluorescent dyes and three lanthanide chelates, were coupled to 6-TSPOmbb732 for optical, PET and multi-modality imaging. The fluorescent dyes coupled to 6-TSPOmbb732 include IRDye^{TM} 800CW NHS ester (LI-COR Biosciences, ε = 300000 L/mol cm in methanol), lissamine^{TM} rhodamine B sulphonyl chloride (Invitrogen, ε = 88000 L/mol cm in methanol) and cypate[17,18] (ε = 224000 L/mol cm in 20% DMSO/H_2O). The resulting optical imaging agents have nanomolar binding

affinities to TSPO and target TSPO in vitro. 6-TSPOmbb732 was also labeled with two trifunctional lanthanide chelators for multi-modality imaging. One agent has a methyl quinoline antenna, whereas the other one uses coumarin as the antenna. Finally, a cyclen (1,4,7,10-tetraazacyclododecane) macrocycle based agent, ^{64}Cu-DOTA-6-TSPOmbb732, was synthesized. The prospect of this agent in TSPO targeted PET imaging will be considered.

Several 6-TSPOmbb732 based imaging agents have been investigated in TSPO targeted cancer cell imaging. MDA-MB-231 mammary adenocarcinoma breast cancer cells or C6 rat glioma cells were treated with IRDye^{TM} 800CW-6-TSPOmbb732 (NIR6T), lissamine^{TM}-6-TSPOmbb732 (Liss6T) and MitoTracker Green (a mitochondrial marker). Co-localization of these molecules was studied to analyze the specific targeting. Moreover, fluorescence images of cancer cells dosed with NIR6T or Liss6T and the images of cells dosed with corresponding free dye were compared. In addition, a relatively inexpensive and stable NIR dye, cypate, was coupled to 6-TSPOmbb732. Cypate-6-TSPOmbb732 (Cypate6T) was used to image MDA-MB-231 cells.

Even though our TSPO targeted imaging has been focused on studying cancers and other diseases[1,19,20], preliminary results presented in this chapter suggest that stem cell tracking will probably become another attractive area for TSPO targeted investigations. Transplantation of stem cells into damaged tissue is a promising strategy for the treatment of a number of disorders, such as Parkinson's disease, Alzheimer's disease, and myocardial infarction[21]. However, the specific contribution of these stem cells toward therapy is not well understood because fate, function, and movement of these cells has not been well defined[22]. Since stem cells do not have any internal

signaling moieties, they cannot be imaged directly with available imaging techniques. The use of imaging agents is thus necessary.

Many contrast agents for stem cell tracking have been developed, such as Gd-DTPA (T1 MRI agent,)[23,24], gadolinium rhodamine dextran(GRID, bifunctional MRI/opcial agent)[25-27], 18FHBG[28], superparamagnetic iron oxide nanoparticles (SPIO, T2 MRI agents)[29-31] and microbubbles (ultrasound)[32]. Unfortunately, there are still many unanswered questions. These include the destiny of the injected cells, what procedure gives desired outcome, and what the long-term impact of stem cell therapy is[33].

Receptor targeted stem cell imaging agents would be favorable alternative to non-specific cell labeling and could possibly label stem cells for a longer period of time. Specific receptor-ligand binding may keep imaging agents from being cleared out of cells. Recently, TSPO expression in stem cells and effects of TSPO ligands on proliferation and differentiation of these cells were studied[34]. These studies suggest that TSPO is potentially a promising target for stem cell imaging. Due to these facts, three TSPO targeted optical imaging agents, NIR6T, Liss6T and LissRo5 (refer to Chapter 3) were used to label bone marrow mononuclear cells (MNC), embryonic epithelial progenitor cells (eEPC) and embryonic stem cells (ESC). Preliminary in vitro images indicate that these agents are able to track these stem cells for at least a day. Significant fluorescence signal was observed from MNC cells labeled with NIR6T three weeks after treatment. This indicates that TSPO targeted imaging agents can be potentially used to follow transplanted stem cells.

4.2 Experimental Procedures

4.2.1 Synthesis

N-(2-Bromo-5-methoxybenzyl)-N-(5-fluro-2-phenoxphenyl)acetamide (2). To a dry round bottom flask, was added anhydrous DMF (10 mL) and sodium hydride (100 mg), followed by N-(5-fluoro-2-phenoxyphenyl)acetamide **1** (1.08 g, 4.4 mmol). After the solution was stirred for 15 min, 2-bromo-5-methoxy-benzyl bromide (1.4 g, 5.0 mmol) was added. After another 30 min, the reaction was added to stirring water chilled to 0°C (60 mL). The mixture was extracted with dichloromethane three times. The organic solutions were combined, dried over Mg_2SO_4 and evaporated to dryness. The residue was chromatographed (silica gel) using 1:3 ethyl acetate/hexanes as the eluent to yield compound **2** as a yellow oil (1.94 g, 99%). ^{1}H NMR 300 MHz ($CDCl_3$) δ 7.29-7.33 (m, 3H), 7.12 (t, J=7.6 Hz, 1H), 7.02 (d, J=3.2 Hz, 1H), 6.80-6.96 (m, 5H), 6.62 (dd, J=8.4, 2.8 Hz, 1H), 4.96 (AX, J=15.2 Hz, Δv=178 Hz, 2H), 3.66 (s, 3H), 2.00 (s, 3H). MS (ESI)$^+$ [M+H]$^+$ calcd 444.1, found 444.3.

General method for n-TSPOmbb732 (3) synthesis. Pd[P(t-Bu)$_3$]$_2$ (102 mg, 0.2 mmol), cetyltrimethylammonium bromide (36 mg, 0.1 mmol), potassium hydroxide (842 mg, 15 mmol) and diamine (30 mmol) were mixed in toluene (4 mL) under argon. **2** (4.44 g, 10 mmol) in toluene (6 mL) and water (270 μL, 15 mmol) were added to the mixture by syringe. The flask was sealed with a septum and the reaction mixture was stirred vigorously at 90°C for 6 h. The reaction then was concentrated by vacuum and purified by column chromatography using 9:1:0.1 $CH_2Cl_2/CH_3OH/NH_3 \cdot H_2O$ on silica gel to yield n-TSPOmbb732 as a colorless oil.

3-TSPOmbb732 (Y=8.7%). NMR data is not shown because diastereomers could not be separated. MS (ESI)$^+$ [M+H]$^+$ calcd 438.2, found 438.2.

4-TSPOmbb732 (Y=7.9%). NMR data is not shown because diastereomers could not be separated. MS (ESI)$^+$ [M+H]$^+$ calcd 452.2, found 452.3.

5-TSPOmbb732 (Y=10%). ^{1}H NMR 400 MHz (CDCl$_3$) δ 7.27 (t, *J*=8.4 Hz, 2H), 7.09 (t, *J*=7.6 Hz, 1H), 6.91-6.96 (m, 1H), 6.79-6.83 (m, 1H), 6.69-6.75 (m, 4H), 6.39 (d, *J*=8.8 Hz, 1H), 6.19 (d, *J*=2.8 Hz, 1H), 4.75 (AX, *J*=9.6 Hz, Δv=79.2 Hz, 2H), 3.60 (s, 3H), 2.86-3.03 (m, 2H), 2.77 (t, *J*=5.1 Hz, 2H), 1.94 (s, 5H), 1.50-1.62 (m, 2H), 1.40-1.45 (m, 5H). MS (ESI)$^+$ [M+H]$^+$ calcd 466.3, found 466.3.

6-TSPOmbb732 (Y=33%). ^{1}H NMR 300 MHz (CDCl$_3$) δ 7.28 (t, *J*=8.1 Hz, 2H), 7.10 (t, *J*=7.5 Hz, 1H), 6.91-6.95 (m, 1H), 6.79-6.84 (m, 1H), 6.70-6.75 (m, 4H), 6.40 (d, *J*=8.7 Hz, 1H), 6.20 (d, *J*=3.0 Hz, 1H), 4.76 (AX, *J*=14.7 Hz, Δv=95.1 Hz, 2H), 3.61 (s, 3H), 2.87-3.03 (m, 2H), 2.66 (t, *J*=6.9 Hz, 2H), 1.94 (s, 3H), 1.54-1.61 (m, 2H), 1.28-0.48 (m, 9H). MS (ESI)$^+$ [M+H]$^+$ calcd 480.3, found 480.2.

7-TSPOmbb732 (Y=12%). ^{1}H NMR 300 MHz (CDCl$_3$) δ 7.28 (t, *J*=7.5 Hz, 2H), 7.10 (t, *J*=7.5 Hz, 1H), 6.91-6.98 (m, 1H), 6.80-6.85 (m, 1H), 6.70-6.75 (m, 4H), 6.41 (d, *J*=9.0 Hz, 1H), 6.20 (d, *J*=3.0 Hz, 1H), 4.76 (AX, *J*=14.7 Hz, Δv=103.2 Hz, 2H), 3.60 (s, 3H), 2.84-3.06 (m, 2H), 2.68 (t, *J*=7.2 Hz, 2H), 1.94 (s, 3H), 1.53-1.60 (m, 2H), 1.31-1.46(m, 11H). MS (ESI)$^+$ [M+H]$^+$ calcd 494.3, found 494.3.

8-TSPOmbb732 (Y=5.8%). ^{1}H NMR 400MHz (CDCl$_3$) δ 7.28 (t, *J*=8.4 Hz, 2H), 7.10 (t, *J*=7.6 Hz, 1H), 6.92-6.97 (m, 1H), 6.81-6.84 (m, 1H), 6.71-6.74 (m, 4H), 6.41 (d, *J*=8.8 Hz, 1H), 6.20 (d, *J*=2.8 Hz, 1H), 4.76 (AX, *J*=14.4 Hz, Δv=140.4 Hz, 2H), 3.60 (s,

3H), 2.85-3.04 (m, 2H), 2.72 (t, *J*=7.2 Hz, 2H), 1.94 (s, 3H), 1.44-1.59 (m, 6H), 1.30-1.37(m, 9H). MS (ESI)$^+$ [M+H]$^+$ calcd 508.3, found 508.3.

9-TSPOmbb732 (Y=11%). ^{1}H NMR 300 MHz (CDCl$_3$) δ 7.29 (t, *J*=7.5 Hz, 2H), 7.10 (t, *J*=7.5 Hz, 1H), 6.92-6.97 (m, 1H), 6.80-6.85 (m, 1H), 6.71-6.75 (m, 4H), 6.41 (d, *J*=9.0 Hz, 1H), 6.20 (d, *J*=3.0 Hz, 1H), 4.76 (AX, *J*=14.4 Hz, Δ*v*=105.3 Hz, 2H), 3.61 (s, 3H), 2.84-3.06 (m, 2H), 2.72 (t, *J*=6.9 Hz, 2H), 2.51 (s, 2H), 1.94 (s, 3H), 1.45-1.62 (m, 5H), 1.19-1.36(m, 10H). MS (ESI)$^+$ [M+H]$^+$ calcd 522.3, found 522.3.

General method for n-TSPOmbb732 amide (4) synthesis. A mixture of acetic acid (1.6 μL, 27.5 μmol), triethylamine (TEA) (50 μL) and 2-succinimido-1,1,3,3,-tetramethyluronium tetrafluoroborate (TSTU) (8.3 mg, 27.5 μmol) in dry dichloromethane (1 mL) was stirred at room temperature under argon for 3 h. A solution of **3** (25 μmol) in anhydrous dichloromethane (1 mL) was added to the mixture and was stirred for another 2.5 h. The reaction solution then was concentrated by vacuum rotary evaporation and the product was purified via silica gel column chromatography using 3% methanol in dichloromethane as eluent. n-TSPOmbb732 amide was collected as a colorless oil.

3-TSPOmbb732 Amide. ^{1}H NMR 300 MHz (CDCl$_3$) δ 7.27 (t, *J*=7.5 Hz, 2H), 7.10 (t, *J*=7.2 Hz, 1H), 6.71-6.84 (m, 3H), 6.63 (d, *J*=7.5 Hz, 2H), 6.40 (d, *J*=8.7 Hz, 1H), 6.19 (d, *J*=2.7 Hz, 1H), 6.04 (br s, 1H), 5.12 (br s, 1H), 4.77 (AX, *J*=14.4 Hz, Δ*v*=36.9 Hz, 2H), 3.61 (s, 3H), 3.29 (q, *J*=6.3 Hz, 2H), 2. 94-3.13 (m, 2H), 1.97 (br s, 6H), 1.75-1.79 (m, 2H), 1.67 (br s, 1H). MS (ESI)$^+$ [M+Na]$^+$ calcd 502.2, found 502.1.

4-TSPOmbb732 Amide. ^{1}H NMR 300 MHz (CDCl$_3$) δ 7.27 (t, *J*=7.5 Hz, 2H), 7.10 (t, *J*=7.2 Hz, 1H), 6.92-6.99 (m, 1H), 6.65-6.84 (m, 5H), 6.56 (br s, 1H), 6.34 (d,

J=8.7 Hz, 1H), 6.20 (d, J=3.0 Hz, 1H), 4.78 (AX, J=14.7 Hz, Δv=36.0 Hz, 2H), 3.61 (s, 3H), 3.28 (m, 2H), 2.81-3.05 (m, 2H), 2.01 (s, 3H), 1.96 (s, 3H), 1.63-1.68 (m, 5H). MS (ESI)$^+$ [M+H]$^+$ calcd 494.2, found 494.2.

5-TSPOmbb732 Amide. ^{1}H NMR 300 MHz (CDCl$_3$) δ 7.28 (t, J=7.5 Hz, 2H), 7.10 (t, J=7.5 Hz, 1H), 6.92-6.99 (m, 1H), 6.80-6.85 (m, 1H), 6.68-6.76 (m, 4H), 6.47 (br s, 1H), 6.39 (d, J=8.7 Hz, 1H), 6.20 (d, J=3.0 Hz, 1H), 4.81 (br s, 1H), 4.78 (AX, J=14.4 Hz, Δv=73.5 Hz, 2H), 3.61 (s, 3H), 3.28 (q, J=6.0 Hz, 2H), 2.82-3.08 (m, 2H), 1.95 (s, 3H), 1.95 (s, 3H), 1.44-1.65 (m, 6H). MS (ESI)$^+$ [M+H]$^+$ calcd 508.3, found 508.2.

6-TSPOmbb732 Amide. ^{1}H NMR 400 MHz (CDCl$_3$) δ 7.28 (t, J=7.6 Hz, 2H), 7.10 (t, J=7.2 Hz, 1H), 6.92-6.97 (m, 1H), 6.80-6.84 (m, 1H), 6.70-6.75 (m, 4H), 6.40 (d, J=8.8 Hz, 1H), 6.19 (d, J=2.8 Hz, 1H), 5.90 (br s, 1H), 4.87 (br s, 1H), 4.76 (AX, J=14.4 Hz, Δv=114.0 Hz, 2H), 3.60 (s, 3H), 3.24 (q, J=6.0 Hz, 2H), 2.86-3.06 (m, 2H), 1.97 (s, 3H), 1.94 (s, 3H), 1.48-1.59 (m, 4H), 1.33-1.41 (m, 4H). MS (ESI)$^+$ [M+H]$^+$ calcd 522.3, found 522.2.

7-TSPOmbb732 Amide. ^{1}H NMR 300 MHz (CDCl$_3$) δ 7.28 (t, J=7.5 Hz, 2H), 7.10 (t, J=7.2 Hz, 1H), 6.92-6.98 (m, 1H), 6.80-6.85 (m, 1H), 6.70-6.75 (m, 4H), 6.40 (d, J=8.7 Hz, 1H), 6.19 (d, J=2.7 Hz, 1H), 5.64 (br s, 1H), 4.87 (br s, 1H), 4.76 (AX, J=14.4 Hz, Δv=100.2 Hz, 2H), 3.60 (s, 3H), 3.23 (q, J=6.0 Hz, 2H), 2.86-3.03 (m, 2H), 1.96 (s, 3H), 1.94 (s, 3H), 1.45-1.60 (m, 4H), 1.31-1.36 (m, 6H). MS (ESI)$^+$ [M+H]$^+$ calcd 536.3, found 536.4.

8-TSPOmbb732 Amide. ^{1}H NMR 300 MHz (CDCl$_3$) δ 7.29 (t, J=7.5 Hz, 2H), 7.10 (t, J=7.2 Hz, 1H), 6.91-6.98 (m, 1H), 6.80-6.85 (m, 1H), 6.70-6.74 (m, 4H), 6.41 (d, J=8.7 Hz, 1H), 6.20 (d, J=3.0 Hz, 1H), 5.60 (br s, 1H), 4.86 (br s, 1H), 4.76 (AX, J=14.4

Hz, Δν=113.1 Hz, 2H), 3.61 (s, 3H), 3.23 (q, *J*=6.0 Hz, 2H), 2.84-3.06 (m, 2H), 1.96 (s, 3H), 1.94 (s, 3H), 1.46-1.59 (m, 4H), 1.31-1.37 (m, 8H). MS (ESI)$^+$ [M+H]$^+$ calcd 550.3, found 550.5.

9-TSPOmbb732 Amide. ^{1}H NMR 300 MHz (CDCl$_3$) δ 7.29 (t, *J*=7.5 Hz, 2H), 7.10 (t, *J*=7.2 Hz, 1H), 6.91-6.98 (m, 1H), 6.80-6.85 (m, 1H), 6.70-6.74 (m, 4H), 6.41 (d, *J*=9.0 Hz, 1H), 6.20 (d, *J*=3.0 Hz, 1H), 5.31 (br s, 1H), 4.86 (br s, 1H), 4.76 (AX, *J*=14.4 Hz, Δν=110.1 Hz, 2H), 3.61 (s, 3H), 3.23 (q, *J*=6.0 Hz, 2H), 2.84-3.05 (m, 2H), 1.97 (s, 3H), 1.94 (s, 3H), 1.46-1.59 (m, 4H), 1.31-1.37 (m, 10H). MS (ESI)$^+$ [M+H]$^+$ calcd 564.3, found 564.5.

IRDye^{TM} 800CW-6-TSPOmbb732 (NIR6T). IRDye^{TM} 800CW NHS ester (3 mg, 2.6 μmol) and 6-TSPOmbb732 (3 mg, 6.3 μmol) were mixed in DMSO (7 mL) in a round bottom flask and stirred under argon flow for 1 h. HPLC analysis was performed on a Varian Polaris C-18 column (250 × 4.6 mm) at a flow rate of 0.8 mL/min. Flow A was 0.1% TEA in water and flow B was 0.1% TEA in acetonitrile. The elution method for analytical HPLC started with a linear gradient from 100% to 70% A over 20 min, continued to 50% A over 5 min, arrived at 20% A in another 10 min, held at 20% A for 3 min, and finally returned to 100% A over 1 min. The elution profile was monitored by UV absorbance at 254 and 780 nm. The product was purified by preparative HPLC using a Varian Polaris C-18 column (250 × 21.2 mm) at 12 mL/min. The collected solution was concentrated by vacuum rotary evaporation, frozen to -78ºC and dried using a freeze-dry system. NIR6T was collected as a dark green solid (1.2 mg, 31%). ^{1}H NMR 500 MHz (MeOD) δ 7.99-7.91 (m, 3H), 7.86-7.78 (m, 6H), 7.34 (d, *J*=8.0 Hz, 1H), 7.27-7.23 (m, 3H), 7.17 (d, *J*=8.5 Hz, 1H), 7.10-7.01 (m, 3H), 6.77-6.74 (m, 1H), 6.70 (dd, *J*=9.0, 3.0

Hz, 1H), 6.59 (d, *J*=8.5 Hz, 2H), 6.42 (d, *J*=9.0 Hz, 1H), 6.26 (d, *J*=14.0 Hz, 1H), 6.20 (d, *J*=3.0 Hz, 1H), 6.15 (d, *J*=14.0 Hz, 1H), 4.96 (d, *J*=14.5 Hz, 1H), 4.60 (d, *J*=14.5 Hz, 1H), 4.15-4.10 (m, 2H), 4.08-4.05 (m, 2H), 3.52 (s, 3H), 3.43-3.39 (m, 2H), 3.14-3.11 (m, 2H), 3.04-2.93 (m, 2H), 2.89-2.86 (m, 2H), 2.82-2.72 (m, 5H), 2.17 (t, *J*=7.0 Hz, 2H), 2.05-2.02(m, 2H), 1.96-1.91 (m, 8H), 1.79-1.76 (m, 3H), 1.68-1.63 (m, 3H), 1.53-1.41 (m, 6H), 1.37 (d, *J*=4.0 Hz, 12H). MS (ESI)$^+$ [M+H]$^+$ calcd 1464.4, found 1464.5.

Lissamine^{TM}-6-TSPOmbb732 (Liss6T). A mixture of lissamine^{TM} rhodamine B sulphonyl chloride (10 mg, 17 μmol), 6-TSPOmbb732 (10 mg, 20 μmol) and triethylamine (15 μL) in dichloromethane (1.6 mL) was stirred under argon at room temperature for 1 h. The reaction solution was concentrated by vacuum rotary evaporation and the crude product was purified through column chromatography (silica gel) using a 19:1 dichloromethane:methanol solution to yield Liss6T as a pink solid. (Isomer I, 5.7 mg, 32%; Isomer II, 4.7 mg, 27%). ^{1}H NMR 400 MHz (CDCl$_3$) Isomer I: δ 8.84 (s, 1H), 7.98 (d, *J*=7.6 Hz, 1H), 7.30-7.24 (m, 3H), 7.19 (d, *J*=7.6 Hz, 1H), 7.08 (t, *J*=7.2 Hz, 1H), 6.93-6.90 (m, 2H), 6.78 (t, *J*=8.8 Hz, 3H), 6.70 (dd, *J*=8.4, 2.0 Hz, 1H), 6.66-6.63 (m, 3H), 6.37 (d, *J*=8.4 Hz, 1H), 6.19 (s, 1H), 5.61 (t, *J*=5.2 Hz, 1H), 4.78 (d, *J*=6.4 Hz, 1H), 3.59 (s, 3H), 3.56-3.45 (m, 7H), 3.10 (q, *J*=6.4 Hz, 2H), 3.02-2.96 (m, 1H), 2.87-2.81 (m, 1H), 2.01 (s, 2H), 1.72-1.50 (m, 12H), 1.44-1.37 (m, 4H), 1.29-1.25 (m, 10H). Isomer II: δ 8.72 (s, 1H), 8.36 (d, *J*=7.2 Hz, 1H), 7.27-7.18 (m, 5H), 7.08 (t, *J*=7.6 Hz, 1H), 6.95-6.89 (m, 2H), 6.87-6.85 (m, 3H), 6.79-6.76 (m, 1H), 6.71 (d, *J*=2.4 Hz, 2H), 6.65 (d, *J*=8.0 Hz, 2H), 6.20 (d, *J*=2.8 Hz, 1H), 6.05-6.00 (m, 1H), 4.77 (s, 2H), 3.62-3.56 (m, 11H), 3.32-3.27 (m, 1H), 3.02-2.96 (m, 1H), 2.96-2.91 (m, 3H), 2.85-2.79 (m, 2H), 1.95 (s, 3H), 1.52-1.42 (m, 4H), 1.32 (t, *J*=7.2 Hz, 12H), 1.15-1.11 (m, 3H). MS

(ESI)$^+$ [M+H]$^+$ calcd 1020.4, found 1020.4. Rf 0.39 (Isomer I), 0.32 (Isomer II) (6% methanol in dichloromethane).

Cypate-6-TSPOmbb732 (Cypate6T). A mixture of cypate (6.3 mg, 10 μmol), 2-(1H-Benzotriazole-1-yl)-1,1,3,3-tetramethyl uronium hexafluorophosphate (HBTU) (4.0 mg, 11 μmol) and 1-Hydroxybenzotriazole (HOBT) (1.3 mg, 10 μmol) in 0.6 mL 50:50 DMF/Dichloromethane was stirred at room temperature for 5 min. The above mixture was treated with diisopropylethylamine (DIEA) (2.5 μL) and stirred for another 10 min. 6-TSPOmbb732 (5.7 mg, 12 μmol) in 0.4 mL 50:50 DMF/dichloromethane solution was added to the above mixture and the reaction solution was stirred for 4 h and then neutralized by 0.1 M HCl solution. The mixture was concentrated by vacuum and product was purified by semi-preparative C18 HPLC column. Flow A was 0.1% TFA in water and flow B was 0.1% TFA in acetonitrile. Gradient elution method was 50% to 90% B in 84 min with 10 mL/min flow rate. Cypate-C$_6$DAA1106 was collected as a green solid (2.8 mg, 26%). MS (ESI)$^+$ [M+H]$^+$ calcd 1086.6, found 1087.0.

2-(4,10-Bis(benzyloxycarbonyl)-7-((6-methylquinolin-2-yl)methyl)-1,4,7,10-tetraazacyclododecan-1-yl)acetic acid (6). Compound **5** was synthesized as preciously reported[35]. A 7 M KOH solution was added slowly to a stirring solution of bromoacetic acid (13.8 g, 0.1 mol) in water (50 mL) at 0 °C, until pH went to 10. A solution of **5** (2.7 g, 4.5 mmol) in ethanol (100 mL) was added to the above mixture while stirring. White precipitate came out immediately. Added dioxane until reaction solution became clear. The mixture was stirred for 36 h and pH was kept at about 10 during this time. The reaction solution was then concentrated by vacuum rotary evaporation and product was purified by silica gel column chromatography using 12:1 dichloromethane/methanol as

eluent. Compound **6** was collected as a white solid (2.3 g, 78%). ^{1}H NMR 300 MHz (CDCl$_3$) δ 8.04-7.91 (m, 1H), 7.81 (d, *J*=8.4 Hz, 1H), 7.55-7.51 (m, 2H), 7.33 (bs, 5H), 7.13 (bs, 6H), 5.08 (s, 2H), 4.95 (s, 2H), 3.51-3.39 (m, 16H), 3.14 (bs, 2H), 2.93 (bs, 2H), 2.53 (s, 3H). MS (ESI)[+] [M+H][+] calcd 654.3, found 654.7.

Dibenzyl-4-(2-(6-(2-((N-(5-fluoro-2-phenoxyphenyl)acetamido)methyl)-4-methoxyphenylamino)hexylamino)-2-oxoethyl)-10-((6-methylquinolin-2-yl)methyl)-1,4,7,10-tetraazacyclododecane-1,7-dicarboxylate (7). A mixture of compound **6** (654 mg, 1 mmol), TSTU (301 mg, 1 mmol) and TEA (5 mL) in dichloromethane (80 mL) was stirred in a round bottom flask under argon at room temperature for 2.5 h. A solution of 6-TSPOmbb732 (480 mg, 1 mmol) in dichloromethane (30 mL) was added slowly to the above mixture and the resultant mixture was stirred at room temperature overnight. Reaction solution was concentrated by vacuum rotary evaporation and product was purified by silica gel column using 30:1 dichloromethane/methanol as eluent. Compound **7** was collected as a yellow oil (922 mg, 83%). ^{1}H NMR 400 MHz (CDCl$_3$) δ 7.95 (bs, 1H), 7.88 (d, *J*=8.4 Hz, 1H), 7.54-7.51 (m, 2H), 7.31-7.21 (m, 13H), 7.09 (t, *J*=7.2 Hz, 1H), 6.96-6.91 (m, 1H), 6.83-6.79 (m, 1H), 6.73-6.69 (m, 4H), 6.38 (d, *J*=8.8 Hz, 1H), 6.19 (d, *J*=2.8 Hz, 1H), 5.02 (bs, 4H), 4.90 (d, *J*=14.8 Hz, 1H), 4.56 (d, *J*=14.8 Hz, 1H), 3.91 (bs, 2H), 3.60 (s, 3H), 3.39 (bs, 9H), 3.16 (bs, 3H), 2.97-2.83 (m, 4H), 2.78-2.75 (m, 7H), 2.53 (s, 4H), 1.91 (s, 3H), 1.57-1.50 (m, 4H), 1.40-1.28 (m, 4H). MS (ESI)[+] [M+H][+] calcd 1115.6, found 1115.7.

N-(5-Fluoro-2-phenoxyphenyl)-N-(5-methoxy-2-(6-(2-(7-(((6-methylquinolin-2-yl)methyl)-1,4,7,10-tetraazacyclododecan-1-yl)acetamido)hexylamino)benzyl) acetamide (8). A mixture of compound **7** (360 mg, 0.32 mmol) and 10% Pd/C (11 mg,

0.03 mmol) in anhydrous ethanol (9 mL) was stirred under hydrogen positive pressure at room temperature for 2 d. Pd/C was removed by filtration through celite and filtrate was concentrated by vacuum rotary evaporation. The product was then purified by silica gel column using 9:1:0.1 dichloromethane/methanol/aqueous ammonia as eluent. Compound **8** was isolated as a yellow oil (226 mg, 83%). ^{1}H NMR 400 MHz (CDCl$_3$) δ 8.03 (d, J=8.4 Hz, 1H), 7.87 (d, J=8.4 Hz, 1H), 7.55-7.50 (m, 2H), 7.43 (d, J=8.4 Hz, 1H), 7.29-7.24 (m, 2H), 7.09 (t, J=7.5 Hz, 1H), 6.97-6.90 (m, 1H), 6.83-6.78 (m, 1H), 6.73-6.68 (m, 4H), 6.35 (d, J=8.7 Hz, 1H), 6.18 (d, J=3.0 Hz, 1H), 4.88 (d, J=14.4 Hz, 1H), 4.57 (d, J=14.4 Hz, 1H), 4.01 (s, 2H), 3.74 (d, J=9.6 Hz, 1H), 3.60 (s, 3H), 3.28 (s, 2H), 3.22 (q, J=7.5 Hz, 2H), 2.83-2.77 (m, 20H), 2.51 (s, 4H), 1.91 (s, 3H), 1.53-1.43 (m, 4H), 1.33-1.22 (m, 4H). MS (ESI)$^+$ [M+H]$^+$ calcd 847.5, found 847.9.

Di-*tert*-butyl-(4-(2-(6-(2-((N-(5-fluoro-2-phenoxyphenyl)acetamido)methyl)-4-methoxyphenylamino)hexylamino)-2-oxoethyl)-10-((6-methylquinolin-2-yl)methyl)-1,4,7,10-tetraazacyclododecane-1,7-diyl)bis(methylene)diphosphonate (9).

Paraformaldehyde (1.5 mg, 50 μmol) was added to a stirring solution of compound **8** (17 mg, 20 μmol) in anhydrous THF (1 mL) and the mixture was stirred under argon for 1 h. Tri-*tert*-butyl-phosphite[36] (46 mg, 180 μmol) was added to the above mixture and the reaction solution was stirred for 2 days. After the mixture was concentrated by vacuum rotary evaporation, product was purified via column chromatography (silica gel) using 15:1:0.1 dichloromethane/methanol/aqueous ammonia as eluent. Compound **9** was collected as a colorless oil (13 mg, 52%). ^{1}H NMR 400 MHz (CDCl$_3$) δ 9.39 (t, J=5.4 Hz, 1H), 8.75 (d, J=8.7 Hz, 1H), 8.02 (d, J=8.4 Hz, 1H), 7.62-7.53 (m, 2H), 7.31-7.19 (m, 2H), 7.10 (t, J=7.5 Hz, 1H), 6.67-6.91 (m, 1H), 6.84-6.79 (m, 1H), 6.75-6.68 (m, 4H),

6.38 (d, *J*=8.7 Hz, 1H), 6.20 (d, *J*=3.0 Hz, 1H), 4.90 (d, *J*=14.7 Hz, 1H), 4.60 (d, *J*=14.7 Hz, 1H), 3.94 (bs, 1H), 3.60 (s, 6H), 3.39-3.33 (m, 2H), 3.08-2.95 (m, 4H), 2.88-2.82 (m, 4H), 2.67-2.59 (m, 8H), 2.53-2.46 (m, 11H), 1.95 (s, 3H), 1.49-1.38 (m, 8H), 1.11 (bs, 36H). MS (ESI)$^+$ [M+2H]$^{2+}$ calcd 630.4, found 630.5.

(4-(2-(6-(2-((N-(5-fluoro-2-phenoxyphenyl)acetamido)methyl)-4-methoxyphenylamino)hexylamino)-2-oxoethyl)-10-((6-methylquinolin-2-yl)methyl)-1,4,7,10-tetraazacyclododecane-1,7-diyl)bis(methylene)diphosphonic acid (10). A solution of compound **9** (23 mg, 18 µmol) in trifluoroacetic acid (TFA) (2 mL) was stirred at room temperature overnight. Reaction solution was then concentrated by vacuum rotary evaporation and product was used without purification. ^{1}H NMR 300 MHz (MeOD) δ 8.97 (bs, 1H), 8.43 (d, *J*=9.0 Hz, 1H), 8.06 (bs, 1H), 7.98-7.91 (m, 1H), 7.42 (d, *J*=8.7 Hz, 1H), 7.36-7.27 (m, 4H), 7.25-7.14 (m, 2H), 7.03 (dd, *J*=9.0, 3.0 Hz, 1H), 6.94-9.89 (m, 1H), 6.76 (d, *J*=8.4 Hz, 2H), 6.58 (d, *J*=3.0 Hz, 1H), 5.15 (d, *J*=15.3 Hz, 1H), 4.73 (d, *J*=15.0 Hz, 1H), 4.40 (bs, 2H), 3.98 (s, 2H), 3.72 (s, 4H), 3.64-3.47 (m, 8H), 3.28-3.06 (m, 9H), 2.88 (bs, 6H), 2.63 (s, 3H), 2.04 (s, 3H), 1.80-1.67 (m, 2H), 1.38-1.24 (m, 8H). MS (ESI)$^+$ [M+2H]$^{2+}$ calcd 518.2, found 518.4.

(4-(2-(6-(2-((N-(5-fluoro-2-phenoxyphenyl)acetamido)methyl)-4-methoxyphenylamino)hexylamino)-2-oxoethyl)-10-((6-methylquinolin-2-yl)methyl)-1,4,7,10-tetraazacyclododecane-1,7-diyl)bis(methylene)diphosphonic acid, europium(III) chelate (Eu-MQ-Phos-6T). A mixture of compound **10** (9 mg, 9 µmol) and Europium (III) trifluoromethanesulfonate (6 mg, 10 µmol) in acetonitrile (3 mL) was refluxed for 2.5 days. Solvent was then removed by vacuum rotary evaporation. MS (ESI)$^+$ [M+H]$^+$ calcd 1185.4, found 1185.4.

***tert*-Butyl-2,2'-(4-(2-(benzyloxy)-2-oxoethyl)-1,4,7,10-tetraazacyclododecane-1,7-diyl)diacetate (12).** Compound **11** was synthesized as reported[37]. A solution of benzyl-2-bromoacetate (350 mg, 1.53 mmol) in anhydrous acetonitrile (15 mL) was added dropwise to a stirring solution of **11** (795 mg, 1.99 mmol) in anhydrous acetonitrile (40 mL). The mixture was stirred under argon for an hour and then concentrated by vacuum rotary evaporation. The product was purified on a silica gel column using gradient 1:99 to 10:90 methanol/chloroform as eluent. **12** was collected as a white solid (446 mg, 53%). ^{1}H NMR 300 MHz (CDCl$_3$) δ 7.39-7.32 (m, 5H), 5.15 (s, 2H), 3.45 (s, 2H), 3.34 (s, 4H), 3.12-3.06 (m, 4H), 2.94-2.81 (m, 12H), 1.45 (s, 18H). MS (ESI)$^+$ [M+H]$^+$ calcd 549.4, found 549.3.

***tert*-Butyl-2,2'-(4-(2-(benzyloxy)-2-oxoethyl)-10-(2-oxo-2H-chromene-3-carbonyl)-1,4,7,10-tetraazacyclododecane-1,7-diyl)diacetate (13).** A mixture of coumarin-3-carboxylic acid (95 mg, 0.5 mmol), anhydrous DMF (4 μL) and oxalyl chloride (69.8 mg, 0.55 mmol) in anhydrous dichloromethane (3 mL) was stirred at 0 ºC under argon for 10 mins. The ice bath was then removed and reaction continued stirring at room temperature for 2 hours. The solution was then concentrated by vacuum rotary evaporation and re-dissolved with anhydrous THF (2 mL) as coumarin-3-carboxylic acid chloride solution. In another dry round bottom flask, 2.5 M n-butyl lithium in hexanes (60 μL, 0.15 mmol) was added dropwise to a solution of **12** (55 mg, 1mmol) in anhydrous THF (2 mL) at -78 ºC. After the mixture was stirred for 15 mins, the coumarin-3-carboxylic acid chloride in THF solution was added dropwise. The resulting mixture was stirred in dry ice/acetone bath for another 30 mins. The reaction was quenched by saturated sodium bicarbonate solution (1 mL) and partitioned between

dichloromethane (20 mL) and water (8 mL). The aqueous solution was extracted with dichloromethane three times (3 × 20 mL), and the organic layers were combined, dried over sodium sulfate and concentrated by vacuum rotary evaporation. Product was purified by silica gel column chromatography using gradient 1:49 to 1:5 dichloromethane/methanol as eluent to yield **13** as a brown oil (35.5 mg, 49%). ^{1}H NMR 400 MHz (CDCl$_3$) δ 7.84 (s, 1H), 7.55 (t, J=7.6 Hz, 1H), 7.50 (d, J=7.6 Hz, 1H), 7.38-7.27 (m, 7H), 5.12 (s, 2H), 3.80-3.72 (m, 4H), 3.49 (s, 2H), 3.34 (s, 2H), 3.16 (s, 2H), 3.04-3.92 (m, 4H), 2.82-2.66 (m, 8H), 1.47 (s, 9H), 1.35 (s, 9H). MS (ESI)$^+$ [M+H]$^+$ calcd 721.4, found 721.3.

2-(4,10-Bis(2-*tert*-butoxy-2-oxoethyl)-7-(2-oxo-2H-chromene-3-carbonyl)-1,4,7,10-tetraazacyclododecan-1-yl)acetic acid (14). A mixture of **13** (35 mg, 49 μmol) and palladium on carbon (5%, 10 mg) in methanol (2 mL) was stirred under hydrogen overnight. Reaction solution was then filtered through celite and concentrated by vacuum rotary evaporation. Flash chromatography of the residue over silica gel, using 9:1:0.1 dichloromethane/methanol/ aqueous ammonia, gave **14** (18 mg, 59%) as a pale yellow oil. ^{1}H NMR 400 MHz (CDCl$_3$) δ 8.17 (s, 1H), 7.64 (d, J=7.6 Hz, 1H), 7.58 (t, J=7.6 Hz, 1H), 7.34 (d, J=8.4 Hz, 2H), 3.8-2.8 (m, 22H), 1.46 (s, 9H), 1.34 (s, 9H). MS (ESI)$^+$ [M+Na]$^+$ calcd 653.3, found 653.2.

***tert*-Butyl 2,2'-(4-(2-(6-(2-((N-(5-fluoro-2-phenoxyphenyl)acetamido)methyl)-4-methoxyphenylamino)hexylamino)-2-oxoethyl)-10-(2-oxo-2H-chromene-3-carbonyl)-1,4,7,10-tetraazacyclododecane-1,7-diyl)diacetate (15).** TEA (200 μL) and TSTU (17.2 mg, 56 μmol) was added to a stirring solution of **14** (36 mg, 56 μmol) in anhydrous dichloromethane (4 mL). The resulting mixture was stirred under argon for 2.5

h. A solution of 6-TSPOmbb732 (32 mg, 68 μmol) was then added and the stirring continued overnight. Evaporation of the solvent and flash silica gel chromatography of the residue using gradient 99:1:0.1 to 9:1:0.1 dichloromethane/methanol/aqueous ammonia yielded **15** (34.2 mg, 56%) as a yellow oil. ^{1}H NMR 400 MHz (CDCl$_3$) δ 7.94 (s, 1H), 7.84 (m, 1H), 7.55-7.48 (m, 2H), 7.37-7.28 (m, 3H), 7.10 (t, *J*=7.6 Hz, 1H), 6.97-6.92 (m, 1H), 6.84-6.81 (m, 1H), 6.75-6.71 (m, 4H), 6.39 (d, *J*=8.8 Hz, 1H), 6.20 (d, *J*=2.8 Hz, 1H), 4.92 (d, *J*=14.8 Hz, 1H), 4.59 (d, *J*=14.4 Hz, 1H), 3.83-3.70 (m, 4H), 3.61 (s, 3H), 3.30 (s, 2H), 3.24-3.15 (m, 4H), 3.08-2.66 (m, 13H), 2.64-2.50 (m, 4H), 1.94 (s, 3H), 1.56-1.29 (m, 27H). MS (ESI)$^+$ [M+H]$^+$ calcd 1092.6, found 1092.5.

2,2'-(4-(2-(6-(2-((N-(5-Fluoro-2-phenoxyphenyl)acetamido)methyl)-4-methoxyphenylamino)hexylamino)-2-oxoethyl)-10-(2-oxo-2H-chromene-3-carbonyl)-1,4,7,10-tetraazacyclododecane-1,7-diyl)diacetic acid (16). A solution of **15** (16 mg, 15 μmol) in TFA (2 mL) was stirred at room temperature for 4 h. TFA was then removed by vacuum rotary evaporation and **16** was used for chelation without further purification. ^{1}H NMR 500 MHz (MeOD) δ 8.36 (s, 1H), 7.65 (d, *J*=7.5 Hz, 1H), 7.61(d, *J*=8.0 Hz, 1H), 7.36-7.33 (m, 2H), 7.28-7.22 (m, 4H), 7.17-7.12 (m, 1H), 7.09 (t, *J*=7.5 Hz, 1H), 6.95 (dd, *J*=9.0, 2.5 Hz, 1H), 6.85-6.82 (m, 1H), 6.66 (d, *J*=8.0 Hz, 2H), 6.51 (d, *J*=2.5 Hz, 1H), 5.06 (d, *J*=15.0 Hz, 1H), 4.61 (d, *J*=15.0 Hz, 1H), 3.90 (s, 2H), 3.84-3.72 (m, 2H), 3.62-3.57 (m, 2H), 3.66 (s, 3H), 3.40-3.05 (m, 18H), 1.93 (s, 3H), 1.80-1.76 (m, 2H), 1.59-1.55 (m, 2H), 1.42-1.34 (m, 4H), 1.28-1.20 (m, 4H). MS (ESI)$^+$ [M+H]$^+$ calcd 980.5, found 980.5.

2,2'-(4-(2-(6-(2-((N-(5-Fluoro-2-phenoxyphenyl)acetamido)methyl)-4-methoxyphenylamino)hexylamino)-2-oxoethyl)-10-(2-oxo-2H-chromene-3-

carbonyl)-1,4,7,10-tetraazacyclododecane-1,7-diyl)diacetic acid, europium(III) chelate (Eu-CM-Carb-6T) (17). A mixture of **16** (1.1 mg, 1.1 μmol), TEA (0.5 μL) and Europium (III) trifluoromethanesulfonate (1 mg, 1.7 μmol) in methanol (1 mL) was stirred at room temperature overnight. The reaction solution was then concentrated by vacuum rotary evaporation and crude product **17** was collected. MS (ESI)$^+$ [M]$^+$ calcd 1130.4, found 1130.4.

DOTA-tris(*tert*-butyl)-6-TSPOmbb732 A mixture of 6-TSPOmbb732 (50 mg, 0.1 mmol), DOTA-tri(*tert*-butyl)-NHS ester (82 mg, 0.1 mmol), and TEA (200 μL) in anhydrous dichloromethane (6 mL) was stirred under argon at room temperature for 1.5 h. The mixture was then concentrated by vacuum rotary evaporation and product was isolated by silica gel column chromatography using gradient 24:1 to 12:1 dichloromethane/methanol as eluent. DOTA-tris(tert-butyl)-6-TSPOmbb732 was collected as a yellow oil (77 mg, 74%). ^{1}H NMR 400 MHz (CDCl$_3$) δ 7.30-7.26 (m, 2H), 7.10 (t, *J*=7.6 Hz, 1H), 6.96-6.91 (m, 1H), 6.83-6.79 (m, 1H), 6.74-6.70 (m, 4H), 6.39 (d, *J*=8.8 Hz, 1H), 6.36 (t, *J*=5.6 Hz, 1H), 6.19 (d, *J*=2.8 Hz, 1H), 4.89 (d, *J*=14.4 Hz, 1H), 4.84 (bs, 1H), 4.60 (d, *J*=14.4 Hz, 1H), 3.60 (s, 3H), 3.20-3.15 (m, 3H), 3.02-2.95 (m, 3H), 2.89-2.83 (m, 3H), 2.79-2.00 (m, 16H), 1.93 (s, 3H), 1.55-1.49 (m, 3H), 1.45 (s, 9H), 1.44 (s, 18H), 1.37-1.25 (m, 8H). MS (ESI)$^+$ [M+2H]$^{2+}$ calcd 517.8, found 518.0.

DOTA-6-TSPOmbb732 A mixture of DOTA-tris(tert-butyl)-6-TSPOmbb732 (30 mg, 29 μmol) and TFA (2 mL) was stirred at room temperature for 1 h. TFA was then removed by vacuum rotary evaporation and the residue was purified using silica gel chromatography using gradient 12:1:0.1 to 2:1:0.1 dichloromethane/methanol/aqueous ammonia to yield DOTA-6-TSPOmbb732 as a brown solid (17 mg, 68%). ^{1}H NMR 400

MHz (CDCl3) δ 7.28 (t, *J*=7.6 Hz, 2H), 7.09 (t, *J*=7.2 Hz, 1H), 6.92 (t, *J*=7.2 Hz, 1H), 6.83-6.78 (m, 1H), 6.75-6.67 (m, 4H), 6.40 (d, *J*=8.8 Hz, 1H), 6.19 (d, *J*=4.8 Hz, 1H), 4.98-4.85 (m, 1H), 4.59-4.45 (m, 1H), 3.80-3.62 (m, 3H), 3.57 (s, 3H), 3.51-3.33 (m, 3H), 3.05-2.60 (m, 16H), 2.40-1.96 (m, 8H), 1.91 (s, 3H), 1.57-1.30 (m, 8H). MS (ESI)$^+$ [M+H]$^+$ calcd 866.4, found 866.4.

^{64}Cu-DOTA-6-TSPOmbb732 (^{64}Cu6T) 150 μL of 1 M sodium acetate solution was added to ^{64}CuCl$_2$ (about 1 ng) solution in a plastic vial. The liquid was swished around a couple times to ensure proper mixing. 10 μL of 2 mg/mL DOTA-6-TSPOmbb732/DMSO solution was added to the above mixture and the resulting solution was stirred for 1 h. During the chelation time, a 150 mg bed volume C18 cartridge was activated by flushing with 5 mL absolute ethanol, followed by 5 mL of water. After chelation was completed, the reaction solution was added to the SPE cartridge, flushed with 5 mL water to elute extra ^{64}Cu acetate, followed by 1 mL absolute ethanol to elute product out.

4.2.2 Spectroscopic Characterization

Upon preparing NIR6T, Liss6T, Cypate6T, Eu-QM-Phos-6T and Eu-CM-Carb-6T, absorption and emission spectra were obtained at room temperature with a Shimadzu 1700 UV-vis spectrophotometer and ISS PTI spectrofluorometer respectively.

4.2.3 Binding Studies

C6 glioma cells were cultured in Dulbecco's modified Eagle medium (DMEM)-F12 medium (Gibco/Invitrogen) supplemented with 0.5% FBS and 2.5% horse serum (HS) at 3.7% CO$_2$. Cells were scraped from 150 mm culture dishes into 5 mL phosphate buffered saline (PBS), dispersed by trituration, and centrifuged at 500 x*g* for 15 min.

Cell pellets were resuspended in PBS and assayed for protein concentration. [³H]PK 11195 binding studies on 30 μg of protein from cell suspensions were performed as previously described[38]. Displacement studies using increasing concentrations of synthesized TSPO ligands were performed in the presence of 15 nM [³H]PK11195. Data were analyzed using PRISM software (vs 4.0, GraphPad, Inc., San Diego, CA).

4.2.4 Cell Imaging

MDA-MB-231 mammary adenocarcinoma breast cancer cells or C6 rat glioma cells in MaTek dishes were incubated with 1 μM NIR6T and 1 μM Liss6T in culture media for 30 min. 1 nM MitoTracker Green was then added to the plate and incubated for another 10 min. Cells were rinsed and re-incubated with saline before imaging using a Nikon epifluorescence microscope equipped with a Hamamatsu C4742-98 camera, Nikon Plan Apo 60x/1.40 oil objective, a mercury lamp, an ICG filter set, a Texas Red filter set, and a FITC filter set.

When imaged with cypate6T, MDA-MB-231 cells in MaTek dishes were incubated with 300 nM cypate6T or 300 nm free cypate dye for 30 min. Cells were rinsed and re-incubated with saline before imaging.

In stem cell tracking studies, dog bone marrow mononuclear cells (MNC), mouse embryonic epithelial progenitor cells (eEPC) and mouse embryonic stem cells (ESC) were incubated with 1 μM NIR6T, 5 μM Liss6T, 5 μM LissRo5 or the same concentration of corresponding free dye for 30 min. Cells were then washed and re-incubated with media. Fluorescence images were collected from these cells daily until no significant fluorescence signal was shown from cells dosed with TSPO targeted imaging agents. Most cells lost fluorescence signal within a week, whereas MNC cells dosed with

Scheme 4.1. Synthesis of n-TSPOmbb732
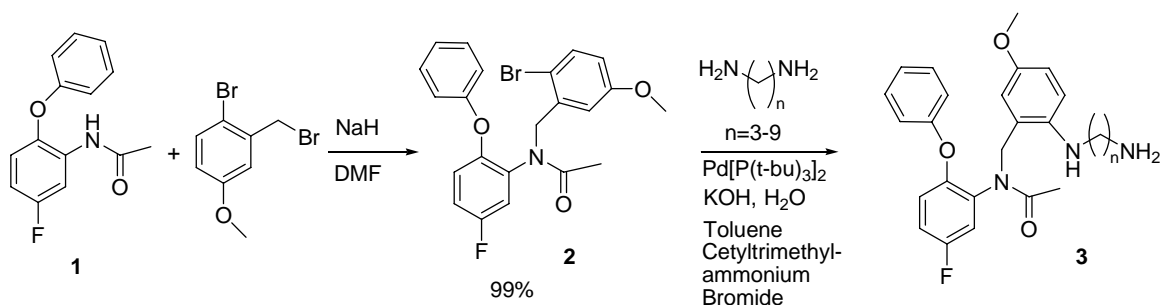
NIR6T still showed significant fluorescence signal three weeks after treatment. No further data was collected after this period.

4.3 Results and Discussion

The n-TSPOmbb732 synthetic pathway is shown in Scheme 4.1. Compound **1** was synthesized as previously reported[39]. The alkylation reaction of **1** with 2-bromo-5-methoxybenzyl bromide was straightforward and produced compound **2** at 99% yield. Aromatic substitution of a diamine (with a 3-9 carbon linker) resulted in relatively low yield (6%-33%), and is attributed to several byproducts and decomposition of the desired product prior to reaction completion. The optimal reaction time for the n-TSPOmbb732 reaction is listed in Table 4.1.

Table 4.1. n-TSPOmbb732 reactions summary

n-TSPOmbb732	Reaction time (hr)	Yield (%)
3-TSPOmbb732	3	8.7
4-TSPOmbb732	2	7.9
5-TSPOmbb732	2	10
6-TSPOmbb732	6	33
7-TSPOmbb732	2.5	12
8-TSPOmbb732	2.5	5.8
9-TSPOmbb732	2.5	11

Scheme 4.2. Capped n-TSPOmbb732 synthesis
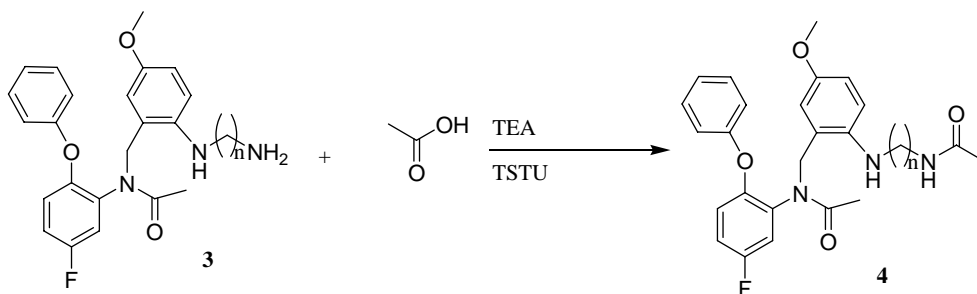
The effect of spacer length on the binding affinity of the n-TSPOmbb732 was also investigated. More specifically, n-TSPOmbb732 with 3-9 carbon spacers, was synthesized, characterized, and used in a competitive binding assay. The amino group was capped by an acetyl group to reduce non-specific binding (Scheme 4.2). The binding affinity data is shown in Table 4.2 and Figure 4.2. Lower IC50 and K_i values indicate higher binding affinities. 3-TSPOmbb732 (n-TSPOmbb732 with a three-carbon linker) (IC50=0.39 µM) and 7-TSPOmbb732 (IC50=0.40 µM) seem to have higher binding affinities than 4-TSPOmbb732 (IC50=0.80 µM) and 5-TSPOmbb732 (IC50=0.84 µM), but relatively low binding affinities compared to 6-TSPOmbb732 (IC50=0.29 µM), 8-TSPOmbb732 (IC50=0.24 µM) and 9-TSPOmbb732 (IC50=0.29 µM). Even though these binding affinities are much lower than

Table 4.2. Capped n-TSPOmbb732 binding studies

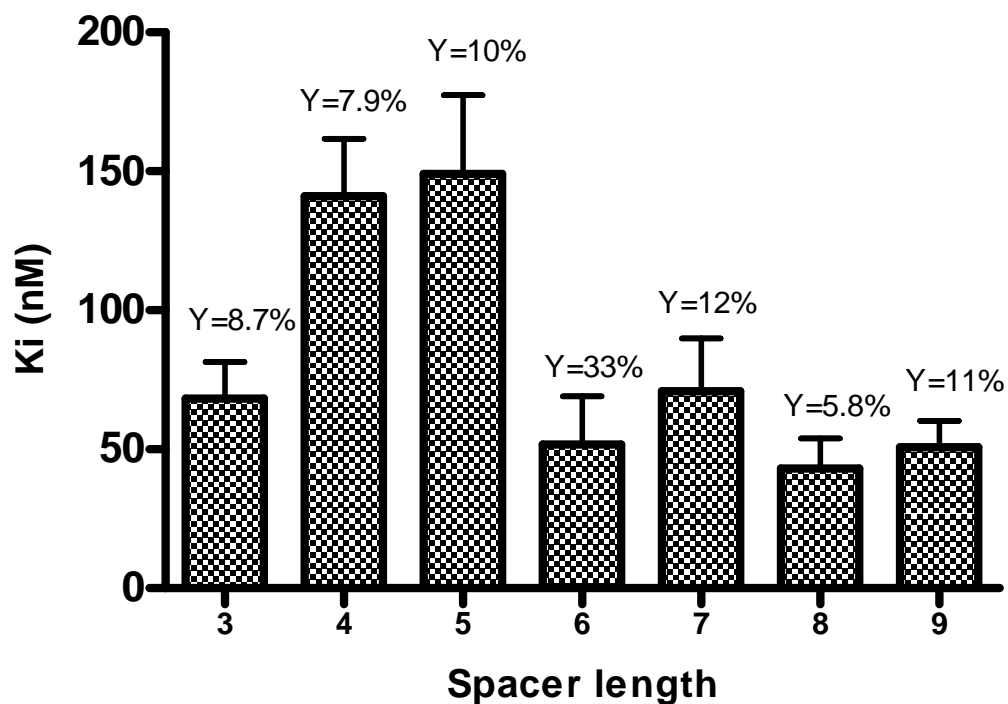| n-TSPOmbb732	IC50 (µM)	K_i (nM)
3-TSPOmbb732	0.39 ± 0.13	68 ± 23
4-TSPOmbb732	0.80 ± 0.21	141 ± 36
5-TSPOmbb732	0.84 ± 0.28	149 ± 49
6-TSPOmbb732	0.35 ± 0.22	52 ± 30
7-TSPOmbb732	0.40 ± 0.19	71 ± 33
8-TSPOmbb732	0.24 ± 0.11	43 ± 19
9-TSPOmbb732	0.29 ± 0.09	51 ± 17

Figure 4.2. Affect of spacer length (number of carbon on linker) on n-TSPOmbb732 binding affinities

DAA1106 (IC50=0.28 nM) and [11C]DAA1106 (IC50=0.91 nM), the nanomolar binding affinities (K_i=43-149 nM) appeared rather promising[39,40]. A six-carbon linker seemed to be the most optimal due to its relatively high binding affinity and yield (33%) of 6-TSPOmbb732.

NIR probes capable of targeting specific receptors are attractive noninvasive imaging tools for preclinical diagnosis[41], therefore we conjugated our relative high binding affinity TSPO-targeted ligand, 6-TSPOmbb732, to IRDye[TM] 800CW NHS ester (Scheme 4.3). The reaction was straightforward, but the overall yield was relatively low (31%), mainly due the impurities in the dye sample and side reactions.

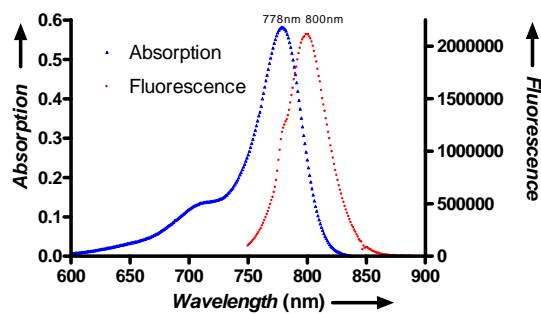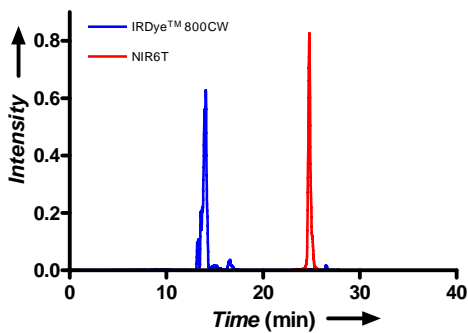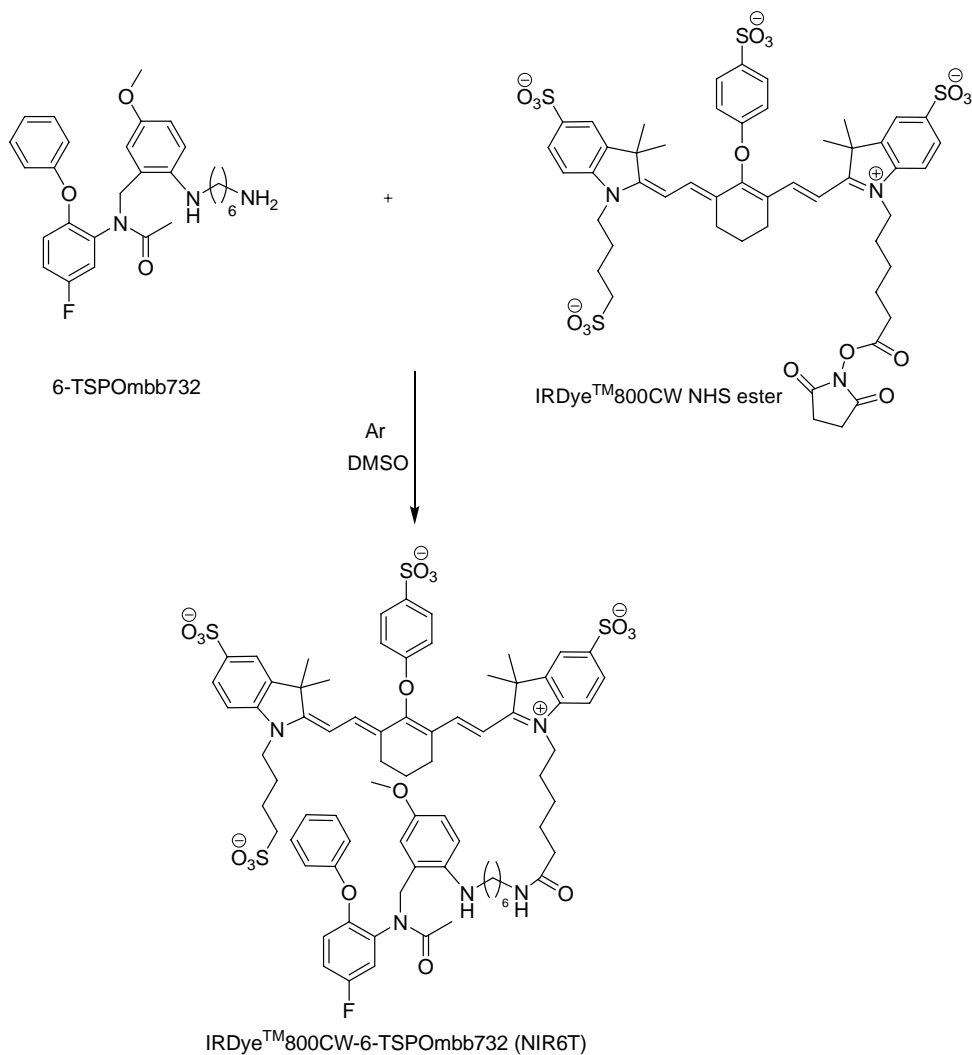**Scheme 4.3. IRDye^{TM} 800CW-6-TSPOmbb732 (NIR6T) reaction scheme**

6-TSPOmbb732

+

IRDye^{TM}800CW NHS ester

Ar
DMSO

IRDye^{TM}800CW-6-TSPOmbb732 (NIR6T)

Figure 4.3. Left: HPLC chromatograph of IRDye^{TM} 800CW and NIR6T at 780 nm; right: absorption and emission spectra of NIR6T in methanol.

Scheme 4.4. Lissamine-6-TSPOmbb732 (Liss6T) reaction scheme

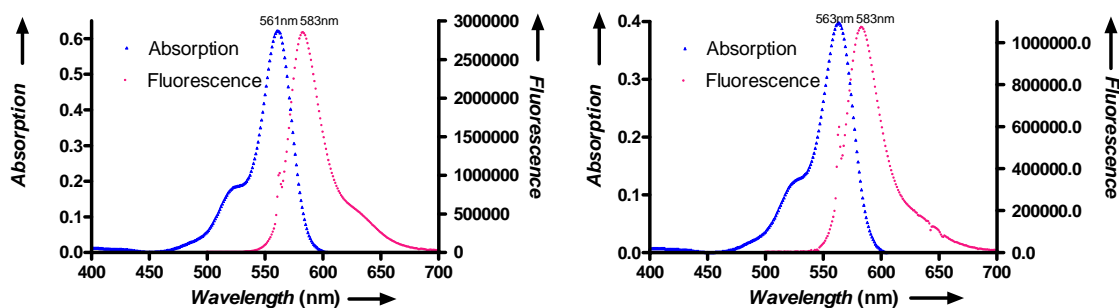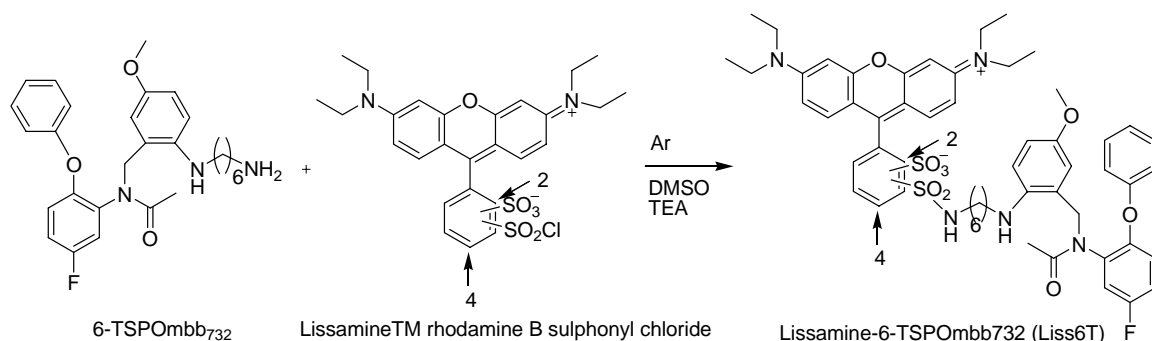6-TSPOmbb_732   Lissamine™ rhodamine B sulphonyl chloride   Lissamine-6-TSPOmbb732 (Liss6T)

Figure 4.4. Liss6T isomer (left) and isomer II (right) absorption and fluorescence

HPLC was used to monitor the production of IRDye™ 800CW-6-TSPOmbb732 (NIR6T). The chromatographs for both the NIR dye and NIR6T at 780 nm are shown in Figure 4.3 (left). Figure 4.3 (right) shows the excitation and emission spectra. The excitation of NIR6T at 778 nm and its subsequent NIR emission at 800 nm allow deep tissue penetration with reduced absorption and scattering for in vivo imaging.

Lissamine™ rhodamine B sulphonyl chloride also was used to conjugate 6-TSPOmbb732 (Liss6T) (Scheme 4.4). Lissamine is optimized for the commonly used Texas Red filter set and is well known for providing high quality images. Since the commercially available lissamine dye has two isomers, the conjugation reaction yielded two isomers as well. The conjugable ligand is in para position in isomer I and ortho position in isomer II, verified by pH test[42]. The spectroscopy curves are shown in Figure

4.4. Isomer I, which has a higher molar extinction coefficient (ε=124000 L/mol cm in methanol) than isomer II (ε=80000 L/mol cm in methanol), was selected for imaging.

Fluorescence microscopy imaging studies were performed to investigate the cellular uptake of NIR6T and Liss6T in MDA-MB-231 (human metastatic mammary adenocarcinoma) and C6 (rat glioma) cells. Accumulation of both agents in these cells was observed (Figures 4.5 and 4.6). To demonstrate mitochondrial binding of the dyes, cultures were co-incubated with MitoTracker Green, a mitochondrial marker, and our two molecules. Overlaid pictures (E, F, G and H in Figures 4.5 and 4.6) demonstrate similar organelle labeling of all three molecules, which suggested that the optical probes bind to mitochondria, the primary site of TSPO expression. In addition, fluorescence images of cells dosed with NIR6T or Liss6T were compared with those of cells dosed with corresponding free dyes. Figure 4.7 shows fluorescence images of C6 cells dosed with NIR6T, Liss6T or corresponding free dye (IRDye[TM] 800CW acid or lissamine[TM] rhodamine B sulphonyl chloride). Figure 4.8 presents fluorescence images of MDA-MB-231 cells dosed with NIR6T, Liss6T or free dye. In both figures, cells dosed with NIR6T or Liss6T showed significant fluorescence signal, whereas cells dosed with free dye are relatively devoid of fluorescence. The nanomolar binding affinities (K_i=42 nM for NIR6T and 0.91 nM for Liss6T) provided further evidence for the selective binding. In addition to IRDye[TM] 800CW, another NIR dye, cypate, was also used to label 6-TSPObmm732. Compared to most NIR dyes, cypate is relatively stable (stored at room temperature, whereas most NIR dyes need to be stored in freezer) and easy to synthesize (only takes three steps)[18]. Cypate6T was synthesized by well-established peptide coupling using 2-(1H-Benzotriazole-1-yl)-1,1,3,3-tetramethyl uronium
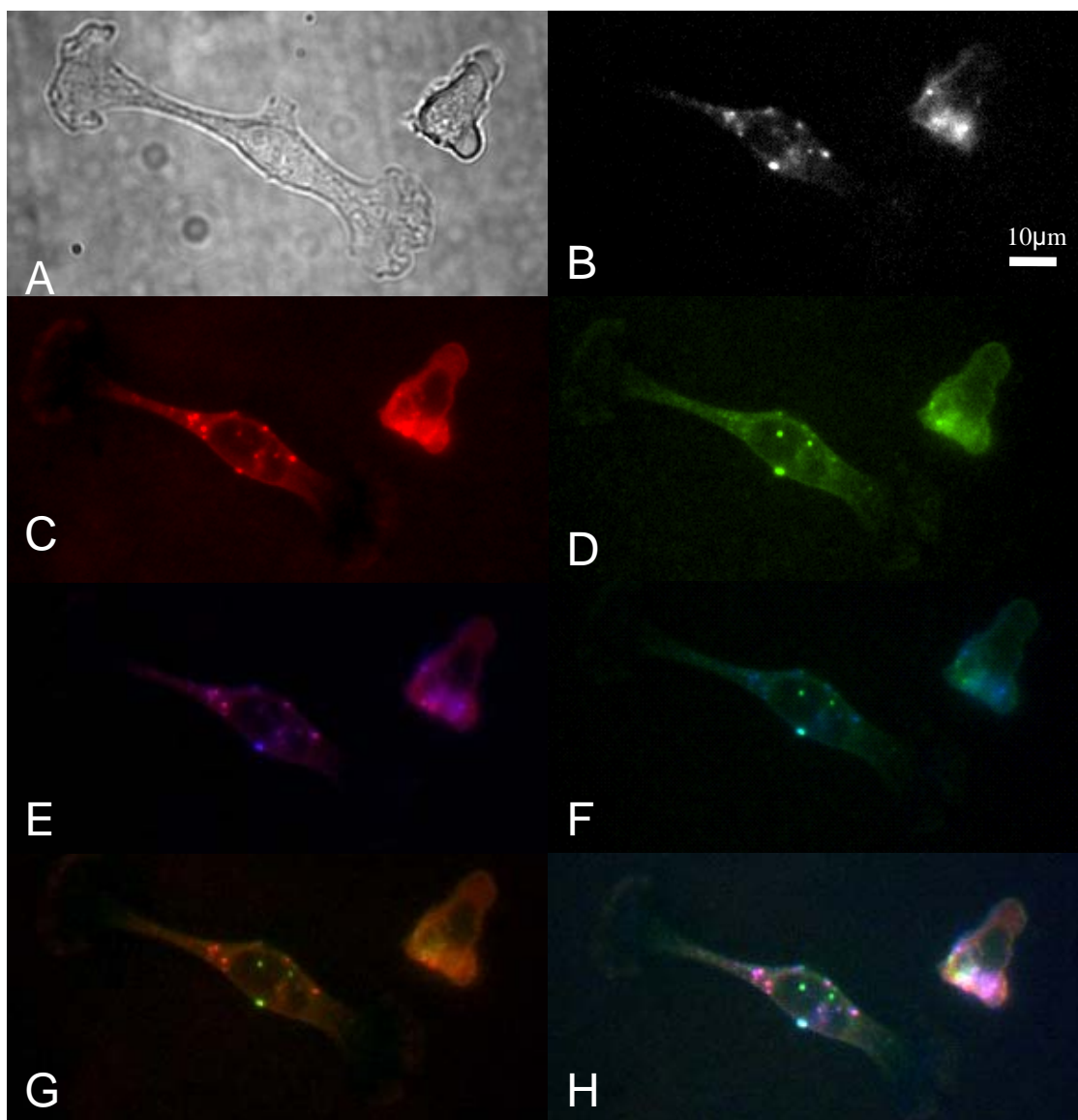
Figure 4.5. Fluorescence imaging of MDA-MB-231 cells incubated with NIR6T, Liss6T and MitoTracker Green. (A) Phase contrast microscopy of cells dosed simultaneously with NIR6T, Liss6T and MitoTracker Green; (B) fluorescence imaging of cells dosed with 1 µM NIR6T (fluorescence signal is shown blue in overlaid pictures E, F and H); (C) fluorescence imaging of cells dosed with 1 µM Liss6T; (D) fluorescence imaging of cells dosed with 1 nM MitoTracker Green; (E) overlaid picture of B and C; (F) overlaid picture of B and D; (G) overlaid picture of C and D; (H) overlaid picture of B, C and D.

Figure 4.6. Fluorescence imaging of C6 cells incubated with NIR6T, Liss6T and MitoTracker Green. (A) Phase contrast microscopy of cells dosed simultaneously with NIR6T, Liss6T and MitoTracker Green; (B) fluorescence imaging of cells dosed with 1 µM NIR6T (fluorescence signal is shown blue in overlaid pictures E, F and H); (C) fluorescence imaging of cells dosed with 1 µM Liss6T; (D) fluorescence imaging of cells dosed with 1 nM MitoTracker Green; (E) overlaid picture of B and C; (F) overlaid picture of B and D; (G) overlaid picture of C and D; (H) overlaid picture of B, C and D.
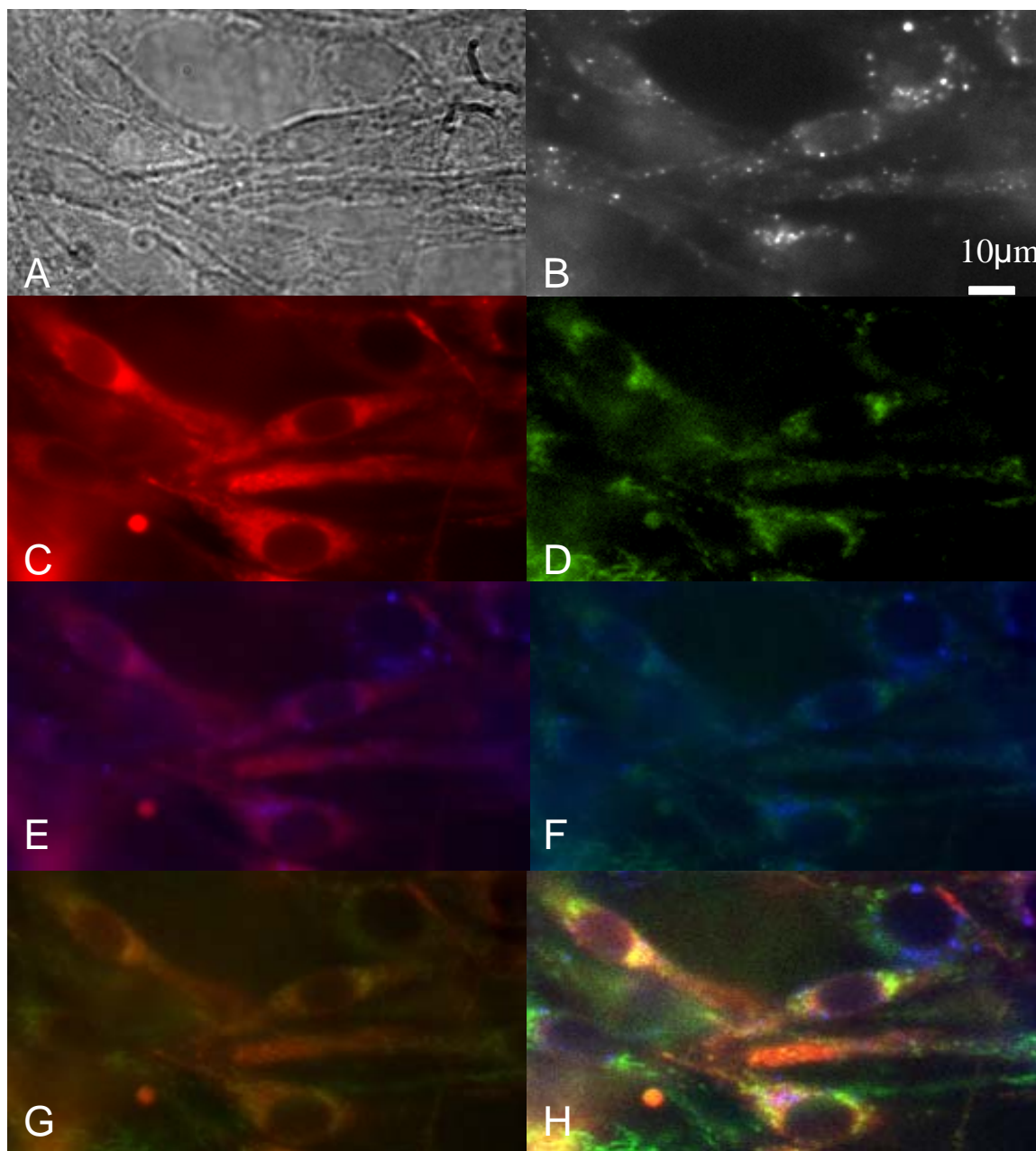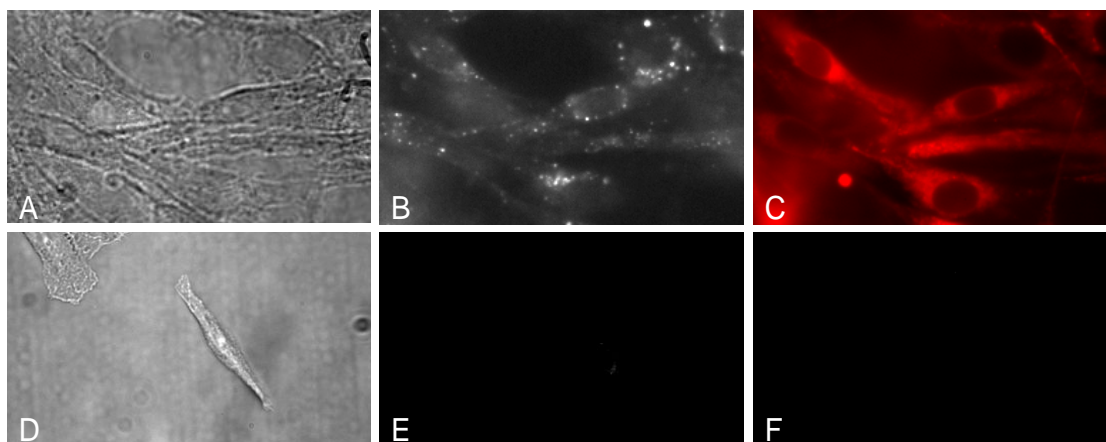
Figure 4.7. Fluorescence imaging of C6 rat glioma cells incubated with NIR6T, Liss6T or free dye: (A) Phase contrast microscopy of cells dosed with NIR6T; (B) fluorescence imaging of cells dosed with 1 µM NIR6T; (C) fluorescence imaging of cells dosed with 1 µM Liss6T; (D) Phase contrast microscopy of cells dosed with free NIR dye; (E) fluorescence imaging of cells dosed with 1 µM free NIR dye (control); (F) fluorescence imaging of cells dosed with 1 µM free lissamine dye (control).
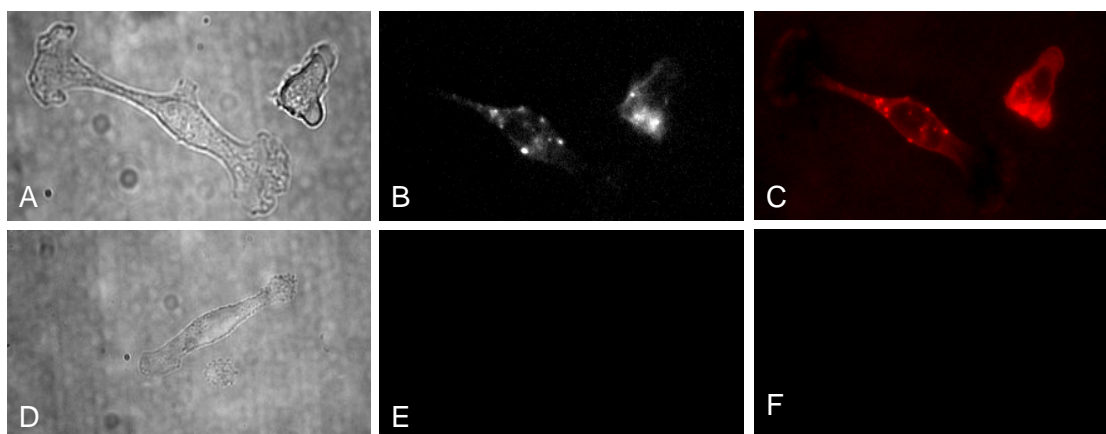

Figure 4.8. Fluorescence imaging of MDA-MB-231 human breast cancer cells incubated with NIR6T, Liss6T or free dye: (A) Phase contrast microscopy of cells dosed with NIR6T; (B) fluorescence imaging of cells dosed with 1 µM NIR6T; (C) fluorescence imaging of cells dosed with 1 µM Liss6T; (D) Phase contrast microscopy of cells dosed with free NIR dye; (E) fluorescence imaging of cells dosed with 1 µM free NIR dye (control); (F) fluorescence imaging of cells dosed with 1 µM free lissamine dye (control).

Scheme 4.5. Cypate-6-TSPOmbb732 (Cypate6T) reaction scheme
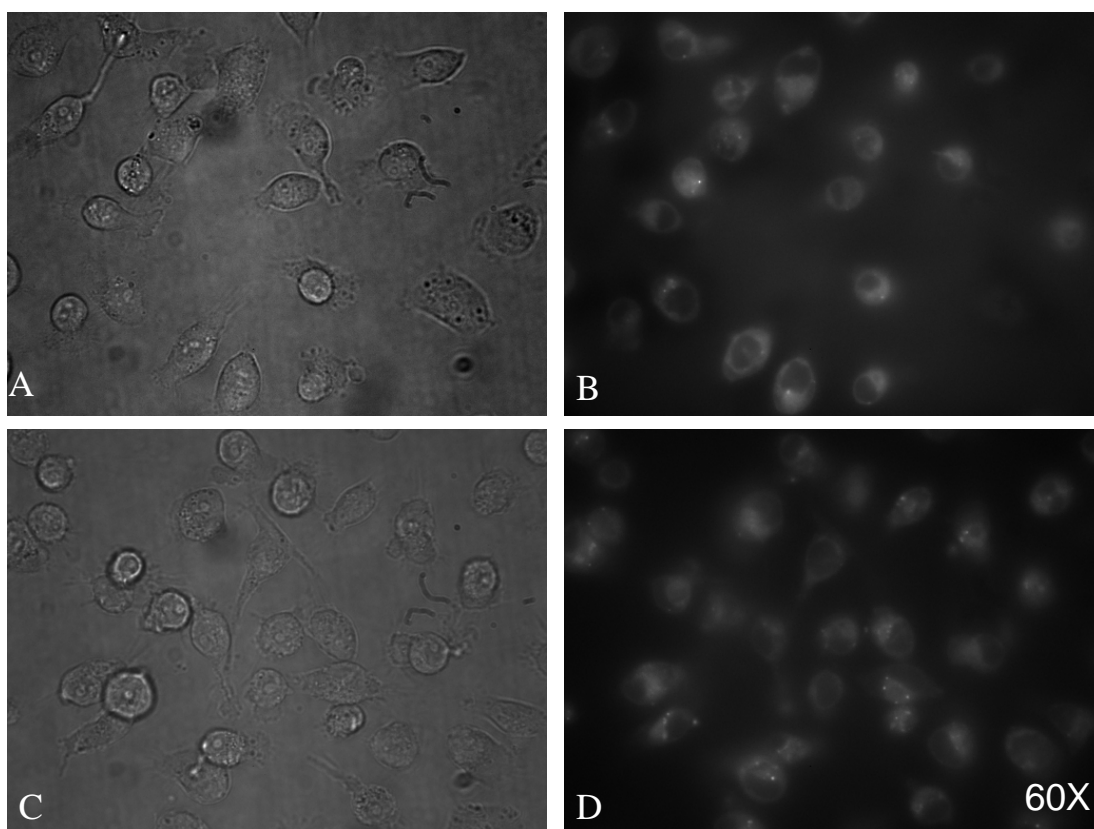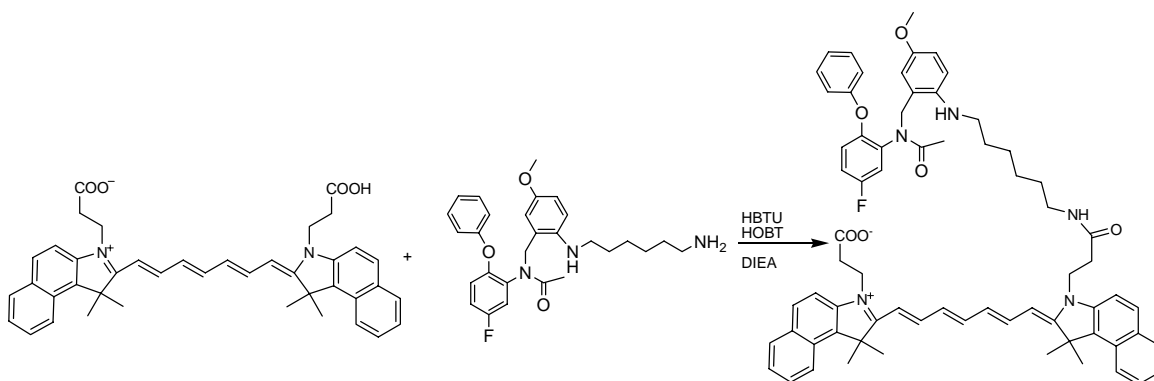

Figure 4.9. Fluorescence imaging of MDA-MB-231 human breast cancer cells incubated with cypate6T or free cypate dye: (A) Phase contrast microscopy of cells dosed with cypate6T; (B) fluorescence imaging of cells dosed with 300 nM cypate6T; (C) Phase contrast microscopy of cells dosed with free cypate dye; (D) fluorescence imaging of cells dosed with 300 nM free cypate dye (control).

hexafluorophosphate (HBTU) (Scheme 4.5). The molecule has maximum absorption at 786 nm and emission at 811 nm in methanol. Cypate6T binds to TSPO at nanomolar affinity (K_i=51±34 nm). In vitro cell imaging was conducted to study cellular uptake. MDA-MB-231 cells were dosed with 300 nm cypate6T or same concentration of free cypate dye, washed, and imaged with a fluorescence microscope. Significant fluorescence signals were seen from the cells dosed with cypate6T, unfortunately, cells dosed with same concentration of free dye showed similar fluorescence signals (Figure 4.9). We postulate that non-specific binding dominates the interaction, probably due to

Figure 4.10. Fluorescence imaging of MNC cells 21 days after treatment of 1 µM NIR6T or free dye: (A) Phase contrast microscopy of cells dosed with NIR6T; (B) fluorescence imaging of cells dosed with 1 µM NIR6T; (C) Overlay of A and B (fluorescence signal is shown blue); (D) fluorescence imaging of cells dosed with 1 µM free NIR dye (control).
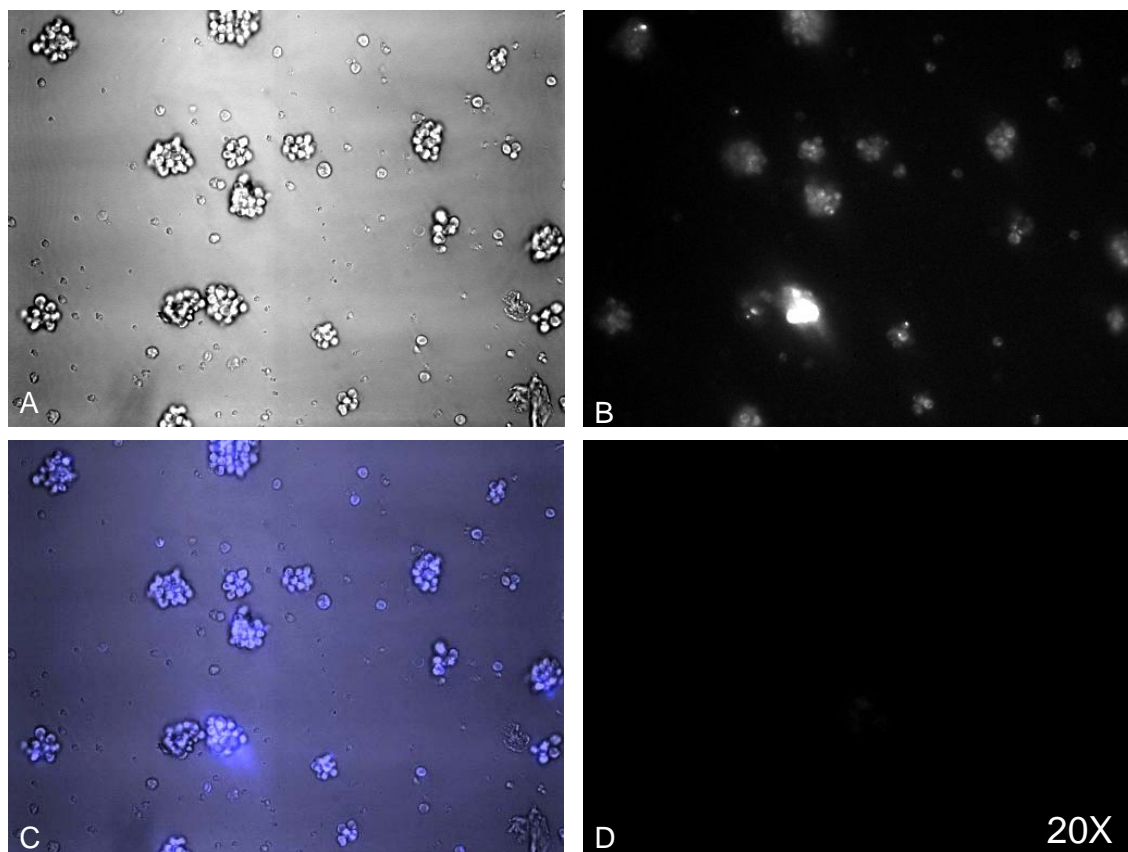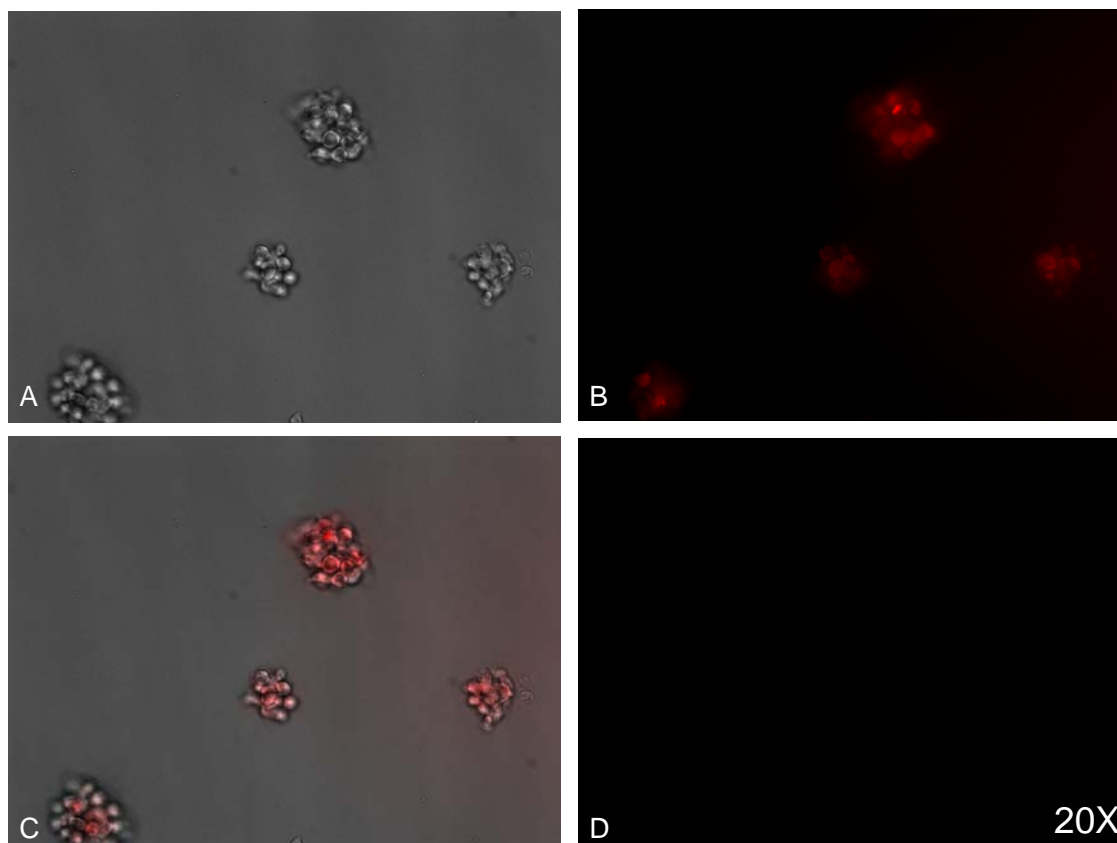
Figure 4.11. Fluorescence imaging of MNC cells 6 days after treatment of 1 µM Liss6T or free dye: (A) Phase contrast microscopy of cells dosed with Liss6T; (B) fluorescence imaging of cells dosed with 1 µM Liss6T; (C) Overlay of A and B; (D) fluorescence imaging of cells dosed with 1 µM free lissamine dye (control).

the relatively high lipophilicity of cypate dye, allowing good permeability through cell membrane.

Other than imaging diseased cells, TSPO targeted imaging agents can also be potentially used to track stem cells. In this study, dog bone marrow mononuclear cells (MNC), mouse embryonic epithelial progenitor cells (eEPC) and mouse embryonic stem cells (ESC) were labeled with NIR6T, Liss6T and LissRo5. To determine the ability of TSPO targeted agents to label stem cells over time, fluorescence imaging was conducted daily on each sample until no significant fluorescence signal was detected. Figure 4.10, 4.11 and 4.12 show three examples of the fluorescence images from MNC cells.
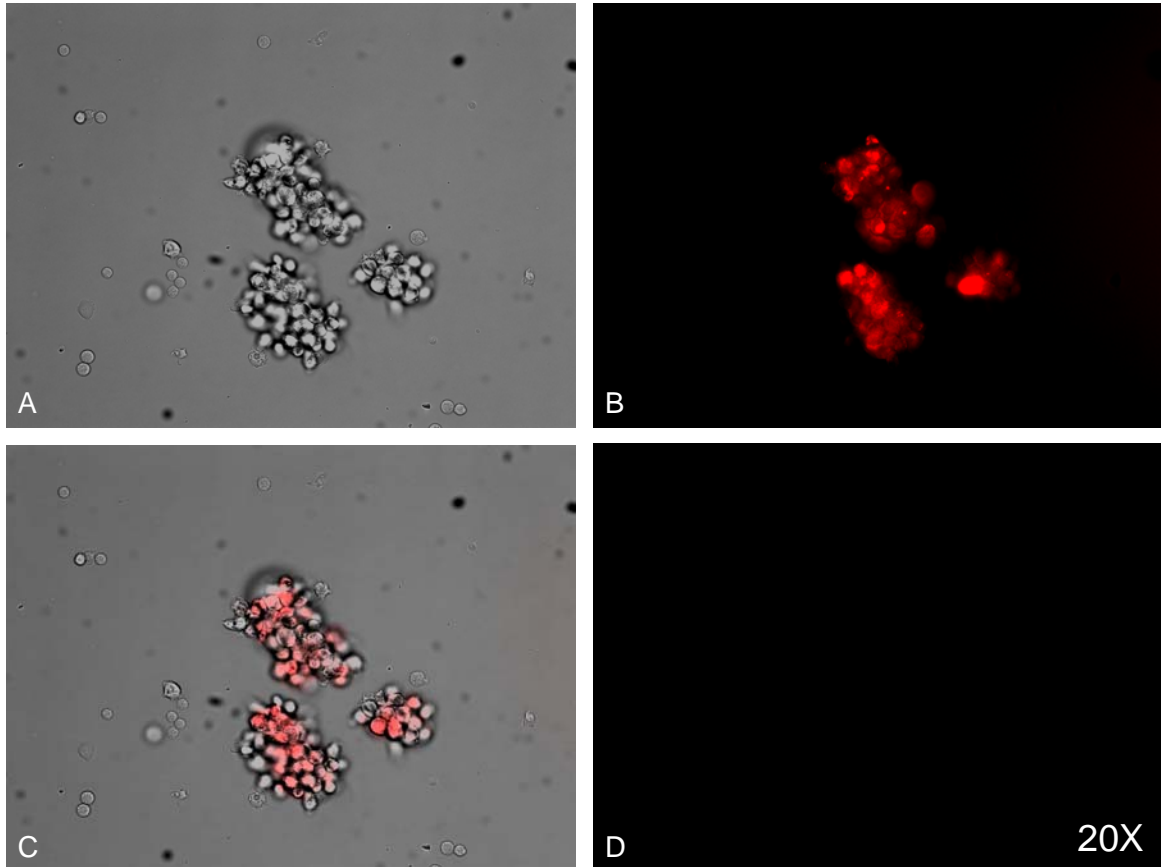
Figure 4.12. Fluorescence imaging of MNC cells 5 days after treatment of 1 µM LissRo5 or free dye: (A) Phase contrast microscopy of cells dosed with LissRo5; (B) fluorescence imaging of cells dosed with 1 µM LissRo5; (C) Overlay of A and B; (D) fluorescence imaging of cells dosed with 1 µM free lissamine dye (control).

Significant fluorescence signals were seen from the cells dosed with TSPO targeted imaging agents, whereas cells incubated with same concentration of corresponding free dye are relatively devoid of signal. Table 4.3 shows the maximum cell-tracking time, after which no significant fluorescence signal could be observed from stem cells under microscope. Generally, MNC cells were labeled for relatively long period of time compared to the other two cell lines. This indicates that MNC cells might

Table 4.3. TSPO targeted stem cell tracking (days)

	MNC	*ES*	*EPC*
NIR6T	>21	1	1
Liss6T	7	3	3
LissRo5	5	2	1

119

have higher TSPO expression than ESC and EPC cells. Most cells studies exhibited significant fluorescence signal for less than a week. The loss of signal can be explained by progressive dilution of dye-TSPO ligand complex due to cell division and clearance of unbound imaging agents from cells over time. However, MNC cells dosed with NIR6T still showed significant fluorescence signal three weeks after treatment. Even though the signal became lower during imaging period due to cell division, the clearance of NIR6T from MNC cells seems minimal, as signal reduction seems rather slow. This observation is probably partly due to relatively high binding affinity of NIR6T to TSPO receptor and high TSPO expression in MNC cells. Overall, TSPO targeted imaging agents were successfully used to label stem cells over time and can be potentially applied in stem cell tracking in vivo.

6-TSPOmbb732 was also conjugated to lanthanide chelates so as to investigate potential multi-modal imaging agents. The first attempted lanthanide chelate is Eu-MQ-Phos, which has a methyl quinoline antenna, two phosphate chelation arms and an acetic acid conjugation arm. As mentioned in section 1.8, the antenna is used to sensitize light and transfer energy to chelated europium ion. The synthesis started with alkylation reaction between bromoacetic acid and compound **5** (Scheme 4.6). Next, 6-TSPOmbb732 was conjugated to **6** by regular peptide coupling using *N,N,N′,N′*-tetramethyl-*O*-(*N*-succinimidyl)uronium tetrafluoroborate (TSTU), followed by removal of benzyl carbonate (Cbz) by hydrogenation. t*ert*-Butyl protected phosphate was introduced to **8** in presence of paraformaldehyde to yield **9**, whose *tert*-butyl protecting group was then removed by trifluoroaceitic acid (TFA). Finally, Eu^{3+} was chelated by refluxing **10** and Europium (III) trifluoromethanesulfonate in acetonitrile for two and half days. The final

Scheme 4.6. Synthetic pathway of Eu-MQ-Phos-6-TSPOmbb732 (Eu-MQ-Phos-6T)
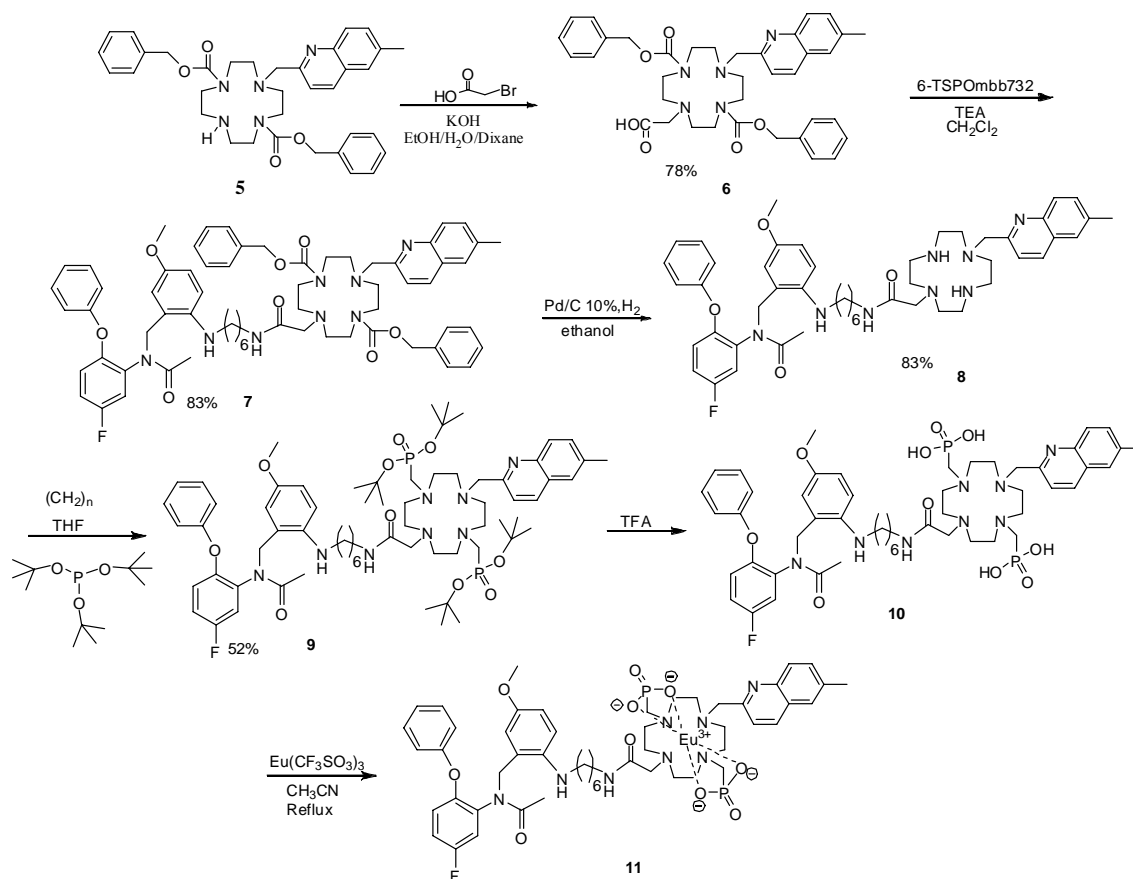
product was characterized by mass spectrometry. Figure 4.13 shows the absorption and

emission of Eu-MQ-Phos-6T in acetonitrile. Eu-MQ-Phos-6T has maximum absorption

at 322 nm and emission peaks at 421 nm, 591 nm, 611 nm and 698 nm. The broad

emission at 421 nm is likely due to methyl quinoline that did not sensitize Eu^{3+} ion. The

large peak at 645 nm is $2\lambda_{exi}$, which is due to Rayleigh scattering[43]. Peaks at 591 nm, 611

nm and 698 nm are from Eu^{3+} sensitized by methyl quinoline.

Eu-MQ-Phos-6-TSPOmbb732 seems to be a promising imaging agent, however,

it takes a lot of effort to synthesize methyl quinoline antenna (3 steps)[44]. A lanthanide

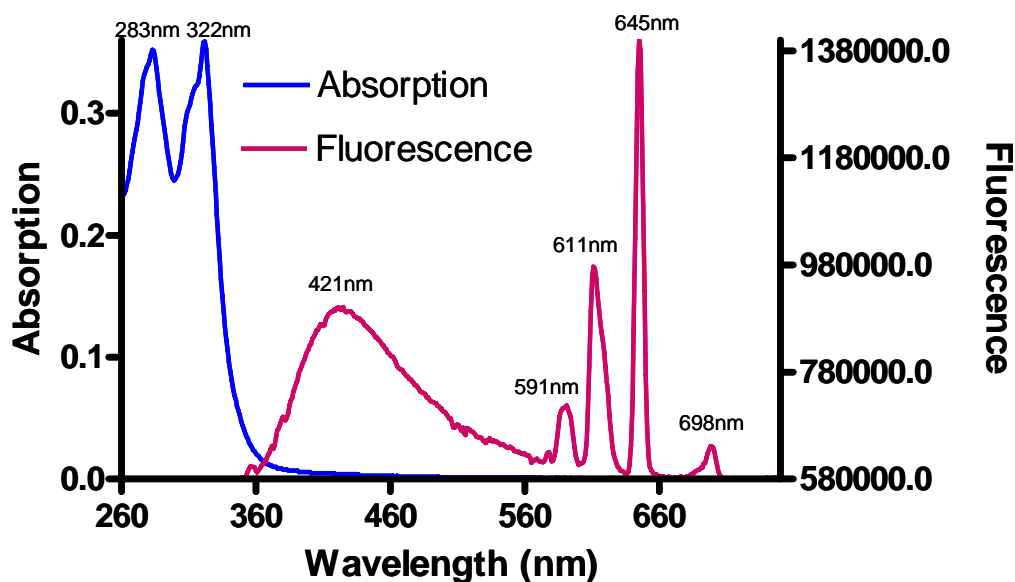chelate with a commercially available antenna is probably more favorable.

Figure 4.13. Eu-QM-Phos-6T absorption and fluorescence

The second attempted lanthanide chelate has two carboxylate chelating arms and a coumarin antenna. Compared to tri-*tert*-butyl-phosphite (phosphate arm), *tert*-butyl 2-bromoacetate (carboxylate arm) is relatively stable and the alkylation reaction with corresponding cyclen ring has higher yield (91%, reported by Sherry and coworkers[37] vs 52% for compound **9**). In addition, coumarin-3-carboxylic acid is commercially available and easily coupled to the cyclen ring. The synthetic pathway is shown in Scheme 4.7. **11** was prepared here as reported[37]. Benzyl-2-bromoacetate was then coupled to **11** via alkylation. The yield (53%) is relatively low probably due to the production of di-substituted byproduct. Next, coumarin-3-carboxylic acid was converted to acyl chloride by oxalyl chloride, and the following N-acylation reaction with **12** produced **13**. After Cbz protecting group was removed by hydrogenation, 6-TSPOmbb732 was conjugated to**14** by N-acylation using TSTU. At last, *tert*-butyl groups were removed by TFA and

Scheme 4.7. Synthetic pathway of Eu-Coumarin-Carboxyl-6-TSPOmbb732 (Eu-CC-6T)
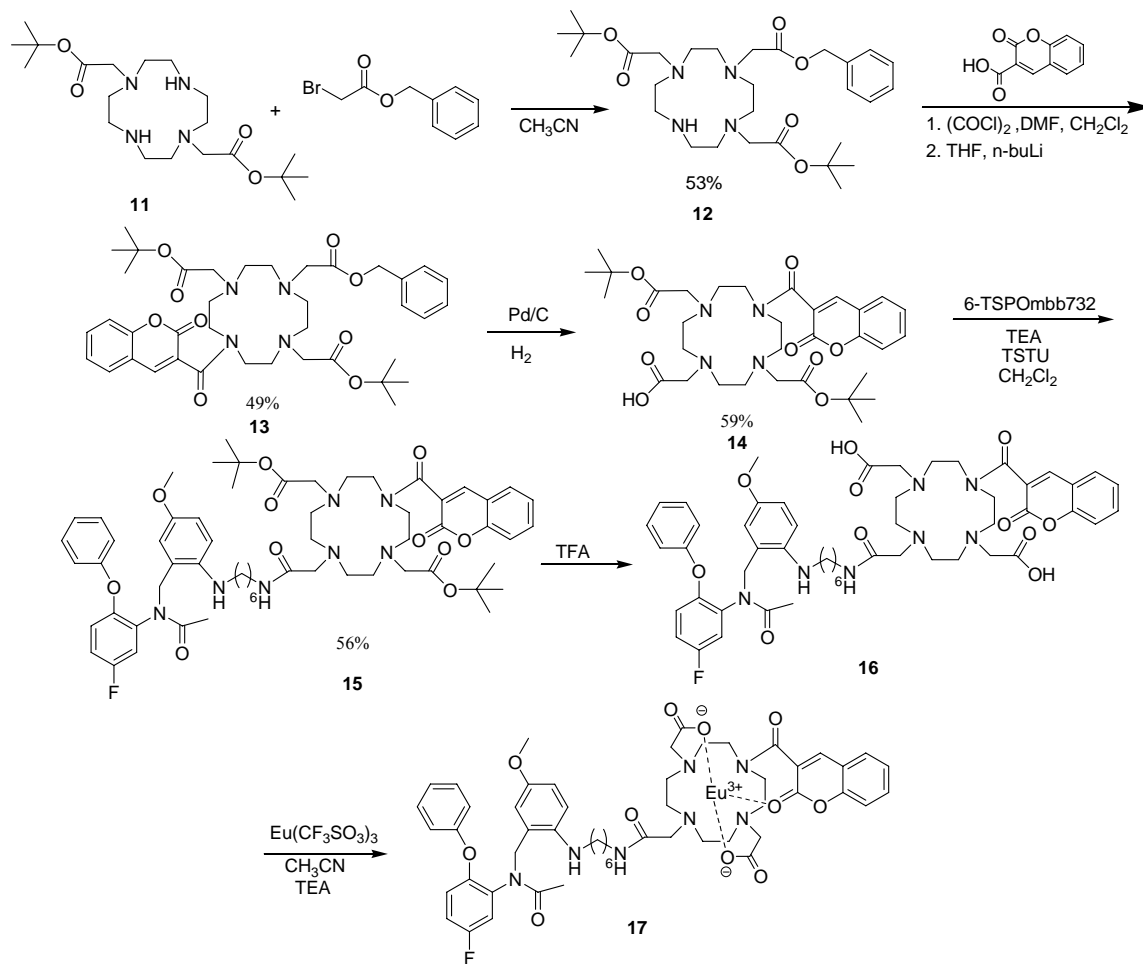
Eu^{3+} was chelated in basic solution. The absorption and emission spectra are shown in Figure 4.14.

Multimodal lanthanide chelates labeled 6-TSPOmbb732 shows promise, and if optical imaging is not a desired modality, a chelate without an antenna can be used. This simpler version of lanthanide chelate labeled 6-TSPOmbb732 was therefore synthesized. A DOTA labeled 6-TSPOmbb732 was achieved in only two steps (Scheme 4.8) and can label different ions such as ^{64}Cu (PET imaging), ^{111}In (SPECT imaging) and Gd^{3+} (MRI).
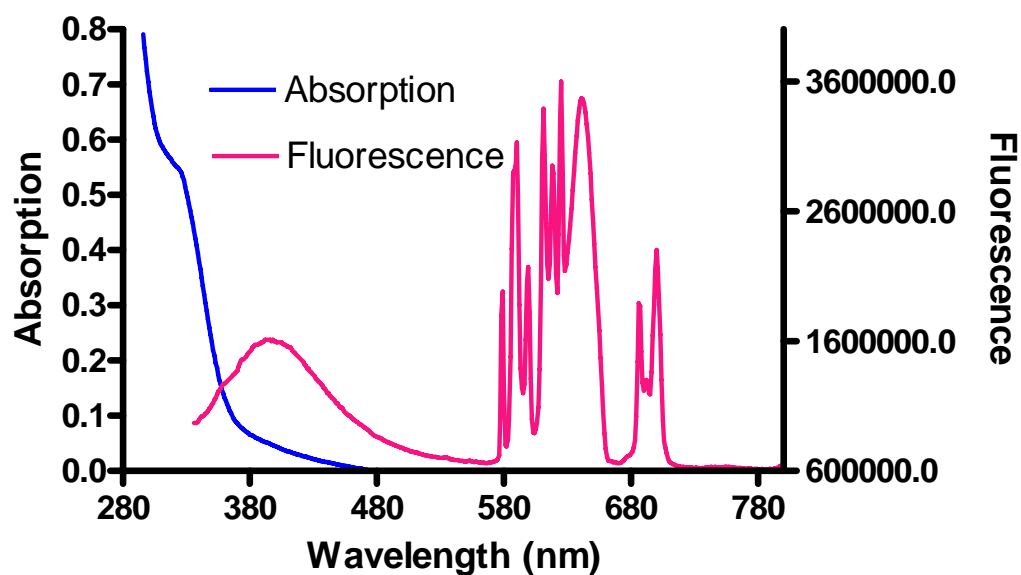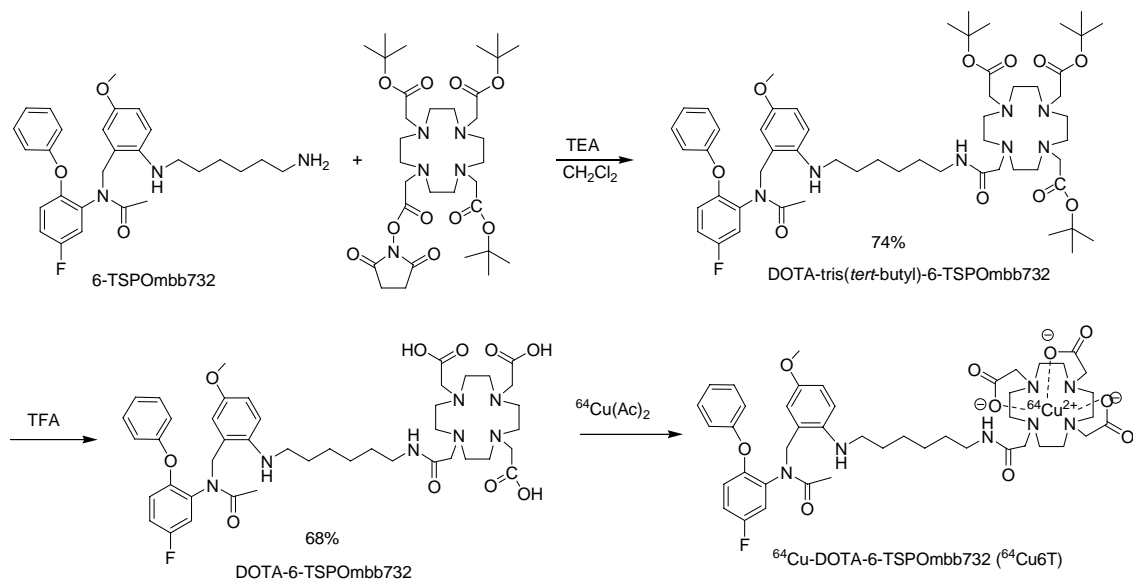
Figure 4.14. Eu-CM-Carb-6T absorption and fluorescence

Scheme 4.8. ^{64}Cu-DOTA-6-TSPOmbb732 (^{64}CuD6T) reaction scheme

The synthesis involves coupling 6-TSPOmbb732 to commercially available

DOTA-tri(*tert*-butyl)-NHS ester via N-acylation, followed by removal of *tert*-butyl

groups by TFA. We selected $^{64}Cu^{2+}$ for PET imaging applications and $^{64}Cu^{2+}$ was chelated by stirring DOTA-6-TSPOmbb732 and copper-64 acetate ($^{64}Cu(Ac)_2$) in DMSO for an hour. $^{64}Cu^{2+}$ has relatively long half life (12.7 hours), therefore, in-lab cyclotron is not necessary. ^{64}Cu-DOTA-6-TSPOmbb732 will be investigated in stem cell tracking in vivo.

4.4 Conclusion

In conclusion, we have synthesized a functional TSPO ligand, n-TSPOmbb732, which can be conjugated to a variety of signaling moieties and widely applied for TSPO targeted cancer imaging. Structure activity relationship (SAR) study indicates that 6-TSPOmbb732 is the most promising TSPO ligand. 6-TSPOmbb732 was then labeled with three fluorescent dyes, including IRDye^{TM} 800CW NHS ester, lissamine^{TM} rhodamine B sulphonyl chloride and cypate. IRDye^{TM} 800CW or lissamine^{TM} rhodamine B labeled 6-TSPOmbb732, NIR6T and Liss6T, display nanomolar binding affinities to TSPO and have been successfully imaged in vitro. Preliminary stem cell tracking studies showed that NIR6T could label MNC cells for over three weeks. Cypate6T binds to TSPO at nanomolar affinity and labels MDA-MB-231 cells as well, but free cypate dye also labels these cells. In addition, 6-TSPOmbb732 was coupled to two tri-functional lanthanide chelates for multimodal imaging. Finally, ^{64}Cu-DOTA-6-TSPOmbb732 was developed for TSPO targeted PET imaging.

4.5 Acknowledgement

4.6 References

(1)   Papadopoulos, V.; Baraldi, M.; Guilarte, T. R.; Knudsen, T. B.; Lacapere, J. J. et al. Translocator protein (18 kDa): new nomenclature for the peripheral-type benzodiazepine receptor based on its structure and molecular function. *Trends in Pharmacological Sciences* **2006**, *27*, 402-409.

(2)   Miettinen, H.; Kononen, J.; Haapasalo, H.; Helen, P.; Sallinen, P. et al. Expression of Peripheral-Type Benzodiazepine Receptor and Diazepam-Binding Inhibitor in Human Astrocytomas - Relationship to Cell-Proliferation. *Cancer Research* **1995**, *55*, 2691-2695.

(3)   Han, Z. Q.; Slack, R. S.; Li, W. P.; Papadopoulos, V. Expression of peripheral benzodiazepine receptor (PBR) in human tumors: Relationship to breast, colorectal, and prostate tumor progression. *Journal of Receptors and Signal Transduction* **2003**, *23*, 225-238.

(4)   Messmer, K.; Reynolds, G. P. Increased peripheral benzodiazepine binding sites in the brain of patients with Huntington's disease. *Neuroscience Letters* **1998**, *241*, 53-56.

(5)   Rao, V. L. R.; Dogan, A.; Bowen, K. K.; Dempsey, R. J. Traumatic brain injury leads to increased expression of peripheral-type benzodiazepine receptors, neuronal death, and activation of astrocytes and microglia in rat thalamus. *Experimental Neurology* **2000**, *161*, 102-114.

(6)   Banati, R. B. Visualising microglial activation in vivo. *Glia* **2002**, *40*, 206-217.

(7)   Decaudin, D.; Castedo, M.; Nemati, F.; Beurdeley-Thomas, A.; De Pinieux, G. et al. Peripheral benzodiazepine receptor ligands reverse apoptosis resistance of cancer cells in vitro and in vivo. *Cancer Research* **2002**, *62*, 1388-1393.

(8)   Romeo, E.; Auta, J.; Kozikowski, A. P.; Ma, D.; Papadopoulos, V. et al. 2-Aryl-3-Indoleacetamides (Fgin-1) - a New Class of Potent and Specific Ligands for the Mitochondrial Dbi Receptor (Mdr). *Journal of Pharmacology and Experimental Therapeutics* **1992**, *262*, 971-978.

(9)   Kozikowski, A. P.; Ma, D.; Brewer, J.; Sun, S.; Costa, E. et al. Chemistry, Binding Affinities, and Behavioral Properties of a New Class of Antineophobic Mitochondrial Dbi Receptor Complex (Mdrc) Ligands. *Journal of Medicinal Chemistry* **1993**, *36*, 2908-2920.

(10)   Culty, M.; Silver, P.; Nakazato, A.; Gazouli, M.; Li, H. et al. Peripheral benzodiazepine receptor binding properties and effects on steroid synthesis of two new phenoxyphenyl-acetamide derivatives, DAA1097 and DAA1106. *Drug Development Research* **2001**, *52*, 475-484.

(11)   Zhang, M. R.; Maeda, J.; Furutsuka, K.; Yoshida, Y.; Ogawa, M. et al. [F-18]FMDAA1106 and [F-18]FEDAA1106: Two positron-emitter labeled ligands for peripheral benzodiazepine receptor (PBR). *Bioorganic & Medicinal Chemistry Letters* **2003**, *13*, 201-204.

(12)   Maeda, J.; Suhara, T.; Zhang, M. R.; Okauchi, T.; Yasuno, F. et al. Novel peripheral benzodiazepine receptor ligand [C-11]DAA1106 for PET: An imaging tool for glial cells in the brain. *Synapse* **2004**, *52*, 283-291.

(13)   Chaki, S.; Funakoshi, T.; Yoshikawa, R.; Okuyama, S.; Okubo, T. et al. Binding characteristics of [H-3]DAA1106, a novel and selective ligand for peripheral benzodiazepine receptors. *European Journal of Pharmacology* **1999**, *371*, 197-204.

(14)   Robinson, R. O.; Ferrie, C. D.; Capra, M.; Maisey, M. N. Positron emission tomography and the central nervous system. *Archives of Disease in Childhood* **1999**, *81*, 263-270.

(15)   Manning, H. C.; Goebel, T.; Marx, J. N.; Bornhop, D. J. Facile, efficient conjugation of a trifunctional lanthanide chelate to a peripheral benzodiazepine receptor ligand. *Organic Letters* **2002**, *4*, 1075-1078.

(16)   Manning, H. C.; Smith, S. M.; Sexton, M.; Haviland, S.; Bai, M. F. et al. A peripheral benzodiazepine receptor targeted agent for in vitro imaging and screening. *Bioconjugate Chemistry* **2006**, *17*, 735-740.

(17)   Achilefu, S.; Dorshow, R. B.; Bugaj, J. E.; Rajagopalan, R. Novel receptor-targeted fluorescent contrast agents for in vivo tumor imaging. *Investigative Radiology* **2000**, *35*, 479-485.

(18)   Ye, Y. P.; Bloch, S.; Kao, J.; Achilefu, S. Multivalent carbocyanine molecular probes: Synthesis and applications. *Bioconjugate Chemistry* **2005**, *16*, 51-61.

(19)   Decaudin, D. Peripheral benzodiazepine receptor and its clinical targeting. *Anti-Cancer Drugs* **2004**, *15*, 737-745.

(20)   Casellas, P.; Galiegue, S.; Basile, A. S. Peripheral benzodiazepine receptors and mitochondrial function. *Neurochemistry International* **2002**, *40*, 475-486.

(21)   Acton, P. D.; Zhou, R. Imaging reporter genes for cell tracking with PET and SPECT. *Quarterly Journal of Nuclear Medicine and Molecular Imaging* **2005**, *49*, 349-360.

(22)   Chemaly, E. R.; Yoneyama, R.; Frangioni, J. V.; Hajjar, R. J. Tracking stem cells in the cardiovascular system. *Trends in Cardiovascular Medicine* **2005**, *15*, 297-302.

(23) Rudelius, M.; Daldrup-Link, H. E.; Heinzmann, U.; Piontek, G.; Settles, M. et al. Highly efficient paramagnetic labelling of embryonic and neuronal stem cells. *European Journal of Nuclear Medicine and Molecular Imaging* **2003**, *30*, 1038-1044.

(24) Shyu, W. C.; Chen, C. P.; Lin, S. Z.; Lee, Y. J.; Li, H. Efficient tracking of non-iron-labeled mesenchymal stem cells with serial MRI in chronic stroke rats. *Stroke* **2007**, *38*, 367-374.

(25) Modo, M.; Cash, D.; Mellodew, K.; Williams, S. C. R.; Fraser, S. E. et al. Tracking transplanted stem cell migration using bifunctional, contrast agent-enhanced, magnetic resonance imaging. *Neuroimage* **2002**, *17*, 803-811.

(26) Modo, M.; Mellodew, K.; Cash, D.; Fraser, S. E.; Meade, T. J. et al. Mapping transplanted stem cell migration after a stroke: a serial, in vivo magnetic resonance imaging study. *Neuroimage* **2004**, *21*, 311-317.

(27) Brekke, C.; Morgan, S. C.; Lowe, A. S.; Meade, T. J.; Price, J. et al. The in vitro effects of a bimodal contrast agent on cellular functions and relaxometry. *Nmr in Biomedicine* **2007**, *20*, 77-89.

(28) Wu, J. C.; Chen, I. Y.; Sundaresan, G.; Min, J. J.; De, A. et al. Molecular imaging of cardiac cell transplantation in living animals using optical bioluminescence and positron emission tomography. *Circulation* **2003**, *108*, 1302-1305.

(29) Frank, J. A.; Miller, B. R.; Arbab, A. S.; Zywicke, H. A.; Jordan, E. K. et al. Clinically applicable labeling of mammalian and stem cells by combining; Superparamagnetic iron oxides and transfection agents. *Radiology* **2003**, *228*, 480-487.

(30) Himes, N.; Min, J. Y.; Lee, R.; Brown, C.; Shea, J. et al. In vivo MRI of embryonic stem cells in a mouse model of myocardial infarction. *Magnetic Resonance in Medicine* **2004**, *52*, 1214-1219.

(31) Rice, H. E.; Hsu, E. W.; Sheng, H. X.; Evenson, D. A.; Freemerman, A. J. et al. Superparamagnetic iron oxide labeling and transplantation of adipose-derived stem cells in middle cerebral artery occlusion-injured mice. *American Journal of Roentgenology* **2007**, *188*, 1101-1108.

(32) Frangioni, J. V.; Hajjar, R. J. In vivo tracking of stem cells for clinical trials in cardiovascular disease. *Circulation* **2004**, *110*, 3378-3383.

(33) San Roman, J. A.; Fernandez-Aviles, F. The role of noninvasive imaging techniques in the assessment of stem cell therapy after acute myocardial infarction. *Nature Clinical Practice Cardiovascular Medicine* **2006**, *3*, S38-S41.

(34)   Lee, D. H.; Kang, S. K.; Lee, R. H.; Ryu, J. M.; Park, H. Y. et al. Effects of peripheral benzodiazepine receptor ligands on proliferation and differentiation of human mesenchymal stem cells. *Journal of Cellular Physiology* **2004**, *198*, 91-99.

(35)   Manning, H. C.; Goebel, T.; Thompson, R. C.; Price, R. R.; Lee, H. et al. Targeted molecular imaging agents for cellular-scale bimodal imaging. *Bioconjugate Chemistry* **2004**, *15*, 1488-1495.

(36)   Manning, H. C.; Bai, M. F.; Anderson, B. M.; Lisiak, R.; Samuelson, L. E. et al. Expeditious synthesis of 'P'-protected macrocycles en route to lanthanide chelate metal complexes. *Tetrahedron Letters* **2005**, *46*, 4707-4710.

(37)   Kovacs, Z.; Sherry, A. D. pH-controlled selective protection of polyaza macrocycles. *Synthesis* **1997**, 759-763.

(38)   Garnier, M.; Dimchev, A. B.; Boujrad, N.; Price, J. M.; Musto, N. A. et al. In-Vitro Reconstitution of a Functional Peripheral-Type Benzodiazepine Receptor from Mouse Leydig Tumor-Cells. *Molecular Pharmacology* **1994**, *45*, 201-211.

(39)   Okubo, T.; Yoshikawa, R.; Chaki, S.; Okuyama, S.; Nakazato, A. Design, synthesis and structure-affinity relationships of aryloxyanilide derivatives as novel peripheral benzodiazepine receptor ligands. *Bioorganic & Medicinal Chemistry* **2004**, *12*, 423-438.

(40)   Zhang, M. R.; Kida, T.; Noguchi, J.; Furutsuka, K.; Maeda, J. et al. [C-11]DAA1106: Radiosynthesis and in vivo binding to peripheral benzodiazepine receptors in mouse brain. *Nuclear Medicine and Biology* **2003**, *30*, 513-519.

(41)   Mahmood, U.; Weissleder, R. Near-infrared optical imaging of proteases in cancer. *Molecular Cancer Therapeutics* **2003**, *2*, 489-496.

(42)   Corrie, J. E. T.; Davis, C. T.; Eccleston, J. F. Chemistry of sulforhodamine-amine conjugates. *Bioconjugate Chemistry* **2001**, *12*, 186-194.

(43)   http://en.wikipedia.org/wiki/Rayleigh_scattering; Wikipedia.

(44)   Bornhop, D. J.; Manning, C. H.; Goebel, T. Preparation of cyclen-based chelates as multi-use multimodal imaging agents. In *PCT Int. Appl.*; WO03020701: U.S., 2003.

CHAPTER V

A TRANSLOCATOR PROTEIN TARGETED CANCER DRUG FOR ENHANCED
THERAPY

5.1 Introduction

One in four deaths in the United States is due to cancer, which makes it one of the

leading causes of death[1]. A total of 559,650 deaths and 1,444,920 new cancer cases for

cancers are projected to occur in the United States in 2007[1]. Cancer is a disease where

abnormal cells divide uncontrollably and form a tumor as their numbers increase[2,3].

Tumors can be benign (non-cancerous) or malignant (cancerous)[3]. Benign tumors can be

removed, do not spread and are rarely a threat to life. Malignant cells invade and destroy

the tissue around them. These cells can also break away from a malignant tumor and

enter the bloodstream or lymphatic system. As a result, cancer cells may spread to distant

anatomic sites to form new tumors. This spread of cancer is called metastasis[3].

Cancer can be treated by surgery, chemotherapy, radiation therapy,

immunotherapy, monoclonal antibody therapy or other

methods[3]. Cytotoxic drugs that target actively

proliferating cells are often used in cancer treatment.

One of the most widely used anticancer drugs is 4'-

demethyl-epipodophyllotoxin 9-[4,6-O-(R)-ethylidene-

beta-D-glucopyranoside], 4' -(dihydrogen phosphate)

(Etoposide, Figure 5.1), which is active against small-

**Figure 5.1. Etoposide
Structure**
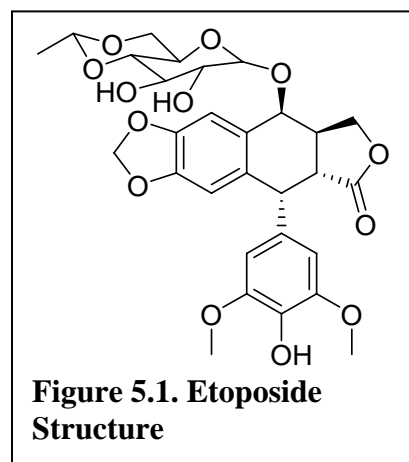
cell lung cancer, testicular cancer, ovarian cancer, breast cancer, gastric cancer, leukemias, rhabdomyosarcomas, neuroblastomas, and lymphomas[4-7].

Etoposide works by inhibiting the DNA topoisomerase II. Type II topoisomerases modulate DNA topology and can cleave the opposing strands of the DNA helix simultaneously[5,6,8]. Once severed, the ends of the DNA are separated, and a second intact DNA duplex is passed through the break. Following passage, the severed DNA is resealed. This double-stranded DNA passage reaction allows topoisomerase II enzymes regulate over- and under-winding of the double helix and resolve nucleic acid knots and tangles. Etoposide poisons these enzymes by stabilizing their covalent DNA cleavage complexes thus preventing the severed DNA from being resealed[5]. The accumulation of DNA cleavage in cell activates the DNA's damage sensors, leading to apoptosis. Some cells depend more heavily upon DNA topoisomerase II for replication than others. Cells that are more dependent upon topoisomerse II for proliferation are better targets for etoposide.

The application of etoposide in cancer therapy is limited as etoposide does not selectively target cancer cells[9]. Instead, etoposide targets any actively proliferating cell that manufactures and utilizes sufficiently high amounts of topoisomerase II. Just as cancer cells actively proliferate, so do many normal cells such as hair follicle cells and certain cells of the gastro-intestinal tract, the reproductive tract, and bone marrow. As a result, etoposide takes effect on these normal cells as well, giving rise to side effects such as nausea, hair loss, myelosuppression, vomiting, and mucositis[6]. A cancer targeted etoposide complex with enhanced selectivity and good efficacy would be more favorable, reducing off-target affects.

Translocator protein (TSPO) is highly expressed in leukemia[10], lymphoma[11] and a variety of cancers[12], such as brain, breast, lung, and prostate cancer. N-(4-chloro-2-phenoxyphenyl)-N-(2-isopropoxybenzyl)acetamide

DAA1106

6-TSPOmbb732

Figure 5.2. Structures of DAA1106 and 6-TSPOmbb732
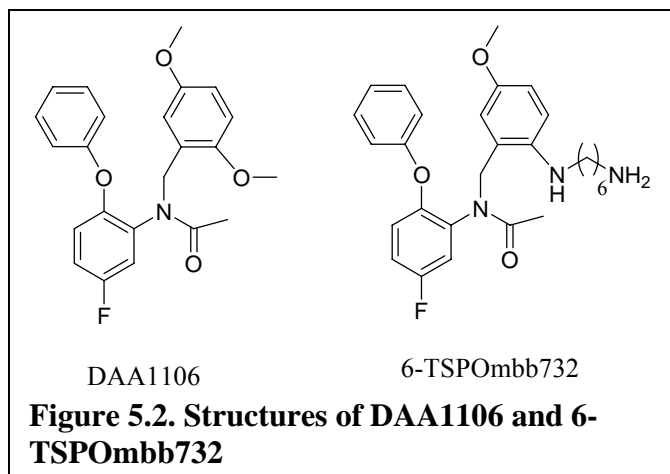
(DAA1106) (Figure 5.2) is a very effective TSPO ligand with picomolar binding affinity[13]. It has been hypothesized that by conjugating etoposide to DAA1106, the resulting molecule would provide a more selective therapy and potentially increase the efficacy of etoposide. Unfortunately, DAA1106 is not easily conjugable. As previously mentioned in Chapter 4, a conjugable analog of DAA1106, 6-TSPOmbb732 (Figure 5.2), was developed for extended TSPO studies. Moreover, several imaging agents based on 6-TSPOmbb732 display nanomolar binding affinities for TSPO and have been successfully used for in vitro imaging (Chapter 4). Due to these promising results, an etoposide-6-TSPOmbb732 conjugate was developed and assessed as a potential targeted cancer drug.

To discover if the etoposide-6-TSPOmbb732 (Et6T) would protect off-target cells while still effectively killing the target cells, the efficacies of etoposide and Et6T were compared in both high and low TSPO expressing cell lines. The high TSPO expressing cells represent the target tumor cells and the low TSPO expressing cells represent the "normal" or control cells. The high TSPO expressing cells used in the first trial were MDA-MB-231 cells, human breast carcinoma cells derived from a pleural effusion metastasis. Jurkat cells (human T-lymphocytes infected with acute T-cell leukemia) were

used as a representative low TSPO cell line. In a second trial, C6 rat glioma cells were used as the high TSPO expressing cell line and IEC-6 normal rat intestinal epithelial cells were used as the low TSPO expressing cell line.

In order to compare the efficacy of etoposide and Et6T in the two cell lines of each trial, the cytotoxicity of each drug in both cell lines was studied by measuring the cell viability at the end of the incubation period.

5.2 Experimental Procedures

5.2.1 Synthesis

2-Bromo-N-(6-(2-((N-(5-fluoro-2-phenoxyphenyl)acetamido)methyl)-4-methoxyphenylamino)hexyl)propanamide (2) A solution of 6-TSPOmbb732 **1** (48 mg, 0.1 mmol) and TEA (14.5 μL, 0.1 mmol) in anhydrous THF (4 mL) was cooled by dry ice/acetone. One equivalent of 2-bromo-propionyl chloride (10.1 μL, 0.1 mmol) was then added and the resulting mixture was allowed to stir for 10 min. Triethyl ammonium hydrochloride salt was filtered through filter paper. Solvent was removed by vacuum rotary evaporation and the product was purified by silica gel column chromatography using 32:1 dichloromethane/methanol as eluent to give **2** as a colorless oil (20 mg, 33%). ^{1}H NMR 300 MHz (CDCl$_3$) δ 7.30-7.26 (m, 2H), 7.10 (t, J = 7.5 Hz, 1H), 6.97-6.91 (m, 1H), 6.84-6.79 (m, 1H), 6.77-6.68 (m, 4H), 6.40 (d, J = 8.7 Hz, 1H), 6.19 (d, J = 2.7 Hz, 1H), 4.93-4.86 (m, 2H), 4.66-4.59 (m, 1H), 4.41 (q, J = 10.5, 3.6 Hz, 1H), 3.60 (s, 3H), 3.27 (q, J = 9.8, 3.2 Hz, 2H), 3.02-2.88 (m, 3H), 1.95 (s, 3H), 1.86 (d, J = 6.9 Hz, 3H), 1.64-1.50 (m, 4H), 1.47-1.31 (m, 4H). MS (ESI)$^+$ [M+H] calcd 614.2, found 614.6.

Etoposide-6-TSPOmbb732 (3) A mixture of etoposide (12 mg, 20 μmol), K_2CO_3 (4 mg, 30 μmol) and 18-crown-6 (1 mg, 4 μmol) in anhydrous acetone (1 mL) was stirred for 5 min under room temperature. A solution of **2** (6 mg, 10 μmol) in anhydrous acetone (300 μL) was added to the mixture and the reaction was heated to reflux with vigorous stirring. After 6 h, the reaction was allowed to cool down to room temperature and the solvent was removed by vacuum rotary evaporation. The residue was partitioned between water (5 mL) and dichloromethane (10 mL). Aqueous layer was extracted with dichloromethane three times (3×10 mL). The organic layers were combined, dried over sodium sulfate and concentrated by vacuum rotary evaporation. The residue was purified by silica gel column chromatography using 3% methanol in dichloromethane as eluent to yield **3** as a colorless oil (5.7 mg, 52%). ^{1}H NMR 300 MHz (CDCl$_3$) δ 7.81 (m, 1H), 7.28 (t, J = 7.2 Hz, 1H), 7.10 (t, J = 7.2 Hz, 1H), 6.95-6.92 (m, 1H), 6.83-6.69 (m, 6H), 6.45 (d, J = 3.2 Hz, 2H), 6.41-6.38 (m, 2H), 6.19 (t, J = 2.4 Hz, 1H), 5.96-5.94 (m, 2H), 4.94-4.85 (m, 3H), 4.72 (q, J = 4.8 Hz, 1H), 4.68-4.47 (m, 4H), 4.25-4.23 (m, 1H), 4.18-4.14 (m, 1H), 3.93 (t, J = 6.8 Hz, 1H), 3.81 (s, 6H), 3.60 (s, 3H), 3.58-3.56 (m, 2H), 3.44 (t, J = 9.2 Hz, 1H), 3.35-3.26 (m, 3H), 3.18-3.13 (m, 2H), 3.00-2.89 (m, 4H), 2.80-2.70 (m, 1H), 1.94-1.92 (m, 3H), 1.60 (s, 3H), 1.58-1.52 (m, 4H), 1.42-1.34 (m, 5H), 1.36 (d, J = 5.2 Hz, 3H). MS (ESI)$^+$ [M+H]$^+$ calcd 1122.5, found 1122.7.

5.2.2 Cytotoxicity Study

Two culture-treated, optical-bottomed, 96-well plates were used for cytotoxicity study. One plate was plated with 10,000 MDA-MB-231 cells per well and the other one was plated with 10,000 Jurkat cells per well. Seven concentrations (10^{-4} M, 10^{-5} M, 10^{-6} M, 10^{-7} M, 10^{-8} M, 10^{-9} M, and 10^{-10} M) of etoposide or Et6T in corresponding media

were prepared. Cells were treated as shown in Figure 5.3. Columns three through nine of rows B,C,D were incubated with increasing concentrations of Et6T and columns three through nine of rows E,F,G were incubated with increasing concentrations of etoposide. Column two, rows B through G served as the control wells and were not treated with any drug. These cells would be treated with the cell viability assay and compared with drug treated cells 72 h after treatment. An additional control (media control) was made in column ten to allow for cell counts following the incubation period. These cells would not be treated with the viability assay.

After the 72 h incubation period, the media control of each cell line was counted so that results could be normalized for cell number. Cells were quantified using a VWR® hemacytometer and trypan blue staining. To quantify cell death induced by drug treatment, cell viability was measured on cells treated with either etoposide or Et6T and compared to the control cells without drug treatment. Cell viability was quanitified using CellTiter-Glo® luminescent cell viability assay (Promega® Corp.). The assay generates luminescent signal in the presence of ATP from viable cells, therefore, photons released are directly proportional to the number of viable cells. The luminescence was then measured using the Xenogen® IVIS® 200 imaging system. The same procedure was used for cytotoxicity study using C6 cells and IEC-6 cells.

5.3 Results and Discussion

The purpose of this study is to develop a TSPO targeted cancer drug with enhanced selectivity and efficacy. An efficient TSPO ligand, 6-TSPOmbb732, was

Scheme 5.1. Synthesis of Etoposide-6-TSPOmbb732
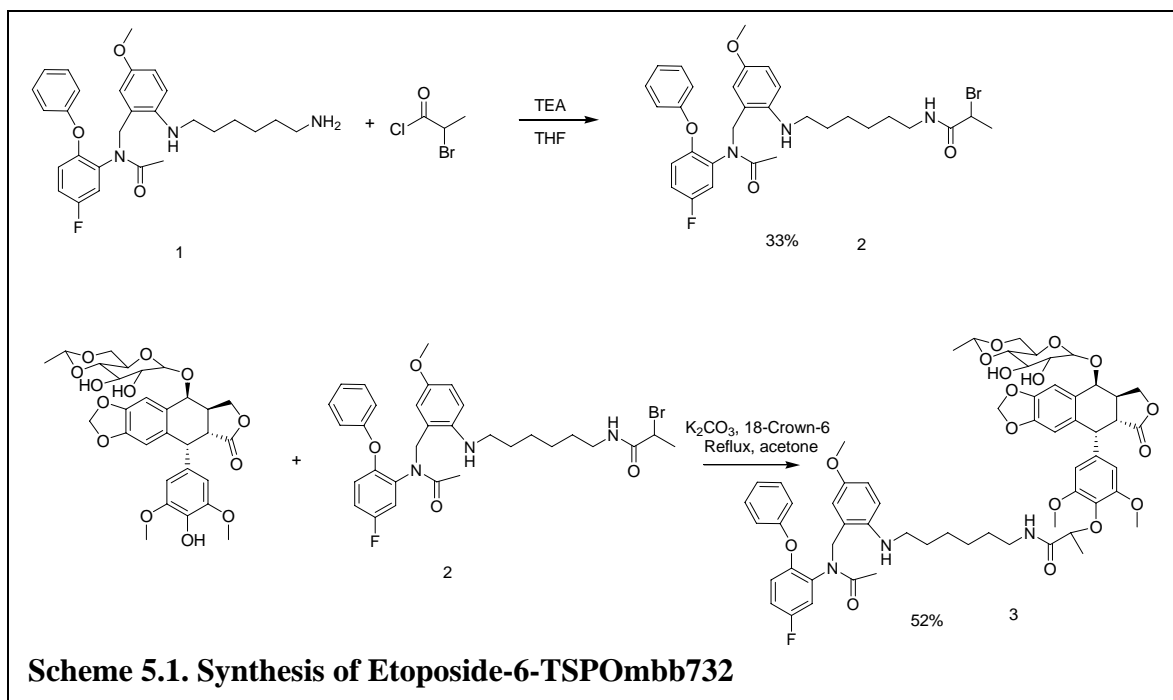
therefore coupled to a commonly used cancer drug, etoposide (Scheme 5.1). The

synthesis involves only two steps. At first, a small linker, 2-bromo-propionyl chloride,

was coupled to 6-TSPOmbb732 by acylation. Second, the phenol group on etoposide was

deprotonated in basic solution and the following alkylation with the 2-bromo-propionyl

group on **2** yielded Et6T. The product was characterized by NMR and MS.

In the first trial of cytotoxicity studies, 10,000 MDA-MB-231 breast cancer cells

or 10,000 Jurkat T-lymphocyte cells were treated with etoposide or Et6T. High TSPO

expressing MDA-MB-231 cells represent cancer cells and low TSPO expressing Jurkat

cells represent normal cells. The density of cells was chosen such that cells would be able

to replicate over the 72 hours incubation period without becoming overly confluent. In

reaching confluent distribution within the well, the cells' natural contact inhibition

mechanisms may negatively affect cell viability. Two groups of cells served as controls.

The first group of cells (column two, rows B through G in Figure 5.3) was not treated

with any drug. These cells were labeled with cell viability assay and compared with etoposide or Et6T treated cells 72 hours after treatment. The other control cells (column ten, rows B through G in Figure 5.3) are media control, and
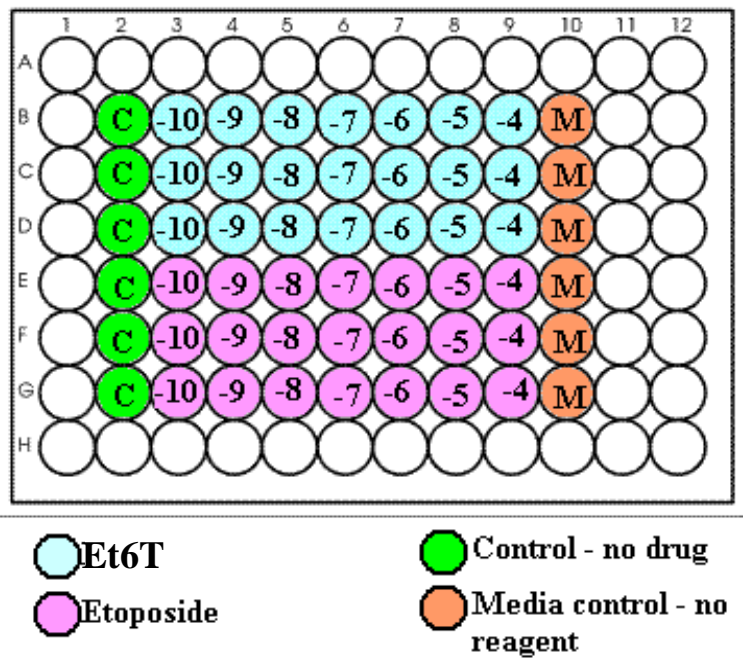

Figure 5.3. Representative image of treatment scheme for the 96 well-plates

were not treated with drug or cell viability assay. These cells were used for cell counting following the incubation period. Three days after non-control cells were treated with etoposide or Et6T, all cells except media control cells were labeled with cell viability assay and the 96-well plates were imaged under IVIS imaging system (Figure 5.4).
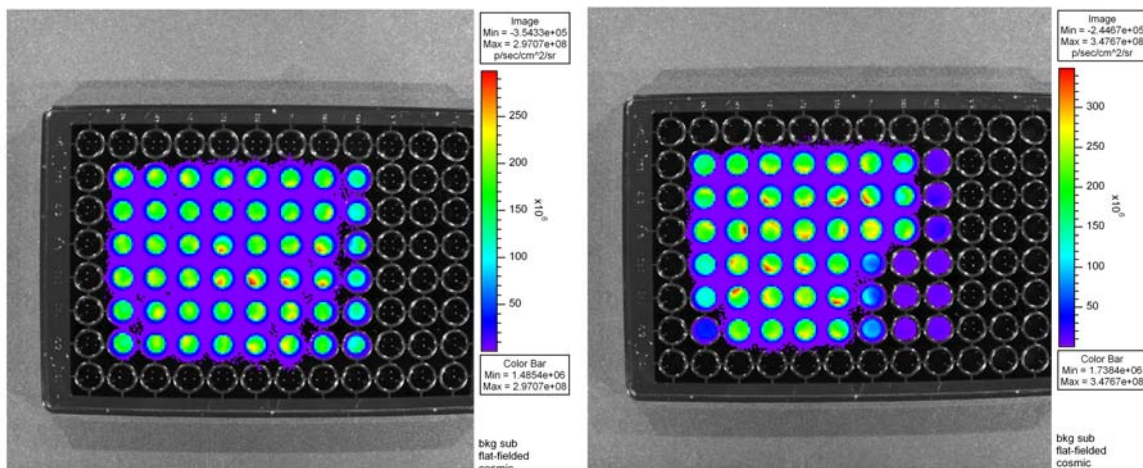

Figure 5.4: Xenogen® IVIS® images of MDA-MB-231 cells (left) and Jurkat cells (right). Higher lumiscent signal (highest = red) indicates more viable cells.

Higher luminescent signal directly corresponds to a greater cell number. Figure 5.4 shows that in the etoposide treated rows on the Jurkat plate, cell death occurred at a lower concentration (10^{-6} M) than Et6T (10^{-4} M) treated rows. On the MDA-MB-231 plate, there does not appear to be a significant difference between the wells dosed with etoposide and the wells dosed with Et6T. Both etoposide and Et6T appear to kill MDA cells at a concentration of 10^{-4} M.

Using LivingImage® software, the data from the IVIS® images was quantified and plotted. Figure 5.5 shows luminescence as percent to the control on the y-axis and drug concentration on the x-axis. Luminescence corresponds to the number of viable cells present at each concentration. At the lowest concentrations (10^{-10} M, 10^{-9} M, 10^{-8} M and 10^{-7} M) of both etoposide and Et6T, the drugs did not cause any significant cell death. Jurkat cells began to respond to etoposide at 10^{-6} M (approximately 60% cell deaths), and
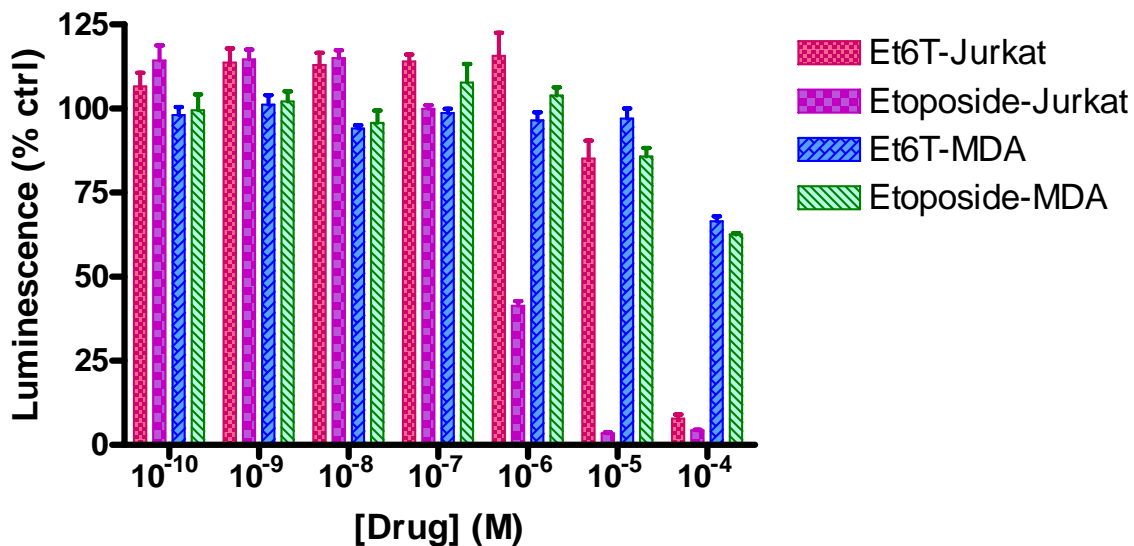

Figure 5.5. Cytotoxicity comparison between Et6T and etoposide on MDA-MB-231 and Jurkat cells

they were effectively responding at 10^{-5} M (approximately 100% cell deaths). However, Jurkat cells effectively respond to Et6T at 10^{-4} M (approximately 100% cell deaths) and no significant cell death was observed at 10^{-5} M. This indicates that Et6T protects the non-target, normal cells. In addition, Figure 5.5 shows that at highest concentration of both etoposide and Et6T, approximately 40% of MDA-MB-231 cells were killed. There does not appear to be a significant difference between the efficacy of etoposide and Et6T in the MDA-MB-231 cells. MDA-MB-231 cells were beginning to respond to etoposide and Et6T at 10^{-4} M. This suggests that Et6T and etoposide have similar efficiency in killing high TSPO expressing MDA-MB-231 cancer cells

Jurkat cells reacted strongly to etoposide due to their upregulated DNA topoisomerase II activity[14]. Since the inhibition of topoisomerase II causes cell death through etoposide treatment, Jurkat cells are good targets for etoposide. This implies that Jurkat cells are not good choices as "normal" cells. On the other hand, Jurkat cells did not respond well to Et6T. This is probably due to minimal expression of TSPO. It appears that Et6T served to protect Jurkat cells from etoposide's inhibition of topoisomerase II. In MDA-MB-231 cells, even though Et6T did not inherently enhance efficacy as expected, it appeared to kill cancer cells with about the same efficacy as etoposide.

To investigate cytotoxicity of etoposide and Et6T in other cells, a second trial using C6 glioma cells (high TSPO expressing) and IEC-6 intestinal epithelial cells (low TSPO expressing) was tested. C6 and IEC-6 were chosen for two reasons. First, the low TSPO expressing control cells in this trial were non-cancerous cells unlike the jurkats, which are leukemia. Second, both C6 and IEC-6 cells are adherent which allows a more uniform bioluminescent signal. In the first trial, MDA-MB-231 cells are adherent
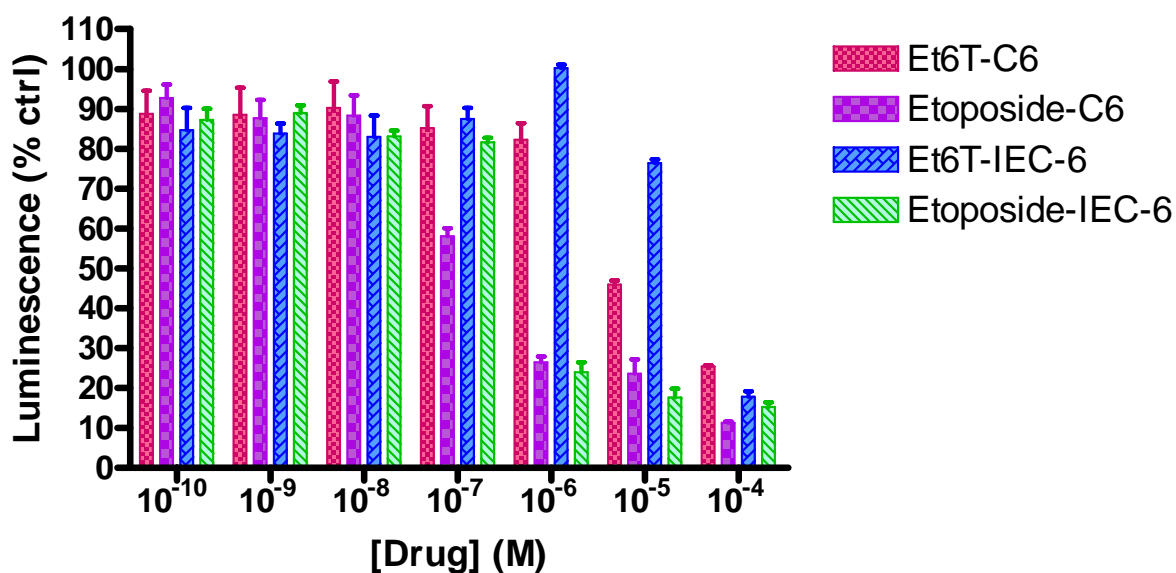
Figure 5.6. Cytotoxicity comparison between Et6T and etoposide on C6 and IEC-6 cells

whereas Jurkat cells are not. It is advantageous to keep adherence property the same for both cell lines.

In the second trial using C6 and IEC-6 cells, etoposide killed both high and low TSPO expressing cell lines at two orders of magnitude lower concentration (10^{-7} M for C6 cells, ~40% cell deaths and 10^{-6} M for IEC-6 cells, ~80% cell deaths) than Et6T (10^{-5} M for C6 cells, ~55% cell deaths and 10^{-4} M for IEC-6 cells, ~80% cell deaths) (Figure 5.6). Unlike in the MDA/Jurkat trial, etoposide and Et6T show significant difference in efficacy. It seems that etoposide is not efficacious in MDA-MB-231 cells, as 10^{-4} M etoposide was needed to take effect on MDA cells whereas only 10^{-7} M etoposide was needed to kill C6 cells. The observed similarity in efficacy on MDA cells between etoposide and Et6T is probably because neither is effective until the largest concentration of drug (10^{-4} M). This indicates that neither etoposide nor Et6T is a good drug for MDA

cells. High concentrations of drug may kill cells through mechanism that does not involve topoisomerase II. For IEC-6 cells, etoposide took effect at 1 μM (about 77% cell deaths) while Et6T took effect at 100 fold higher concentration (100 μM, about 82% cell deaths). The results of this C6/IEC-6 trial show that etoposide began to kill cells at two orders of magnitude lower concentration than Et6T in both high and low PBR cell lines. Et6T appears to protect the IEC-6 cells, but kill C6 cells with lower efficacy. This suggests that Et6T is able to protect normal cells from off-target effects, however, it does not have as good efficacy as etoposide on killing cancer cells.

5.4. Conclusion

In conclusion, we developed a TSPO targeted cancer drug by coupling a TSPO ligand, 6-TSPOmbb732 to a non-selective cancer drug, etoposide. Cytotoxicity of etoposide and the TSPO targeted drug, Et6T were compared in high TSPO expressing cancer cells and low TSPO expressing control cells. In the first trial using MDA-MB-231 cancer cells and Jurkat control cells, Et6T appeared to protect Jurkat cells and had similar efficacy as etoposide in killing MDA-MB-231 cancer cells. However, neither etoposide nor Et6T was effective in treating MDA cells until reaching the largest concentration (100 μM). In the second trial using C6 glioma cells and IEC-6 normal epithelial cells, etoposide started killing cells at two orders of magnitude lower concentration than Et6T in both cell lines. Overall, even though Et6T does not appear to increase efficacy in cancer treatment compared to etoposide, it seems to protect low TSPO expressing control cells from off-target effects.

5.5 Acknowledgements

5.6 References

(1)   Jemal, A.; Siegel, R.; Ward, E.; Murray, T.; Xu, J. Q. et al. Cancer statistics, 2007. *Ca-a Cancer Journal for Clinicians* **2007**, *57*, 43-66.

(2)   http://www.who.int/mediacentre/factsheets/fs297/en/; World Health Organization.

(3)   http://en.wikipedia.org/wiki/Cancer; Wikipedia.

(4)   Slevin, M. L.; Clark, P. I.; Joel, S. P.; Malik, S.; Osborne, R. J. et al. A Randomized Trial to Evaluate the Effect of Schedule on the Activity of Etoposide in Small-Cell Lung-Cancer. *Journal of Clinical Oncology* **1989**, *7*, 1333-1340.

(5)   Hasinoff, B. B.; Chee, G. L.; Day, B. W.; Avor, K. S.; Barnabe, N. et al. Synthesis and biological activity of a photoaffinity etoposide probe. *Bioorganic & Medicinal Chemistry* **2001**, *9*, 1765-1771.

(6)   Hande, K. R. Etoposide: Four decades of development of a topoisomerase II inhibitor. *European Journal of Cancer* **1998**, *34*, 1514-1521.

(7)   Felix, C. A. Leukemias related to treatment with DNA topoisomerase II inhibitors. *Medical and Pediatric Oncology* **2001**, *36*, 525-535.

(8)   Champoux, J. J. DNA topoisomerases: Structure, function, and mechanism. *Annual Review of Biochemistry* **2001**, *70*, 369-413.

(9)   Schmidt, F.; Monneret, A. C. Prodrug Mono Therapy: Synthesis and biological evaluation of an etoposide glucuronide-prodrug. *Bioorganic & Medicinal Chemistry* **2003**, *11*, 2277-2283.

(10)   Ishiguro, K.; Taft, W. C.; Delorenzo, R. J.; Sartorelli, A. C. The Role of Benzodiazepine Receptors in the Induction of Differentiation of Hl-60 Leukemia-Cells by Benzodiazepines and Purines. *Journal of Cellular Physiology* **1987**, *131*, 226-234.

(11)   Alexander, B. E. E.; Roller, E.; Klotz, U. Characterization of Peripheral-Type Benzodiazepine Binding-Sites on Human-Lymphocytes and Lymphoma Cell-Lines and Their Role in Cell-Growth. *Biochemical Pharmacology* **1992**, *44*, 269-274.

(12)   Decaudin, D.; Castedo, M.; Nemati, F.; Beurdeley-Thomas, A.; De Pinieux, G. et al. Peripheral benzodiazepine receptor ligands reverse apoptosis resistance of cancer cells in vitro and in vivo. *Cancer Research* **2002**, *62*, 1388-1393.

(13)   Culty, M.; Silver, P.; Nakazato, A.; Gazouli, M.; Li, H. et al. Peripheral benzodiazepine receptor binding properties and effects on steroid synthesis of two new phenoxyphenyl-acetamide derivatives, DAA1097 and DAA1106. *Drug Development Research* **2001**, *52*, 475-484.

(14)   Padget, K.; Pearson, A. D. J.; Austin, C. A. Quantitation of DNA topoisomerase II alpha and beta in human leukaemia cells by immunoblotting. *Leukemia* **2000**, *14*, 1997-2005.

MBC94, A NOVEL CONJUGABLE CANNABINOID CB$_2$ RECEPTOR LIGAND

6.1 Introduction

Cannabinoid receptors are 7-transmembrance domain G protein-coupled receptors (GPCR) and located on cell membrances[1,2]. To date, two distinct cannabinoid receptors have been identified, including CB$_1$ and CB$_2$ receptors[3,4]. The CB$_1$ receptor is expressed primarily in the central nervous system whereas the CB$_2$ receptor is expressed predominantly in tissues of the immune system, such as the spleen, tonsils and thymus[5,6]. The two receptors share an overall 44% homology, however, within the transmembrane domains of CB$_1$ and CB$_2$, 68% of their amino acid sequence is identical[4].

Although the exact functional role of CB$_2$ is still not clear, the receptor seems to be involved in signal transduction in the immune system[7] and mediates immunosuppressive and immunostimulatory effects[8-10]. The CB$_2$ receptor is only highly expressed in immune cells while the expression in other cells is low, which makes this receptor a particularly attractive target for immune system imaging and therapy[6]. The CB$_2$ receptor is undetectable in thyroid, retina, placenta, skeletal muscle, kidney, liver, brain, cerebellum, cortex, pituitary gland, adrenal gland, heart, protate and ovary[6]. This provides great opportunities in imaging with low background and therapy with reduced side effects. The CB$_2$ receptor has become an interesting target for drug development aiming at treatment of pain[11,12], inflammation[13], osteoporosis[14], malignant gliomas[15], tumors of immune origin[16], and immunological disorders[17].

Together with the characterization of the CB$_2$ receptor, a considerable effort has been carried out to identify or develop CB$_2$ receptor ligands. The term cannabinoid was first used to describe terpenophenolic compounds in *Cannabis Sativa* L., among which (-)-trans-Δ^9-tetrahydrocanabinol (Δ^9-THC) was shown to be the active constituent[18]. Many immunological effects

Anandamide

2-Arachidonyl-glycerol (2-AG)

Figure 6.1. Structures of endogenous CB$_2$ receptor ligands

of Δ^9-THC have been discovered, including anti-inflammatory effect, inhibiting production of tumor necrosis factor-α, interleukin-2 and nitric oxide from macrophages and T cells, and induction of arachidonic acid release[13]. CB$_2$ receptor ligands can be divided into two groups: endogenous and exogenous ligands. Two endogenous CB$_2$ receptor agonists are known (Figure 6.1), including arachidonoylethanolamide (anandamide)[19] and 2-arachidonoyl glycerol (2-AG)[20,21]. Both molecules have marginally greater CB$_1$ than CB$_2$ affinity[22]. Even though 2-AG acts as a full CB$_1$ and CB$_2$ receptor agonist, anandamide acts as a partial agonist (showing mixed agonist-antagonist properties) toward these receptors[21]. Many exogenous CB$_2$ receptor ligands have been discovered as well, such as Δ^9-THC, HU-210, CP55940, WIN55212-2, AM630 and SR 144528 (Figure 6.2). Δ^9- THC, HU-210, CP55940, WIN55212-2 are canabinoid receptor agonists with no or marginal CB$_1$- or CB$_2$ selectivity[22]. AM630 and SR 144528 are both selective CB$_2$ receptor ligands and behave as inverse agonists rather than as "silent"
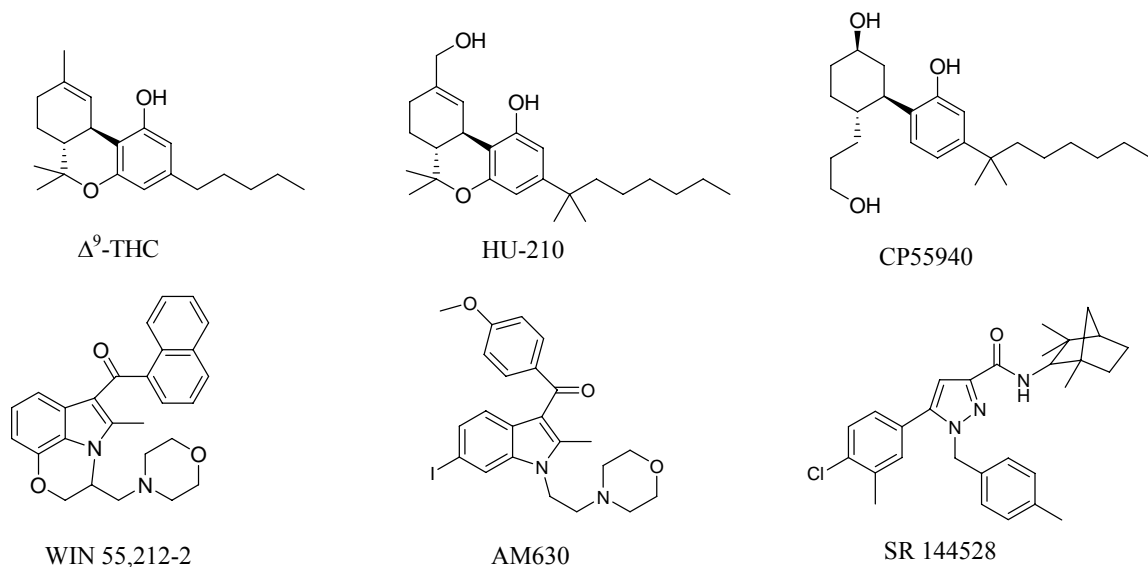
Δ^9-THC HU-210 CP55940

WIN 55,212-2 AM630 SR 144528
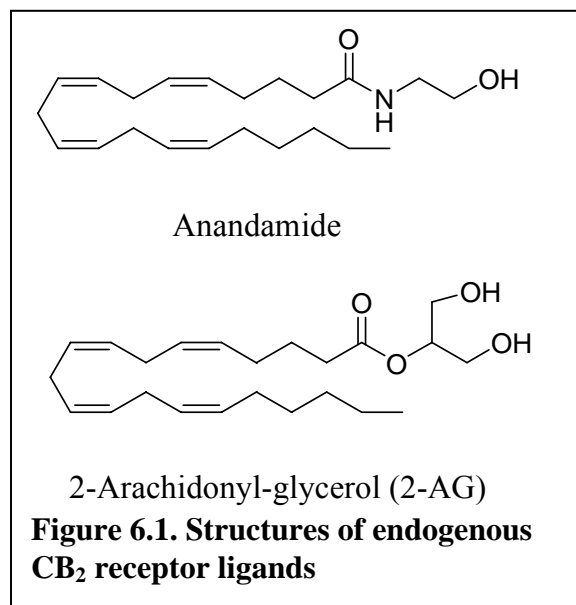
Figure 6.2. Structures of exogenous CB$_2$ receptor ligands

antagonists. The CB$_2$/CB$_1$ affinity ratio is less for AM630 (CB$_2$/CB$_1$ affinity =165) than

for SR 144528 (CB$_2$/CB$_1$ affinity >700)[22]. SR 144528 has been widely used as a

pharmacological tool for recognizing CB$_2$ receptor-mediated effects[22].

Even though SR 144528 has been extensively used to characterize CB$_2$

receptors[1,22-26], the application of SR 144528 in CB$_2$ receptor targeted imaging is limited

as SR 144528 is not conjugable. In other words, signaling moieties, such as fluorescent

dyes, lanthanide chelates and nanoparticles, can not be easily coupled to SR 144528. To

further study CB$_2$ receptor and related diseases, development of a conjugable SR 144528

analog seems to be a reasonable strategy.

In the current study, we synthesized a conjugable SR 144528 analog, mbc94. To

our knowledge, this is the only fully conjugable CB$_2$ receptor ligand in existence, which

has a terminal amino group, allowing easy conjugation to other molecules. It is expected

that by coupling signaling moieties to SR 144528, the molecule can provide opportunities

in CB$_2$ receptor targeted disease imaging. A near infrared (NIR) dye, IRDye^{TM} 800CW

148

NHS ester, was selected to label mbc94 for optical imaging. Both mbc94 and the NIR dye labeled mbc94 (NIRmbc94) bind to CB_2 receptor with nanomolar binding affinities. Preliminary live cell imaging showed that NIRmbc94 labeled CB_2 receptor expressing cells.

<div align="center">6.2 Experimental Procedures</div>

6.2.1 Synthesis

Compound **3** was prepared from 4'-chloro-3'methylacetophenone and diethyl oxalate as previously described[27]. Formation of pyrazoles **4** and **5** were achieved by following literature procedures[28]. Fenchylamine **8** was prepared by converting fenchone to a formamide **7**, followed by hydrolysis of the amide bond as previously described[29].

5-(4-chloro-3-methylphenyl)-N-(1,3,3-trimethylbicyclo[2.2.1]heptan-2-yl)-1H-pyrazole-3-carboxamide (9). A mixture of **5** (237 mg, 1 mmol), 2-(1H-Benzotriazole-1-yl)-1,1,3,3-tetramethyl uronium hexafluorophosphate (HBTU) (417 mg, 1.1 mmol), and 1-Hydroxybenzotriazole (HOBT) (135 mg, 1 mmol) in 50/50 dichloromethane/DMF (10 mL) was stirred at RT for 5 min. DIEA (248 µL, 1.5 mmol) was added and the resulting mixture was stirred for another 10 min. A solution of **8** in 50/50 dichloromethane/DMF (10 mL) was then added to the mixture and the reaction mixture was stirred for another 2 h. The reaction solution was concentrated by vacuum rotary evaporation and purified with silica gel column chromatography eluted with 100% hexanes to 1:7 ethyl acetate/hexanes. Compound **9** was collected as a white solid (314 mg, 84%). ^{1}H NMR 400 MHz (CDCl3) δ 7.51 (s, 1H), 7.42 (s, 1H), 6.97 (s, 1H), 6.76 (bs, 1H), 3.84 (d, J = 9.6 Hz, 1H), 2.43 (s, 3H), 1.81 (d, J = 3.6 Hz, 1H), 1.73 (d, J = 10.8 Hz, 2H), 1.50-1.41

(m, 2H), 1.29-1.26 (m, 2H), 1.18 (s, 3H), 1.11 (s, 3H), 0.88 (s, 3H); MS (ESI)$^+$ [M+Na]$^+$ calcd 394.2, found 394.4.

1-(4-(bromomethyl)benzyl)-5-(4-chloro-3-methylphenyl)-N-(1,3,3-trimethylbicyclo[2.2.1]heptan-2-yl)-1H-pyrazole-3-carboxamide (10) NaH (60% in mineral oil, 14.4 mg, 0.36 mmol) was added to a solution of **9** (111.6 mg, 0.3 mmol) in anhydrous toluene (30 mL) at room temperature. The mixture was heated at 70 °C for one hour and then cooled to room temperature. αα-Dibromo-p-xylene (791.9 mg, 3 mmol) was added and the resulting mixture was refluxed for 20 h. The reaction solution was then concentrated by vacuum rotary evaporation and the crude mixture was purified by column chromatography (silica gel) using gradient 100% hexanes to 1:9 ethyl acetate/hexanes as eluent. Compound **10** was collected as an colorless oil (131.9 mg, 79%). ^{1}H NMR 400 MHz (CDCl3) δ 7.28 (s, 1H), 7.19 (s, 1H), 7.02 (s, 1H), 6.94 (d, J = 7.6 Hz, 4H), 6.77 (s, 1H), 5.24 (s, 2H), 4.40 (s, 2H), 3.75 (d, J = 9.6 Hz, 1H), 2.26 (s, 3H), 1.73 (s, 1H), 1.65 (d, J = 10.0 Hz, 2H), 1.43-1.34 (m, 2H), 1.20-1.45 (m, 2H), 1.10 (s, 3H), 1.04 (s, 3H), 0.80 (s, 3H); MS (ESI)$^+$ [M+Na]$^+$ calcd 578.1, found 578.2.

Mbc94 (11) A solution of **10** (22.2 mg, 40 μmol) in dichloromethane (5 mL) was added dropwise to a stirring solution of 1,6-hexane diamine (93 mg, 0.8 mmol) in dichloromethane (5 mL). The resulting mixture was stirred at room temperature for 5 h. The solution was then concentrated by rotary evaporation and chromatographed on a silica gel column using gradient 100% dichloromethane to 8:1:0.1 dichloromethane/methanol/ammonia as eluent. Mbc94 was collected as a pale yellow oil (19 mg, 70%). ^{1}H NMR 400 MHz (CDCl3) δ 7.33 (d, J = 8.0 Hz, 1H), 7.26 (d, J = 8.0 Hz, 2H), 7.11 (d, J = 1.6 Hz, 1H), 7.04-6.99 (m, 4H), 6.83 (s, 1H), 5.30 (s, 2H), 3.81 (dd, J =

9.6, 1.6 Hz, 1H), 3.76 (s, 2H), 2.68 (t, J = 2.4 Hz, 2H), 2.61 (t, J = 7.2 Hz, 2H), 2.32 (s, 3H), 1.79-1.78 (m, 1H), 1.72-1.70 (m, 5H), 1.53-1.41 (m, 6H), 1.34-1.30 (m, 4H), 1.26-1.21 (m, 2H), 1.16 (s, 3H), 1.11 (s, 3H), 0.86 (s, 3H); MS (ESI)$^+$ [M+H]$^+$ calcd 590.3, found 590.3.

NIRmbc94 A mixture of mbc94 (5 mg, 8.5 μmol) and IRDye^{TM} 800CW NHS ester (5 mg, 4.3 μmol) in DMSO (7 mL) was stirred under argon at room temperature overnight. HPLC analysis was performed to monitor the reaction on a Varian Polaris C-18 column (250 × 4.6 mm) at a flow rate of 0.8 mL/min. Flow A was 0.1% TEA in water and flow B was 0.1% TEA in acetonitrile. The elution method for analytical HPLC started with a linear gradient from 100% to 80% A over 30 min, then from 80% to 50% A for 5 min, arrived at 20% A in another 3 min, held at 20% A for 10 min, and finally returned to 100% A over 1 min. The elution profile was monitored by UV absorbance at 254 and 780 nm. Product was purified by preparative HPLC using a Varian Polaris C-18 column (250 × 21.2 mm) at 17 mL/min. The collected solution was concentrated by vacuum rotary evaporation and frozen to -78ºC. The solvent (mostly water) was then removed via lyophilization. The amount of NIRmbc94 was determined by absorption in DMSO solution at 780 nm (3.0 mg, 44%). ^{1}H NMR 400 MHz (MeOD) δ 8.02 (d, J = 14.4 Hz, 1H), 7.89-7.78 (m, 5H), 7.74 (d, J = 1.2 Hz, 1H), 7.48 (d, J = 8.0 Hz, 2H), 7.34-7.32 (m, 4H), 7.24 (d, J = 8.4 Hz, 1H), 7.20-7.17 (m, 3H), 7.09 (d, J = 8.0 Hz, 2H), 6.84 (s, 1H), 6.33 (d, J = 14.0 Hz, 1H), 6.14 (d, J = 14.0 Hz, 1H), 5.49 (s, 2H), 4.20-4.15 (m, 4H), 4.09 (t, J = 2.4 Hz, 2H), 3.76 (dd, J = 9.2, 1.2 Hz, 1H), 3.01-2.93 (m, 4H), 2.89 (t, J = 2.8 Hz, 2H), 2.80 (t, J = 5.6 Hz, 2H), 2.74 (t, J = 5.6 Hz, 2H), 2.34 (s, 3H), 2.11 (t, J = 6.8 Hz, 2H), 2.05-2.02 (m, 2H), 1.95-1.92 (m, 5H), 1.79-1.71 (m, 6H), 1.64-1.49 (m, 8H),

1.40 (s, 6H), 1.34 (s, 6H), 1.25-1.21 (m, 7H), 1.15 (s, 3H), 1.08 (s, 3H), 0.92-0.86 (m, 2H), 0.85 (s, 3H). MS (ESI)⁻ [M-H]⁻ calcd 1572.6, found 1572.5.

6.2.2 Satruation Binding Study

Wild-type and 2D4 DBT cells were expanded in DMEM containing Glutamax™, D-glucose (4.5g/l) and sodium pyruvate (110 mg/ml) (Invitrogen/Gibco 10569), and supplemented with FBS (10%), HEPES (10 mM), $NaHCO_3$ (5 mM), penicillin (100 U/ml) and streptomycin (100 μg/ml). Ninety-six well plates were thinly-coated with collagen Type I (2.5 μg/ml, 30 min, BD Bioscience #354236) diluted in acetic acid (0.02 N) in sterile H_2O. Wells were subsequently rinsed three times with PBS and allowed to air dry in a cell incubator at 37 ºC.

The cells were seeded in 96 well plates with an optical bottom polymer (NUNC®) at 4 x 10^4 cells *per* 200 µL of DMEM (same DMEM as above) *per* well. Twenty-four h later, cells typically reached a density of 80% confluence. The media was then replaced by DMEM + FBS (1%, 100 µL) containing NIRmbc94 and incubated at 37 ºC for 30 min. The cells were rinsed twice with DMEM + FBS (1%, 100 µL) to remove unbound NIRmbc94.

Fluorescence at 800 nm was then immediately quantified with a Li-Cor Odyssey® Infrared Imaging System. The values for non-specific binding (wild-type DBT cells) were subtracted from the total binding values (2D4 DBT cells) with data expressed in terms of relative fluorescence units (RFU), analyzed by Scatchard analysis, and calculated by nonlinear regression using Graph Pad Prism® software (GraphPad Prism®, San Diego, CA, USA).

6.2.3 Competitive Binding Study

DBT cells expressing CB_2 receptor were expanded in 10 mm dishes. Once at confluence, cells were rinsed once with PBS and frozen without supernatant. Cells were then lysed in Tris-EDTA-$MgCl_2$ buffer (50 mM, 1 mM and 3 mM; pH 7.4; buffer A), homogenized using a polytron homogenizer and centrifuged at 14,000 g (20 min, 4 ºC). Pellets were resuspended in buffer A and centrifuged at 14,000 g (20 min, 4 ºC). Saturations and binding experiments were performed using silanized tubes and pipettes tips. Homogenates (50 μg of proteins in 150 μL of buffer A containing 1% FFA-BSA) were added to tubes containing either 0.2 μL of drug in DMSO or DMSO alone (0.1%, total binding), and 50 μL of [^{3}H]-CP-55,940 (3 nM final concentration). Non-specific binding was determined in the presence of 10 μM CP-55,940. Tubes were incubated for 1 h in a shaking water bath at 30 ºC. Cold buffer was rapidly added to the tubes, solutions filtered through pre-soaked glass-fibers filters (Whatman GF/B) using a Brandell harvester (Gaithersburg, MD) and tubes rinsed twice using cold buffer. Radioactivity on the filter was counted using 10 mL of Ecoscint scintillation liquid following 10 s of agitation and 3 h resting. K_i values were calculated from the IC50 values using the Cheng-Prusoff equation[30] yielding K_d and B_{max} values of 3.1 nM and 6 pmol/mg, respectively.

6.2.4 Cell Imaging

CB_2 expressing DBT (2D4) cells in MaTek dishes were incubated with 5 μM NIRmbc94 or 5 μM free NIR dye in culture media for 30 min. Cells were rinsed and re-incubated with saline before imaging using a Nikon epifluorescence microscope equipped with a Hamamatsu C4742-98 camera, Nikon Plan Apo 60x/1.40 oil objective, a mercury

lamp, an ICG filter set, a Texas Red filter set, and a FITC filter set (Figure 6.5).
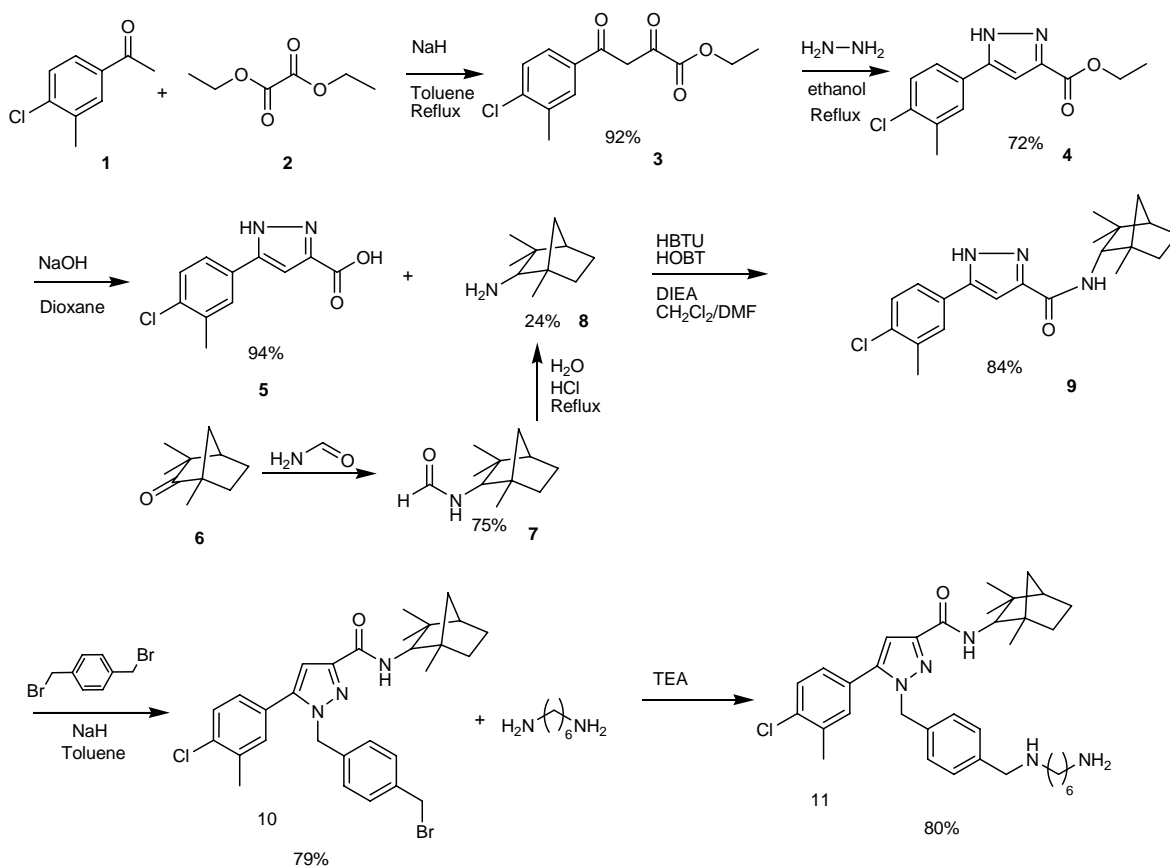
Scheme 6.1. Synthesis of mbc94

6.3 Results and Discussion

The synthetic pathway of the conjugable SR 144528 analog, mbc94 is shown in Scheme 6.1. Compound **3**[27], **5**[28], **7**[29] and **8**[29] were prepared as reported. Compound **9** was prepared using thionyl chloride before, but the yield was relatively low (70%)[28]. We synthesized **9** by regular peptide coupling using 2-(1H-Benzotriazole-1-yl)-1,1,3,3-tetramethyl uronium hexafluorophosphate (HBTU) and the yield was improved to 84%. The following N-alkylation with αα-Dibromo-p-xylene produced **10** and another N-alkylation with 1,6-hexane diamine yielded the conjugable CB_2 receptor ligand, mbc94.

The use of near-infrared (NIR) light in molecular imaging has gained increasing
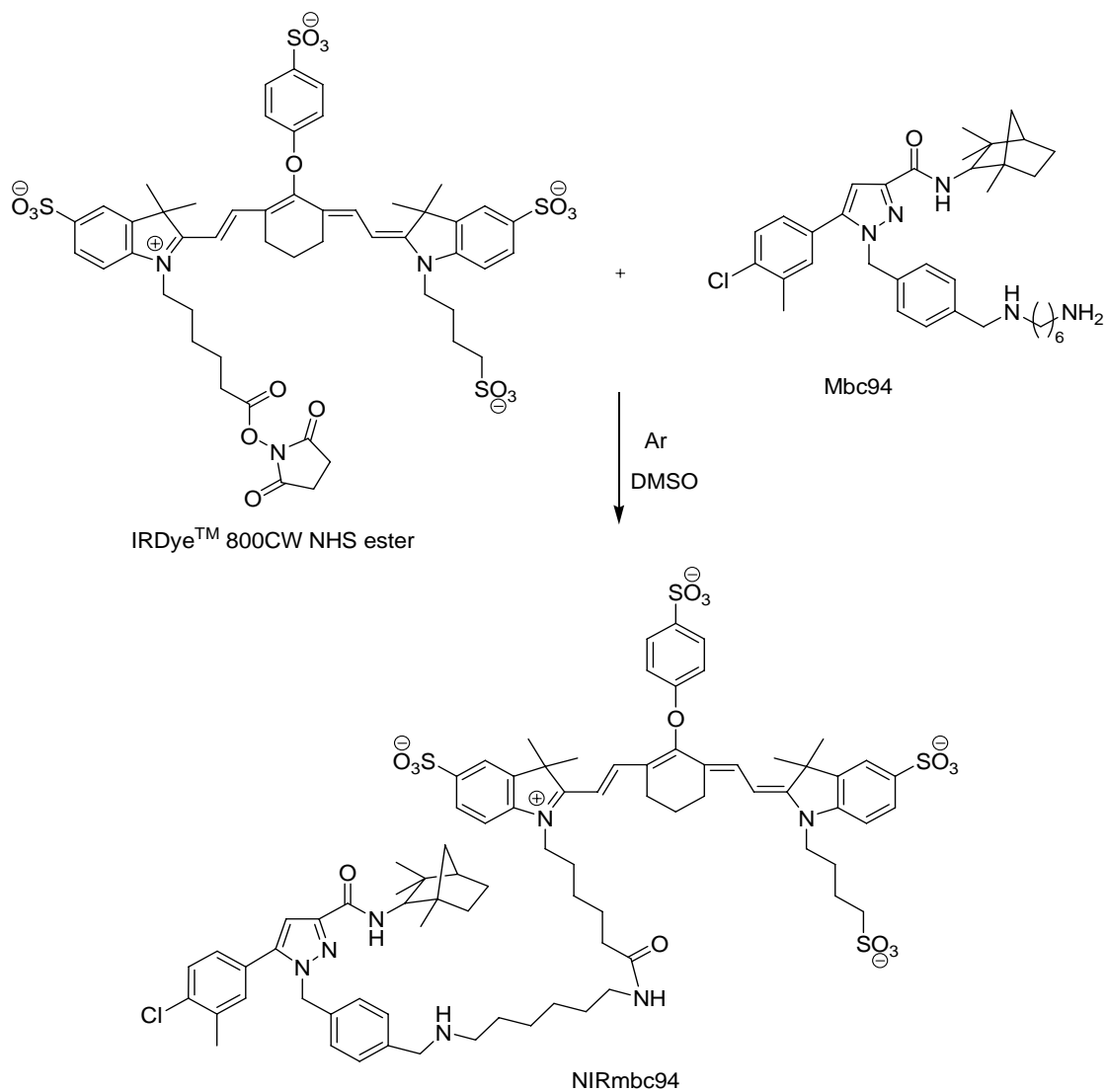
Scheme 6.2. Synthesis of NIRmbc94

interest during recent years. In the NIR region (650-900 nm), tissues are relatively

transparent because hemoglobin, water and lipids exhibits relatively low absorption

coefficients[31]. Therefore, we labeled mbc94 with a NIR dye, IRDye™ 800CW NHS

ester for NIR optical imaging. The reaction was monitored by analytical HPLC at 780 nm

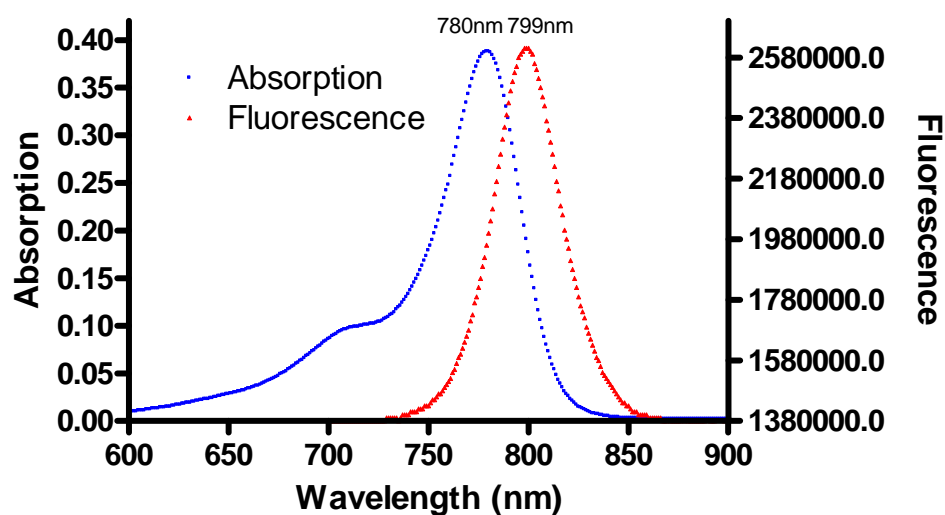and the product, IRDye™ 800CW-mbc94 (NIRmbc94), was purified using a semi

Figure 6.3. NIRmbc94 absorption and fluorescence

preparative HPLC and characterized by NMR and mass spectrometry. The absorption and emission spectra were then taken (Figure 6.3). NIRmbc94 has maximum absorption at 780 nm and emission at 799 nm (methanol), which are in the NIR spectral region which would allow deep tissue emission for enhanced in vivo imaging.

A competitive binding study was performed on mbc94 and NIRmbc94 to test their ability to displace the binding of [^{3}H]-CP-55,940 (a CB_2 ligand) to DBT cells membrane fractions that stably express mouse CB_2 receptors (Figure 6.4). SR 144528 was found to have a K_i of 0.7 nM, which is in agreement with the literature value (K_i = 0.6 nM)[32]. Mbc94 had a K_i of 15 nM and NIRmbc94 had a K_i of 120 nM. Though lower than the binding affinity of SR144528, the nanomolar binding affinities of mbc94 and NIRmbc94 is rather high, making them promising CB_2 receptor ligands.

NIRmbc94 was then tested for its ability to specifically label intact CB_2-expressing DBT cells in culture. Total binding was determined in CB_2-expressing DBT
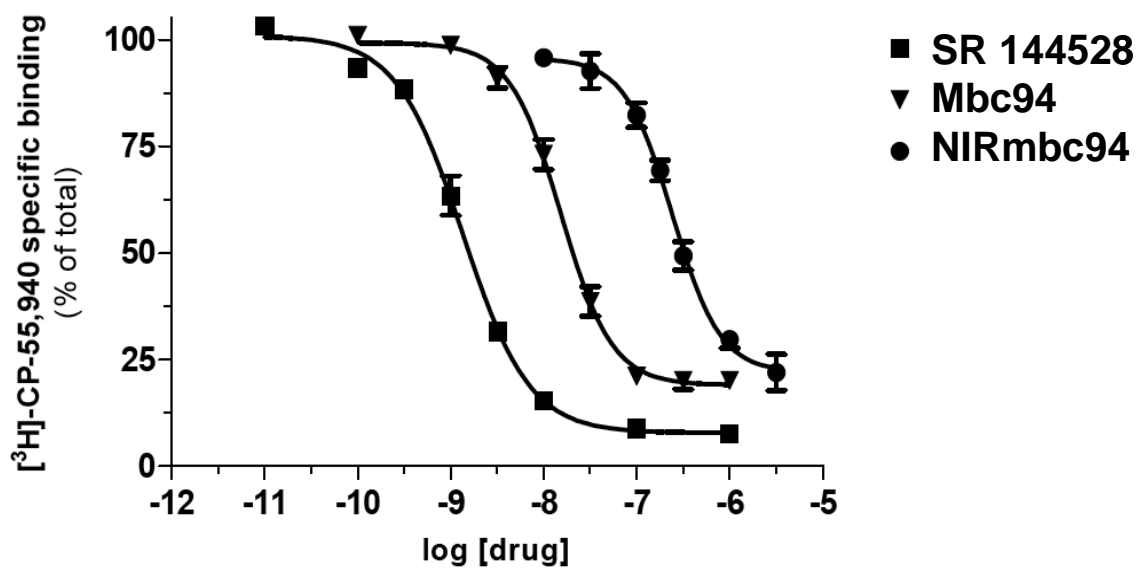
156

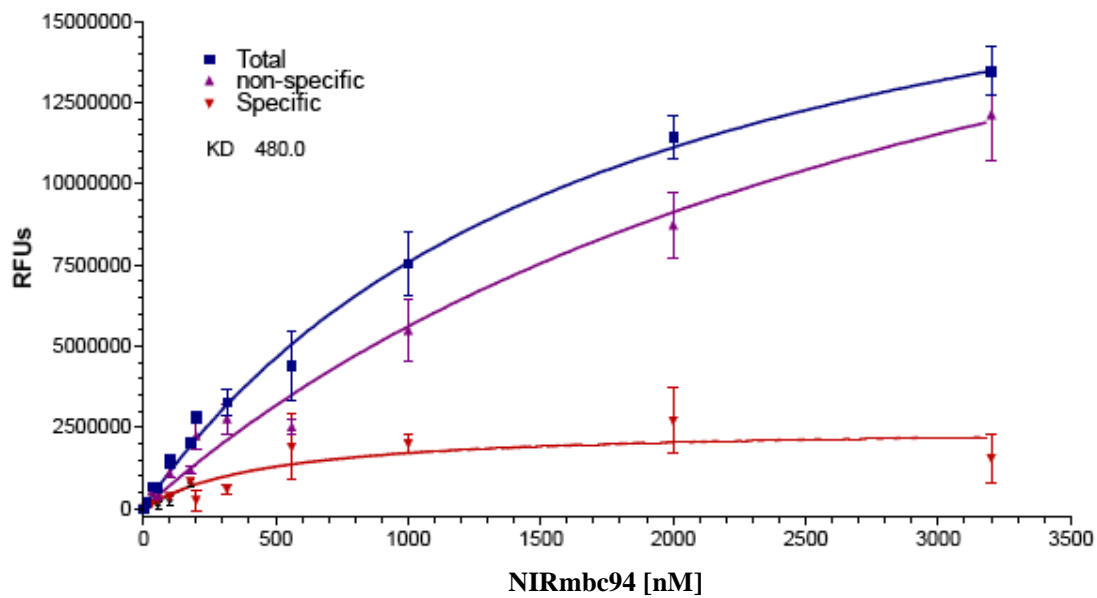**Figure 6.4. Competitive binding study of mbc94 and NIRmbc94**

Figure 6.5. Saturation binding study of NIRmbc94

cells and non-specific binding was determined in wild-type DBT cells, which are devoid

of CB_2 receptors. Figure 6.5 shows that CB_2-expressing DBT cells had significantly

higher fluorescence signal than wild-type DBT cells. In addition, it was found NIRmbc94

binds to CB_2 receptors with nanomolar affinity ($K_d = 480$ nM, Figure 6.5). These facts

indicate that NIRmbc94 binds specifically to CB_2-expressing DBT cells.

Fluorescence microscopy imaging was performed to study the cellular uptake of

NIRmbc94 in CB_2 receptor expressing DBT cells (Figure 6.6). Cells labeled with 5 µM

NIRmbc94 showed significant fluorescence signal (S/N=1.6) whereas cells labeled with

the same concentration of free dye (IRDye^{TM} 800CW acid) did not give significant
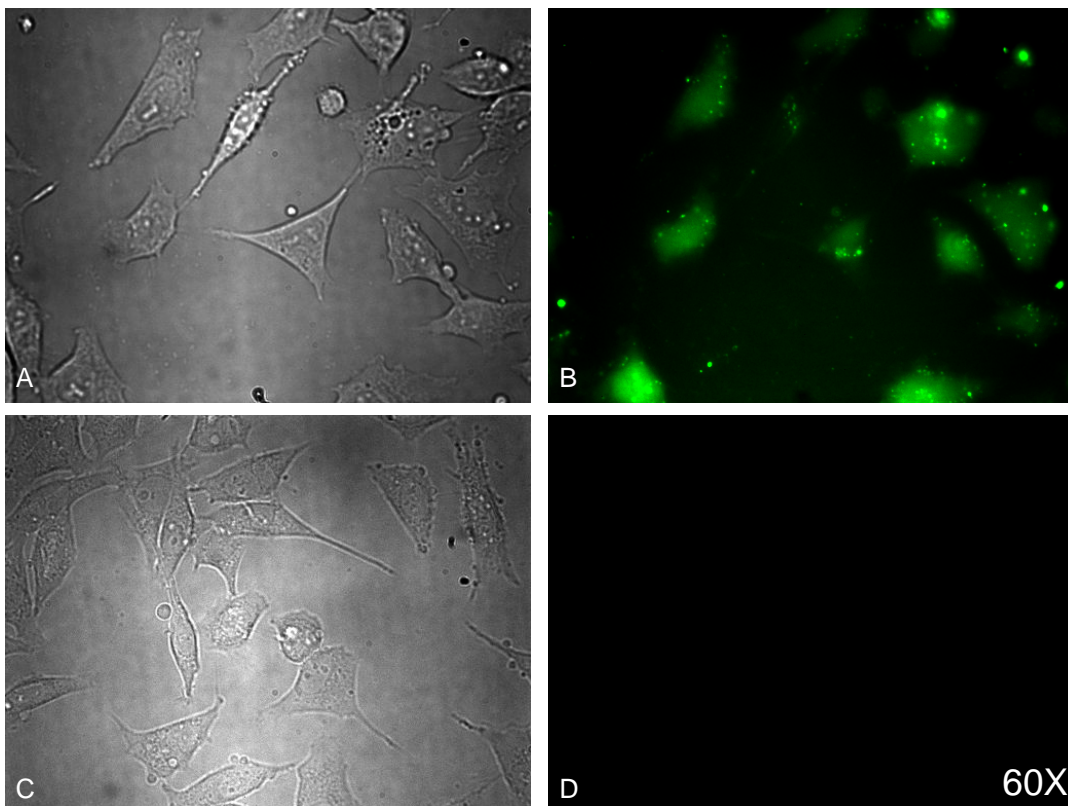

Figure 6.6. Fluorescence imaging of DBT cells incubated with NIRmbc94 or free NIR dye: (A) Phase contrast microscopy of cells dosed with NIRmbc94; (B) fluorescence imaging of cells dosed with 5 µM NIRmbc94; (C) Phase contrast microscopy of cells dosed with free NIR dye; (D) fluorescence imaging of cells dosed with 5 µM free NIR dye (control).

fluorescence signal.

6.4 Conclusion

In conclusion, we developed a conjugable CB_2 receptor ligand, mbc94, which has nanomolar binding affinity (K_i = 15 nM) for CB_2 receptors. Mbc94 has a terminal amino group, making it universally conjugable. A NIR dye labeled mbc94, NIRmbc94, was found to displace a known CB_2 ligand, $[^3H]$-CP-55,940 from CB_2 receptors (K_i = 120 nM). In addition, saturation binding studies indicated that CB_2-expressing DBT cells labeled significantly more NIRmbc94 than low-CB_2 expressing wild-type DBT cells (K_d = 480 nM). Finally, to a much greater extent, a preliminary live cell imaging studies showed uptake of NIRmbc94 in CB_2-expressing DBT cells. Overall, NIRmbc94 has been shown to be a potent CB_2 receptor targeted imaging agent and mbc94 seems to be a promising conjugable CB_2 receptor ligand.

6.5 Acknowledgement

6.6 References

(1)   Gouldson, P.; Calandra, B.; Legoux, P.; Kerneis, A.; Rinaldi-Carmona, M. et al. Mutational analysis and molecular modelling of the antagonist SR 144528 binding site on the human cannabinoid CB2 receptor. *European Journal of Pharmacology* **2000**, *401*, 17-25.

(2)   Andersson, H.; D'Antona, A. M.; Kendall, D. A.; Von Heijne, G.; Chin, C. N. Membrane assembly of the cannabinoid receptor 1: Impact of a long N-terminal tail. *Molecular Pharmacology* **2003**, *64*, 570-577.

(3)   Matsuda, L. A.; Lolait, S. J.; Brownstein, M. J.; Young, A. C.; Bonner, T. I. Structure of a Cannabinoid Receptor and Functional Expression of the Cloned Cdna. *Nature* **1990**, *346*, 561-564.

(4)   Munro, S.; Thomas, K. L.; Abushaar, M. Molecular Characterization of a Peripheral Receptor for Cannabinoids. *Nature* **1993**, *365*, 61-65.

(5)   Pertwee, R. G. Pharmacology of cannabinoid CB1 and CB2 receptors. *Pharmacology & Therapeutics* **1997**, *74*, 129-180.

(6)   Galiegue, S.; Mary, S.; Marchand, J.; Dussossoy, D.; Carriere, D. et al. Expression of Central and Peripheral Cannabinoid Receptors in Human Immune Tissues and Leukocyte Subpopulations. *European Journal of Biochemistry* **1995**, *232*, 54-61.

(7)   Xie, X. Q.; Chen, J. Z.; Billings, E. M. 3D structural model of the G-protein-coupled cannabinoid CB2 receptor. *Proteins-Structure Function and Genetics* **2003**, *53*, 307-319.

(8)   Derocq, J. M.; Segui, M.; Marchand, J.; Lefur, G.; Casellas, P. Cannabinoids Enhance Human B-Cell Growth at Low Nanomolar Concentrations. *Febs Letters* **1995**, *369*, 177-182.

(9)   Kaminski, N. E. Immune regulation by cannabinoid compounds through the inhibition of the cyclic AMP signaling cascade and altered gene expression. *Biochemical Pharmacology* **1996**, *52*, 1133-1140.

(10)   Sanchez, C.; Velasco, G.; Guzman, M. Metabolic stimulation of mouse spleen lymphocytes by low doses of delta(9)-tetrahydrocannabinol. *Life Sciences* **1997**, *60*, 1709-1717.

(11)   Malan, T. P.; Ibrahim, M. M.; Lai, J.; Vanderah, T. W.; Makriyannis, A. et al. CB2 cannabinoid receptor agonists: pain relief without psychoactive effects? *Current Opinion in Pharmacology* **2003**, *3*, 62-67.

(12) Malan, T. P.; Ibrahim, M. M.; Deng, H. F.; Liu, Q.; Mata, H. P. et al. CB2 cannabinoid receptor-mediated peripheral antinociception. *Pain* **2001**, *93*, 239-245.

(13) Iwamura, H.; Suzuki, H.; Ueda, Y.; Kaya, T.; Inaba, T. In vitro and in vivo pharmacological characterization of JTE907, a novel selective ligand for cannabinoid CB2 receptor. *Journal of Pharmacology and Experimental Therapeutics* **2001**, *296*, 420-425.

(14) Karsak, M.; Ofek, O.; Fogel, M.; Wright, K.; Tam, J. et al. The cannabinoid CB2 receptor: A potential target for the diagnosis and treatment of osteoporosis. *Journal of Bone and Mineral Research* **2004**, *19*, S383-S383.

(15) Sanchez, C.; de Ceballos, M. L.; del Pulgar, T. G.; Rueda, D.; Corbacho, C. et al. Inhibition of glioma growth in vivo by selective activation of the CB2 cannabinoid receptor. *Cancer Research* **2001**, *61*, 5784-5789.

(16) McKallip, R. J.; Lombard, C.; Fisher, M.; Martin, B. R.; Ryu, S. H. et al. Targeting CB2 cannabinoid receptors as a novel therapy to treat malignant lymphoblastic disease. *Blood* **2002**, *100*, 627-634.

(17) Pertwee, R. G. Cannabinoids and multiple sclerosis. *Pharmacology & Therapeutics* **2002**, *95*, 165-174.

(18) Gaoni, Y.; Mechoulam, R. Isolation, Structure, and Partial Synthesis of an Active Constituent of Hashish. *Journal of the American Chemical Society* **1964**, *86*, 1646-1647.

(19) Devane, W. A.; Hanus, L.; Breuer, A.; Pertwee, R. G.; Stevenson, L. A. et al. Isolation and Structure of a Brain Constituent That Binds to the Cannabinoid Receptor. *Science* **1992**, *258*, 1946-1949.

(20) Mechoulam, R.; Fride, E.; Di Marzo, V. Endocannabinoids. *European Journal of Pharmacology* **1998**, *359*, 1-18.

(21) Oka, S.; Ikeda, S.; Kishimoto, S.; Gokoh, M.; Yanagimoto, S. et al. 2-Arachidonoylglycerol, an endogenous cannabinoid receptor ligand, induces the migration of EoL-1 human eosinophilic leukemia cells and human peripheral blood eosinophils. *Journal of Leukocyte Biology* **2004**, *76*, 1002-1009.

(22) Pertwee, R. G.; Ross, R. A. Cannabinoid receptors and their ligands. *Prostaglandins Leukotrienes and Essential Fatty Acids* **2002**, *66*, 101-121.

(23) Griffin, G.; Wray, E. J.; Tao, Q.; McAllister, S. D.; Rorrer, W. K. et al. Evaluation of the cannabinoid CB2 receptor-selective antagonist, SR144528: further evidence for cannabinoid CB2 receptor absence in the rat central nervous system. *European Journal of Pharmacology* **1999**, *377*, 117-125.

(24)   Bouaboula, M.; Dussossoy, D.; Casellas, P. Regulation of peripheral cannabinoid receptor CB2 phosphorylation by the inverse agonist SR 144528 - Implications for receptor biological responses. *Journal of Biological Chemistry* **1999**, *274*, 20397-20405.

(25)   Portier, M.; Rinaldi-Carmona, M.; Pecceu, F.; Combes, T.; Poinot-Chazel, C. et al. SR 144528, an antagonist for the peripheral cannabinoid receptor that behaves as an inverse agonist. *Journal of Pharmacology and Experimental Therapeutics* **1999**, *288*, 582-589.

(26)   Raitio, K. H.; Salo, O. M. H.; Nevalainen, T.; Poso, A.; Jarvinen, T. Targeting the cannabinoid CB2 receptor: Mutations, modeling and development of CB2 selective ligands. *Current Medicinal Chemistry* **2005**, *12*, 1217-1237.

(27)   Roy, A. K.; Batra, S. Facile Baylis-Hillman reaction of substituted 3-isoxazolecarbaldehydes: The impact of a proximal heteroatom within a heterocycle on the acceleration of the reaction. *Synthesis-Stuttgart* **2003**, 2325-2330.

(28)   Seltzman, H. H.; Foster, M. C.; Wyrick, C. D.; Burgess, J. P.; Carroll, F. I. Tritiation of the cannabinoid receptor antagonist SR144528 involving lithium aluminum tritide reduction; assessment of the kinetic isotope effect by H-3-NMR. *Journal of Labelled Compounds & Radiopharmaceuticals* **2005**, *48*, 589-596.

(29)   Suchocki, J. A.; May, E. L.; Martin, T. J.; George, C.; Martin, B. R. Synthesis of 2-Exo-Mecamylamine and 2-Endo-Mecamylamine Analogs - Structure-Activity-Relationships for Nicotinic Antagonism in the Central-Nervous-System. *Journal of Medicinal Chemistry* **1991**, *34*, 1003-1010.

(30)   Cheng, Y.; Prusoff, W. H. Relationship between Inhibition Constant (K1) and Concentration of Inhibitor Which Causes 50 Per Cent Inhibition (I50) of an Enzymatic-Reaction. *Biochemical Pharmacology* **1973**, *22*, 3099-3108.

(31)   Shah, K.; Weissleder, R. Molecular optical imaging: applications leading to the development of present day therapeutics. *The American Society for Experimental NeuroTherapeutics* **2005**, *2*, 215-225.

(32)   Rinaldi-Carmona, M.; Barth, F.; Millan, J.; Derocq, J. M.; Casellas, P. et al. SR 144528, the first potent and selective antagonist of the CB2 cannabinoid receptor. *Journal of Pharmacology and Experimental Therapeutics* **1998**, *284*, 644-650.